

1969

Pionic and muonic x-rays in liquid Helium-4

Robert John. Wetmore
College of William & Mary - Arts & Sciences

Follow this and additional works at: <https://scholarworks.wm.edu/etd>

Recommended Citation

Wetmore, Robert John., "Pionic and muonic x-rays in liquid Helium-4" (1969). *Dissertations, Theses, and Masters Projects*. Paper 1539623652.

<https://dx.doi.org/doi:10.21220/s2-19k8-zx04>

This Dissertation is brought to you for free and open access by the Theses, Dissertations, & Master Projects at W&M ScholarWorks. It has been accepted for inclusion in Dissertations, Theses, and Masters Projects by an authorized administrator of W&M ScholarWorks. For more information, please contact scholarworks@wm.edu.

70-5249

WETMORE, Robert John, 1939-
PIONIC AND MUONIC X-RAYS IN LIQUID
He⁴.

The College of William and Mary in Virginia,
Ph.D., 1969
Physics, nuclear

University Microfilms, Inc., Ann Arbor, Michigan

PIONIC AND MUONIC X-RAYS IN LIQUID He⁴

A Thesis
Presented to
The Faculty of the Department of Physics
The College of William and Mary in Virginia

In Partial Fulfillment
Of the Requirements for the Degree of
Doctor of Philosophy

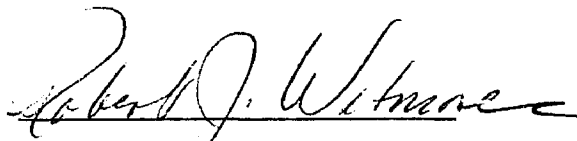
by

Robert John Wetmore


August 1969

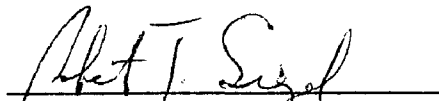
APPROVAL SHEET

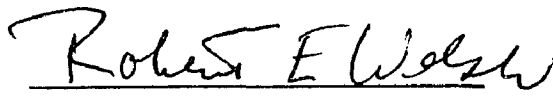
This thesis is submitted in partial fulfillment of
the requirements for the degree of
Doctor of Philosophy


Robert J. Wetmore

Approved, August 1969


John R. Kane


Robert T. Siegel


Robert E. Welsh


Carl M. Andersen


Richard L. Kiefer

PIONIC AND MUONIC X-RAYS IN LIQUID He⁴

TABLE OF CONTENTS

	page
I. ABSTRACT	1
II. INTRODUCTION	3
A. Energies	
B. Linewidths	
C. The Ericson Theory	
D. Effective Range Theory	
E. Yields	
III. LIQUID HELIUM SCINTILLATION COUNTER	25
A. Description	
B. Assembly and Operation	
C. Auxilliary Equipment	
IV. EXPERIMENTAL METHOD	33
A. Si(Li) Spectrometer	
B. Beam Characteristics, Experimental Arrangement, and Description of Counters	
C. Timing and Logic	
D. Stabilization	
E. Experimental Technique and Calibration	
V. DATA ANALYSIS: ENERGY	45
A. Analysis of Spectra	
B. Energy Determination	
C. Correction of Energies for the Effects of Compton Scattering	
D. Discussion of Errors	

	page
VI. DATA ANALYSIS: NATURAL LINEWIDTHS	59
A. Introduction	
B. Determination of Peak Shapes	
C. The Pionic 1s Level Width	
D. Negligible Sources of Error	
VII. DATA ANALYSIS: YIELDS	72
A. Experimental Arrangement	
B. Derivation of Yield Expression	
C. Detector Efficiency	
D. The Average Efficiency of the System	
E. The Numbers of X-Rays Observed	
F. The Number of Stopping Particles	
G. Negligible Sources of Error	
H. Tabulation of Yields	
VIII. DISCUSSION OF RESULTS	96
A. Energies	
B. Natural Linewidth	
C. Yields	
IX. TABLES	102
X. ACKNOWLEDGEMENTS	113
XI. APPENDICES	115
A. Mass Absorption Coefficients	
B. Intensities of Radiations from the Calibrated Co ⁵⁷ Source	
C. Anticoincidence Efficiency of Beam Telescope During Yield Runs	

	page
XII. LIST OF REFERENCES	121
XIII. FIGURES	125

I. ABSTRACT

Negative pions and muons were stopped in a liquid helium scintillation counter and resulted in the formation of pionic and muonic He^4 atoms. Pionic and muonic x-rays from these atoms were observed with a Si(Li) spectrometer. The energies and yields of the K series x-rays were measured. The natural linewidth of the pionic 1s level was also measured.

From the observed energy of the $\pi\text{-K}_\alpha$ transition of 10.70 ± 0.05 keV, the nuclear force shift ΔE_{nucl} of the 1s level was measured and found to be in agreement with its value as predicted by existing theories. The measured value is:

$$\Delta E_{\text{nucl}} = 80 \pm 50 \text{ eV.}$$

The measured value of the natural linewidth of the 1s level of the pionic He^4 atom is:

$$\Gamma_{\text{nat}} = 10 \begin{array}{c} + 60 \\ - 10 \end{array} \text{ eV.}$$

This value was found to be in disagreement with an Eckstein prediction of 400 ± 240 eV, but in satisfactory agreement with other theoretical predictions.

The measured values of the absolute x-ray yields are:

<u>Transition</u>	<u>Yield</u>	<u>Transition</u>	<u>Yield</u>
$\pi\text{-K}_\alpha$	0.0336 ± 0.0080	$\mu\text{-K}_\alpha$	0.596 ± 0.110
$\pi\text{-K}_\beta$	0.0518 ± 0.0110	$\mu\text{-K}_\beta$	0.268 ± 0.054
$\pi\text{-K}_\gamma$	0.00946 ± 0.00320	$\mu\text{-K}_\gamma$	0.059 ± 0.023
Total $\pi\text{-K}$	0.0949 ± 0.0140	Total $\mu\text{-K}$	0.923 ± 0.130

The measured values of the relative yields are:

$$Y_{\pi\text{-K}_\alpha} / Y_{\text{all K}} = 0.354 \pm 0.060$$

$$Y_{\mu\text{-K}_\alpha} / Y_{\text{all K}} = 0.647 \pm 0.052$$

$$Y_{\pi\text{-K}_\alpha} / Y_{\pi\text{-K}_\beta} = 0.649 \pm 0.180$$

$$Y_{\mu\text{-K}_\alpha} / Y_{\mu\text{-K}_\beta} = 2.23 \pm 0.53$$

II. INTRODUCTION

A mesonic (muonic) atom is formed when a negative meson (muon) becomes bound in the Coulomb field of a nucleus. In 1947, Conversi, Pancini and Piccioni¹ stopped negative cosmic muons in graphite and detected muonic decay electrons. Fermi and Teller² noted that relativistic muons slowing down in condensed matter would reach an energy of 2000 eV in $\sim 10^{-10}$ seconds. Treating the atomic electrons of the stopping material as a degenerate electron gas, they calculated that the time required for the muon to go from 2000 eV of energy to capture in the K shell of the atom was less than 10^{-13} seconds. Since muons were known to have lifetimes of $\approx 2 \mu\text{s}$, it was clear that the muons were decaying from the K shells of carbon atoms. The experiment and its interpretation dispelled the then current belief that the muon was the Yukawa meson. If it was, nuclear capture of the muon from the K shell would have occurred in $\sim 10^{-19}$ seconds. Wheeler³ then showed that for a muon in the K shell of an atom, one would expect a Z^4 dependence in the nuclear capture rate. Ticho⁴ verified Wheeler's prediction by stopping muons in a number of low Z target materials. As a result of the efforts of these workers, the existence of muonic atoms was demonstrated. The formation of pionic atoms was demonstrated by Camac et al.⁵ who stopped a beam of 40 MeV negative pions in targets of graphite, water and beryllium and observed the $\pi\text{-K}_\alpha$ x-rays with a NaI(Tl) crystal.

Since the time of the experiment of Camac et al., mesic and muonic x-rays have been observed in a great variety of materials, and their energies, widths and yields measured with ever-increasing precision.

Theories have also been developed which describe the meson-nucleus interaction and predict the results of mesic x-ray measurements. Mesic and muonic x-rays in He^4 had not been observed prior to this experiment, probably because of the difficulty of preparing a liquid helium target. Such a target was developed at William and Mary and accordingly, a program was undertaken to observe the x-rays.

The purpose of the present experiment is threefold:

1. To demonstrate the existence of the pionic and muonic x-rays in liquid He^4 .
2. To measure the energies and widths of the x-rays for a comparison with existing theories.
3. To experimentally determine the x-ray yields.

The basic properties of pionic (muonic) atoms can be demonstrated by using the Bohr theory. A pion (muon) in a Bohr orbit about a nucleus of charge Z has an energy

$$E_n = -\bar{\mu}c^2 \frac{(Z\alpha)^2}{2n^2}, \quad (1)$$

where: $\bar{\mu} = \mu(1 + \mu/A)^{-1}$ is the reduced pion (muon) mass
 μ is the pion (muon) mass.

The orbit radius is

$$r_n = \frac{\hbar^2}{\bar{\mu}e^2} \frac{n^2}{Z}, \quad (2)$$

and the pion (muon) has a velocity

$$v_n = \alpha c \frac{Z}{n}. \quad (3)$$

Since the pion (muon) is 273 (206) times as heavy as the electron, it follows from Eq. (2) that Bohr orbit radii are considerably smaller than electronic radii in an atom. In fact, a pion (muon) in a state of principal quantum number $n = 17$ ($n = 14$) and a K electron of a particular atom have approximately the same Bohr radius. Hence a pion (muon) in a level of $n < 17$ ($n < 14$) is located within the electron cloud of an atom and the pion-nucleus (muon-nucleus) system can be viewed as a hydrogenic atom with the electron being replaced by a pion (muon).

Eq. (1) shows that the characteristic energies of pionic and muonic atoms are in magnitude larger than the energies of electronic atoms by the pion and muon to electron mass ratio respectively. Eq. (3) shows that relativistic effects are only as important for pionic or muonic atoms as they are for electronic atoms since v_n is independent of the particle's mass.

A. Energies

1) Calculation of Muonic X-Ray Energies in He^4

The energy levels of a muonic atom can be calculated with high accuracy by using the Dirac equation for a point nucleus and then correcting the results for the effects of the finite nuclear size and for vacuum polarization.⁶ For a point nucleus the energies are given by

$$E_{n,j} = - \frac{\bar{\mu}c^2}{2n^2} (Z\alpha)^2 \left[1 + \frac{(Z\alpha)^2}{n^2} \left[\frac{n}{j + \frac{1}{2}} - \frac{3}{4} \right] - \dots \right], \quad (4)$$

where terms of order $(Z\alpha)^6$ have been neglected. The Dirac energies for

the He⁴ x-rays are given in Table I(a). The spin-orbit splitting is ≤ 0.2 eV and has been neglected.

Since the helium nucleus is of finite extent, the field in its interior is not Coulombic and causes muons to be less bound than they would be for a point nucleus. The resultant shift in energies can be calculated from perturbation theory using*

$$\Delta E_{\text{fns}} = \int |\psi|^2 (V - V_p) d\tau, \quad (5)$$

where $V - V_p$ is the difference between the actual potential and the Coulomb potential. The effect is greatest for s states and the level shift for the 1s state has been calculated by Cooper and Henley⁷ who obtain

$$\Delta E_{\text{fns}} = \frac{1}{\pi} \left(\frac{Z}{a_0} \right)^3 \int (V - V_p) d\tau, \quad (6)$$

where $a_0 = \hbar^2 / \mu e^2$ is the muonic Bohr radius. They show further that if

$$\lim_{r \rightarrow \infty} r^3 (V - V_p) = 0,$$

Eq. (6) can be rewritten:

$$\Delta E_{\text{fns}} = \frac{2}{3} \left(\frac{Z}{a_0} \right)^3 e \int r^2 \rho d\tau, \quad (7)$$

where ρ is the nuclear charge density normalized such that $\int \rho d\tau = Ze$.

* The convention used is that $\Delta E < 0$ corresponds to an increased binding of the 1s level and therefore to an increased transition energy.

The shift of the 1s level in He^4 due to the finite nuclear size can be calculated from Eq. (7) using the results of the electron scattering experiments by Hofstadter⁸ who finds the He^4 nuclear charge distribution to be best fit with the Gaussian

$$\rho(r) = \left(\frac{3}{2\pi}\right)^{3/2} \frac{Ze}{R^3} \exp\left(-\frac{3}{2} \frac{r^2}{R^2}\right) \quad (9)$$

with an RMS radius of $R = 1.61F$. Substitution of Eq. (9) into Eq. (7) gives for the shift of the 1s energy level in He^4

$$\Delta E_{\text{fns}} = \frac{2}{3} \frac{Z^4 e^2 R^2}{a_0^3} \quad (10)$$

The energy shifts due to finite nuclear size for levels with higher angular momentum quantum numbers are less than the 1s level shift because of the decreased muon-nucleus wave function overlap. West⁶ for example, gives an unpublished expression by Flügge wherein the fractional shift of the 2p level $\Delta E/E_{2p}$ is estimated to be

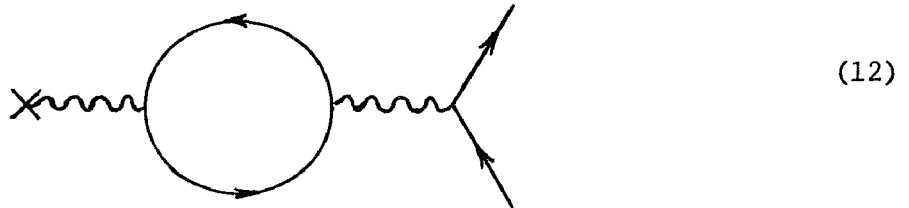
$$\frac{\Delta E}{E_{2p}} = \left[0.0018 \left(\frac{ZR}{a_0}\right)^4 - 0.001 \left(\frac{ZR}{a_0}\right)^5 + \dots \right] \quad (11)$$

The shift is $\sim 10^{-6}$ eV for He^4 and is negligible by comparison to the 1s level shift. The correction for the transition energy is therefore given by the negative of the 1s level shift and its value (-2 eV) is given in the second column of Table I(a).

Because the muon (pion) and nucleus polarize the vacuum in their vicinity, they experience more of their "bare" charges when they are

located close to each other. Thus vacuum polarization causes a lowering of the energy levels of the muonic (pionic) atom and since s states are the most affected, K series transition energies are increased by the effect.

Mickelwait and Corben⁹ have calculated this shift in the energy levels of pionic and muonic atoms. They note that the vacuum polarization is the major quantum electrodynamical effect shifting the levels (excluding the finite nuclear size effect), the shifts due to the muon (pion) self energy being $\sim 10^{-3}$ of the vacuum polarization shifts. The calculation was performed using first order perturbation theory and assuming the nucleus to be a point charge. The approximation used was inclusive of the second order term of an expansion of the S-matrix for an external Maxwell field interacting with a charged particle, corresponding to the Feynman diagram:



They obtain for the increase of the binding energy of the 1s level

$$\Delta E_{vp} = \frac{\alpha^3}{3\pi} \mu Z^2 \left[-\frac{11}{3} + \frac{3\pi\epsilon}{2} - 4\epsilon^2 + 2\pi\epsilon^3 + (2-\epsilon^2-4\epsilon^4) (1-\epsilon^2)^{-1/2} \ln \left[\epsilon^{-1} \left[1 + (1-\epsilon^2)^{1/2} \right] \right] \right], \quad (13)$$

where μ is the muon (pion) mass, M_e the electron mass and $\epsilon \equiv M_e/Z\mu\alpha$.

The next largest shifts are experienced by the 2p states which the authors calculated to be $\sim 1\%$ of the 1s level shift and therefore are negligible as far as their effect on the K series transition energies. They also estimate that the finite size of the nucleus affects their results to less than 8%. The correction to the muonic K series energies ($-\Delta E_{vp} = 20$ eV) is listed in Table I(a).

2) Calculation of Pionic X-Ray Energies in He^4 (Electromagnetic Effects Only)

The energy levels of a pionic atom can be calculated by using the Klein-Gordon equation and applying corrections for the effects of: (1) finite nuclear size, (2) vacuum polarization, and (3) the strong pion-nucleus interaction. Since the electromagnetic contributions to the x-ray energies are well known, a measurement of pionic x-ray energies is interpreted on the basis of the difference between the transition energy obtained from calculation which includes only electromagnetic effects ($\equiv E_{\text{calc}}$) and the measured value. This difference ΔE_{nucl} is the shift of the 1s level due to the strong pion-nucleus interaction and is called the "nuclear force shift."^{*} The resultant "experimental" value for the nuclear force shift is then compared with values from existing theories.

The main contribution to the energy levels of a pionic atom is given by the Klein-Gordon equation:⁶

* The nuclear force shift of the 2p state in a given atom is negligible in comparison to the 1s level shift. For example, Krell and Ericson (reference 10) have calculated it to be less than 0.1% of the 1s level shift in nitrogen.

$$E_{n,\ell} = -\frac{\mu c^2}{2n^2} (Z\alpha)^2 \left[1 + \frac{(Z\alpha)^2}{n^2} \left(\frac{n}{\ell + \frac{1}{2}} - \frac{3}{4} \right) \right], \quad (14)$$

where $Z < 137/2$ and terms $\sim (Z\alpha)^6$ have been neglected. The corrections to the Klein-Gordon energies due to the finite nuclear size and vacuum polarization are calculated in the same manner as for muonic atoms with the pion mass replacing the muon mass in Eqs. (10) and (13).^{*} The Klein-Gordon energies, corrections and the resultant E_{calc} are listed in Table I(b).

3) Calculations of the Nuclear Force Shift in Pionic He⁴

Deser et al.¹¹ were first to discuss 1s level shifts in pionic atoms. They considered the π^- -p system, assumed that the strong interaction was short ranged and used perturbation theory to write the energy shift matrix element. They then compared the energy shift matrix element to the matrix element of elastic scattering of positive-energy pions and wrote the energy shift for hydrogen in terms of the π^- -p scattering length $a(\pi^-)$:

$$\Delta E_{\text{nucl}} = -\frac{2\pi}{\mu} \left| \Psi_0(0) \right|^2 a(\pi^-), \quad (14)$$

where $\Psi_0(0)$ is the ground state wave function of the pion evaluated at the origin; $a(\pi^-) = \frac{1}{3} (2a_1 + a_3)$ where a_1 and a_3 are the scattering lengths for isotopic spin $\frac{1}{2}$ and $3/2$ respectively.

They then assumed for a complex nucleus having Z protons and n neutrons, that the effects of the nucleons were additive and obtained:

* Krell and Ericson¹⁰ have shown that contributions to the vacuum polarization correction due to the strong interaction are negligible for low Z atoms being ~ 1 -2%.

$$\frac{\Delta E_{\text{nuc1}}}{E_{K\alpha}} = -\frac{4}{3} \frac{\mu}{m} \frac{4Z}{a_0(\infty)} \left[\frac{2}{3} Z a_1 + \frac{3n+Z}{3} a_3 \right], \quad (15)$$

where $a_0(\infty)$ is the pionic Bohr radius for a nucleus of infinite mass and $E_{K\alpha}$ is the $2p - 1s$ transition energy. A recent determination of $a_1 + 2a_3 = -0.035 \pm 0.012$ (in units of $\mu = \hbar = c = 1$) by Samaranayake and Woolcock¹² is used in Eq. (15) in order to determine the prediction of Deser et al. for the nuclear force shift in He^4 . The result is:

$$\Delta E_{\text{nuc1}} (\text{Deser}) = 41 \pm 14 \text{ eV}. \quad (16)$$

Brueckner¹³ deduced that there would be an energy shift due to the inelastic process $\pi^- + \text{nucleus} \rightarrow \text{star}$ in addition to the elastic shift of Deser et al. He noted that the interaction $\pi^- + N \rightarrow N$ was in violation of momentum conservation and that experimentally, charge exchange scattering was absent in light nuclei. He assumed therefore, that the basic capture process involved the cooperation of two nucleons. He then derived an energy shift and a broadening of the $1s$ level by making use of the cross section $\sigma[\pi^- + A \rightarrow \text{star}]$ obtained from the results of Brueckner, Serber and Watson¹⁴ who derived it from the cross section $\sigma[p + p \rightarrow \pi^+ + D]$. The result Brueckner obtained was (for $n = 2$):

$$\Delta E_{\text{nuc1}} (\text{Brueckner}) = \Delta E_{\text{nuc1}} (\text{Deser}) + \frac{4}{3} \left(\frac{Z^2}{985} \right) E_{\pi-K\alpha}, \quad (17)$$

which evaluated for He^4 becomes

$$\Delta E_{\text{nuc1}} (\text{Brueckner}) = 99 \pm 14 \text{ eV}. \quad (18)$$

An extension of Brueckner's theory by Karplus and Halpern¹⁵ results in a shift 25% larger than the shift of Deser et al. Thus:

$$\Delta E_{\text{nucl}} \text{ (Karplus)} = 51 \pm 14 \text{ eV.} \quad (19)$$

Finally, Wolfenstein¹⁶, by including the elastic p wave interaction, which can contribute to 1s state scattering due to the motion of the nucleons in the nucleus, finds a shift equal to that of Karplus' and Halpern's but of the opposite sign, and thus concludes that the proper result should be somewhere in between the two. Therefore

$$\Delta E_{\text{nucl}} \text{ (Wolfenstein)} = 41 \pm 10 \text{ eV.} \quad (20)$$

More recently, Ericson and Ericson¹⁷ have developed an extensive theory of pion scattering in nuclei. Its discussion will be deferred until Sec. C where their predictions for the level shifts and widths of the pionic He⁴ atom will be presented. In Sec. D predictions of the shifts and widths on the basis of effective range theory will be discussed.

B. Linewidths

The time dependent part of the wave function of a quantum state of energy E_j , with mean life τ_j , is proportional to

$$\exp \left(- \frac{iE_j t}{\hbar} \right) \exp \left(- \frac{t}{2\tau_j} \right) . \quad (21)$$

The probability therefore that the state is occupied after a time t is

$$\exp\left(\frac{-t}{\tau_j}\right), \quad (22)$$

and the width Γ_j of the state is given by

$$\Gamma_j = \frac{\hbar}{\tau_j}. \quad (23)$$

Because of the strong pion-nucleus interaction, pions undergo rapid capture from s states of the lightest nuclei and a broadening of the pionic K series x-rays is expected. Broadening of muonic x-rays in low Z materials is negligible since the capture process is competitive with free decay.¹ The radiative transition rates for pions and muons in p states are $\sim 10^{13}$ /sec and contribute negligibly to broadening.

As was mentioned in Sec. A, values of the natural linewidths of $1s$ states in pionic atoms were first predicted by Brueckner.¹³ On the basis of a two-nucleon capture model, in which the final state was assumed to consist of two fast nucleons, he derived the following expression for the $1s$ level width Γ_{nat} :

$$\Gamma_{\text{nat}} \text{ (Brueckner)} = \frac{8}{3} \frac{Z^2}{2150} E_{\pi-K_\alpha} \quad (24)$$

which, evaluated for He^4 , becomes

$$\Gamma_{\text{nat}} \text{ (Brueckner)} = 53 \text{ eV}. \quad (25)$$

More recently, Eckstein,¹⁸ using the two-nucleon capture model of Brueckner as a basis, calculated the capture rates of negative pions from s states of He⁴ for each of the possible final states — t + n, D + 2n, p + 3n. Eckstein's calculation which uses the most general phenomenological Hamiltonian consistent with zero-range absorption contains two coupling constants. These coupling constants, which are obtained from pion production cross section data, contain all of the complications arising from short-range nuclear correlations.

We present here, Eckstein's results calculated with more recent values of the coupling constants.¹⁹ Although the coupling constants are known to be relatively real, their signs have not been uniquely determined. If they are assumed to have the same sign, Eckstein's prediction for the ratio of triton final state captures to total capture is 0.23. If the coupling constants are assumed to have the opposite signs, this ratio becomes 0.07. On the basis of a measurement by Schiff et. al.²⁰ who find the ratio to be 0.33, Eckstein favors the same sign for the constants.

With the same sign for the coupling constants, then, Eckstein's prediction for the natural linewidth of the 1s level in He⁴ is:

$$\Gamma_{\text{nat}}^{+} \text{ (Eckstein)} = 400 \pm 240 \text{ eV.} \quad (26)$$

If the coupling constants are assumed to have different signs, then:

$$\Gamma_{\text{nat}}^{-} \text{ (Eckstein)} = 141 \pm 85 \text{ eV.} \quad (27)$$

C. The Ericson Theory

1) Description

A theory of the behavior of low-energy pions in finite nuclei has been developed by M. Ericson and T.E.O. Ericson¹⁷ which, together with the computational techniques of M. Krell and T.E.O. Ericson¹⁰, can be used to predict energies and widths of pionic x-rays. Central to the theory is an optical potential having parameters which can be related to $\pi - N$ scattering results and to pion production cross sections.

In the Ericson theory, the nucleons bound in a nucleus are assumed to scatter low energy pions in the same way as do free nucleons except for trivial kinematical effects. In their paper, the Ericsons do a simplified multiple scattering problem in the impulse approximation with the p-wave component of the $\pi - N$ interaction included as well as short-range nucleon pair correlations. They derive thereby the following phenomenological potential:

$$V(\vec{r}) = - \frac{4\pi}{2\mu} \left[b_0 \rho(\vec{r}) - \nabla \cdot \frac{c_0 \rho(\vec{r})}{1 + \frac{4}{3} \pi c_0 \rho(\vec{r})} \nabla \right], \quad (29)$$

where b_0 and c_0 are constants. The potential is seen to have explicit nonlocality and a nonlinear dependence on the nucleon density. It is pointed out by the Ericsons that by setting $b_0 = 0$, Eq. (29) describes the dipole scattering of electromagnetic waves in a dense polarizable

medium in which the medium is seen to display a refractive index dependent on its density (Lorentz-Lorenz effect).

The Ericsons then generalize the simplified potential in order to include (1) different kinds of scatterers, (2) spin and isospin effects and (3) kinematical factors. The potential is further generalized to include absorption based on Brueckner's two-nucleon theory by doing the multiple scattering problem using a two-nucleon scattering amplitude.

Krell and Ericson¹⁰ write the complete phenomenological potential in the following form:

$$2\bar{\mu} V(\vec{r}) = q(\vec{r}) + \nabla \cdot \alpha(\vec{r}) \nabla, \quad (30a)$$

with

$$q(\vec{r}) = -4\pi \left[p_1 b_0 \rho(\vec{r}) + p_1 b_1 \left(\rho_n(\vec{r}) - \rho_p(\vec{r}) \right) + ip_2 \text{Im} B_0 \rho^2(\vec{r}) \right] \quad (30b)$$

$$\alpha(\vec{r}) = \alpha_0(\vec{r}) \left[1 + \xi \frac{\alpha_0(\vec{r})}{3} \right]^{-1} \quad (30c)$$

$$\alpha_0(\vec{r}) = 4\pi \left[p_1^{-1} c_0 \rho(\vec{r}) + ip_2 \text{Im} C_0 \rho^2(\vec{r}) \right]; \quad (30d)$$

where b_0 , b_1 , $\text{Im}B_0$, c_0 and $\text{Im}C_0$ are real constants associated with the elementary interactions; $p_1 = (1 + \mu/M)$ and $p_2 = (1 + \mu/2M)$ are kinematical constants with M the nucleon mass; $\rho(\vec{r}) = \rho_n(\vec{r}) + \rho_p(\vec{r})$, where ρ_n and ρ_p are average neutron and proton mass densities respectively. Nuclear correlations are included in the parameter ξ where:

$\xi = 0$ for a smooth neutron and proton distribution

$\xi \neq 0$ for a nucleus having a granular structure

$\xi = 1$ for short range anti-correlations between nucleons.

Certain effects are included in the parameters of the potential (Eq. (30)) and certain approximations are made in deriving it:

1. Nuclear correlation effects dominate the local part of the potential although they are not made explicit.
2. All explicit dependence on neutron and proton density is concentrated in the b_1 term.
3. The dispersive effects produced by absorptive processes are not explicit.
4. Strong-interaction hyperfine effects are neglected.
5. The two-nucleon density in absorptive terms is approximated by the square of the single nucleon density.

Thus the parameters of the potential are considered to be effective parameters (and are called such). They must be corrected in order that they may be related to the parameters of the elementary processes (termed basic parameters here).

In principle, one should be able to derive the effective parameters from the basic parameters and then use the Ericson theory to predict the outcome of measurements of the energies and widths of pionic x-rays. However, since corrections to some of the effective parameters (particularly b_0) are not well known, and since some disagreement exists as to the basic parameter values, an alternative approach is used to test the theory. The attempt is made to describe the existing body of mesonic x-ray data with a unique set of effective parameters. Comparison is then made with the basic parameter values of the parameters where possible.

2) Determination of Effective Parameters

The energy eigenvalues of the pionic atom levels are obtained by Krell and Ericson to a precision of 1 part in 10^6 by numerically solving the Klein-Gordon equation²¹:

$$\left[\nabla^2 + \left[(E - V_c)^2 - \bar{\mu}^2 \right] \right] \Psi = 2\bar{\mu} V \Psi, \quad (31)$$

where V_c is the potential for an extended nuclear charge, E is the pion binding energy including the rest mass, and $\hbar = c = 1$. Nuclei are assumed to be spherical. The mass densities are represented by two-parameter Fermi distributions:

$$\rho^F(r) = N \left[1 - \exp \left[4 \ln \frac{3(r - c)}{t} \right] \right]^{-1}, \quad (32)$$

where the normalization N is chosen such that the integral of $\rho^F(r)$ is the total number of particles, and c and t are the radial and surface thickness parameters respectively. The proton distribution is related to the nuclear charge distribution by the conventional correction for the proton size:

$$\langle r^2 \rangle_{p\text{-dist}} = \langle r^2 \rangle_{\text{chg}} - \langle r^2 \rangle_p. \quad (33)$$

The shape of the neutron and proton distributions is kept the same. Corrections to the energy levels for vacuum polarization are made with perturbation theory. The strong interaction is calculated to affect the corrections to a negligible 1-2%.

The effective parameter values are varied in the potential V and the following choices are determined to fit well the existing experimental data on pionic atoms.

$$\begin{aligned} b_0 &= -0.030 \mu^{-1}; & b_1 &= -0.080 \mu^{-1}; & \text{Im}B_0 &= 0.040 \mu^{-4} \\ c_0 &= 0.24 \mu^{-3}; & \text{Im}C_0 &= 0.14 \mu^{-6} \end{aligned} \quad (34)$$

In evaluating the uniqueness of the set of parameters with respect to the $1s$ level shifts, they find that in switching off the gradient interaction as well as the absorption ($\text{Im}B_0 = c_0 = \text{Im}C_0 = 0$), b_0 and b_1 remain nearly the same. They conclude therefore that the $1s$ level shifts are dominated by the real part of the local interaction. On the other hand, they find that the $1s$ level widths are changed by setting $b_0 = b_1 = 0$ but argue that it physically is unreasonable to

turn off the real interaction since doing so would increase the amount of wave function overlap with the nucleus, thereby increasing the absorption.

3) Ericson Theory Prediction of Shift and Width of the 1s Level of Pionic He⁴

Using the effective parameters given in Eqs. (34), Krell²² has calculated the nuclear force shift and 1s level width of the pionic He⁴ atom. He used a Fermi distribution for the nucleus with a RMS charge radius of 1.63F and with $c = 1.48F$ and $t = 1.0F$. The predictions of the 1s level shifts and widths are (i.e. the values they must be in order to be consistent according to theory with the other pionic atom data):

$$\Delta E_{\text{nucl}} (\text{Ericson}) = 111 \text{ eV} \quad (35)$$

and

$$\Gamma_{\text{nat}} (\text{Ericson}) = 69 \text{ eV}. \quad (36)$$

Because of the values of the charge distribution parameters used, Krell states that the predicted width is an upper theoretical limit.

D. Effective Range Theory

Another approach to the problem of determining the level shifts and widths of pionic atoms results from the effective range theory. Trueman²³ has derived the relation between the s-wave strong interaction phase shift δ_0 and the s-wave pion-nucleus scattering length A_0 :

$$\frac{1}{a_0} \left[\frac{C_0^2(\eta) \cot \delta_0}{\eta} - 2g(\eta) \right] = -\frac{1}{A_0} + \frac{1}{2} r_0 k^2 + O(k^4) \quad , \quad (37)$$

where: a_0 is the pionic Bohr radius

r_0 is the effective range of the interaction

k is the wave number of the pion

$$\eta = (a_0 k)^{-1}.$$

The function $g(\eta)$ is given by

$$g(\eta) = \eta^2 \sum_{M=1}^{\infty} \frac{1}{M(m^2 + \eta^2)} - \ln(\eta) - 0.577, \quad (38)$$

and $C_0(\eta)$ is given by

$$C_0(\eta) = |\Gamma(1 + i\eta)| \exp\left(\frac{\pi\eta}{2}\right). \quad (39)$$

Trueman then derives the relationship between the (complex) $1s$ level shifts and the s -wave scattering length

$$\frac{\Delta E}{E_{K\alpha}} = \frac{4A_0}{a_0} \quad , \quad (40)$$

where terms $\sim (A_0/a_0)^2$ have been neglected and

$$\Delta E = \Delta E_{\text{nucl}} + i \frac{\Gamma_{\text{nat}}}{2} \quad (41)$$

Boyd and Veirs²⁴ have used the effective range theory as developed by Trueman and have determined thereby bounds for the nuclear force

shift and width of the 1s level of the pionic He^4 atom. The value for the scattering length used in Eq. (40) is chosen from the results of $\pi^\pm - \text{He}^4$ scattering data. They obtain a result for the nuclear force shift of

$$90 \text{ eV} \leq \Delta E_{\text{nuc1}} \text{ (Boyd)} \leq 160 \text{ eV} \quad , \quad (42)$$

and for the natural linewidth:

$$8 \text{ eV} \leq \Gamma_{\text{nat}} \text{ (Boyd)} \leq 116 \text{ eV}. \quad (43)$$

E. Yields

A negative pion (muon) stopping in liquid helium becomes bound to an atom after one of its electrons is ejected. The pionic (muonic) helium atom is assumed to be formed with the pion (muon) in a level of principal quantum number $n \approx 17$ ($n \approx 14$), since in this state the wave function best overlaps the electron which it replaces.²⁵ The pions (muons) are usually assumed to initially populate angular momentum states in proportion to the $2\ell + 1$ multiplicity of the states. Shortly after the formation of the pionic or muonic helium atom ($\sim 10^{-15}$ sec), an Auger effect transition takes place in which the remaining electron is ejected. The $(\pi - \text{He})^+$ or $(\mu - \text{He})^+$ ion which is formed is energetically unable to acquire another electron from the surrounding atoms.²⁵ Subsequent de-excitation of the pionic or muonic helium atom takes place through the following mechanisms:

1. Radiative transitions. The pion or muon is able to make radiative dipole transitions between the various quantum states. The transition probabilities, which are well known, are proportional to the square of the matrix element between the initial (n_i, ℓ_i) and final (n_f, ℓ_f) states and to the cube of the energy difference between them. Radiative transitions are the dominant de-excitation process in low lying levels ($n \lesssim 4$) and transitions with large $\Delta n = n_f - n_i$ are favored. The dipole selection rule is $\Delta \ell = \ell_f - \ell_i = \pm 1$ with $\Delta \ell = -1$ being more probable by two to three orders of magnitude than $\Delta \ell = +1$.

2. Auger transitions. When the pion or muon is in a level of $n > 4$, external Auger transitions dominate the cascade. The transition rates are not well known but Michael²⁶ has estimated them from the work of Leon and Bethe²⁷ who have calculated the rates for mesons bound in hydrogen. Auger transitions satisfy the same selection rules as radiative transitions but $\Delta \ell = 0$ is not strictly forbidden. The Auger rates depend only weakly on energy and $\Delta n = -1$, $\Delta \ell = -1$ transitions are favored. If an external Auger transition is energetically impossible in helium for $\Delta n = -1$, the transition is made with a larger Δn .

3. Stark mixing. The $(\pi - \text{He})^+$ or $(\mu - \text{He})^+$ ion in collisions with neighboring atoms is able to "feel" their Coulomb fields. A collisional Stark mixing of the ℓ states for a given principal quantum number can result. This mixing can affect the yields since it influences the population of the levels.

4. Nuclear capture (pions only). Because of the strong pion-nucleus interaction, pions reaching ns states will be captured by the nucleus, the capture rates ($\sim n^{-3} \times 10^{17}/\text{sec}$) being larger than either the radiative or Auger rates from these states. Nuclear capture from p states is also expected to compete with the Auger and radiative transitions from these states.²⁸

Competition among the above processes and the shape of the initial distribution determines the resultant x-ray yield.

The target was of steel construction, 1/2 inch in length by 1/2 inch in diameter. A Sulfrin Corporation target was used. A recessed flange was used so that an end plate could be used to stop charged particles traversing the definition of a stopping range with its axis horizontal. One end of the target was a 1/2 inch diameter sapphire window which could be viewed by photomicroscopy with a beryllium window which permitted the x-rays to pass into kovar rings, were then soft-soldered into a stainless steel o-ring was fashioned from the recess of the target flange ring, which was threaded into position. A vacuum seal was made between the retaining ring, thereby the flat surfaces of the end

4. Nuclear capture (pions only). Because of the strong pion-nucleus interaction, pions reaching ns states will be captured by the nucleus, the capture rates ($\sim n^{-3} \times 10^{17}/\text{sec}$) being larger than either the radiative or Auger rates from these states. Nuclear capture from p states is also expected to compete with the Auger and radiative transitions from these states.²⁸

Competition among the above processes and the shape of the initial distribution determines the resultant x-ray yield.

III. LIQUID HELIUM SCINTILLATION COUNTER

A. Description

The target (see Fig. 1) was a cylindrical vessel of stainless steel construction containing 3 liters of liquid helium. It was 6" in length by 6" in diameter with a 0.030" wall and was housed within a Sulfrian Corporation cryostat which had a 15 liter reservoir capacity. A recessed flange was welded at each end of the target into which an end plate could be sealed. The fast ($\tau_m < 7\text{ns}$) scintillations due to charged particles traversing the helium were used as an aid in the definition of a stopping particle.²⁹⁻³² The target was positioned with its axis horizontal, the beam entering through the cylinder wall. One end of the target was sealed by an end plate containing two 2" diameter sapphire windows through which the helium scintillations could be viewed by photomultipliers. The opposite end was sealed with a beryllium window which allowed the low energy (8-14 keV) x-rays to exit from the target. A series of similar high transmission windows permitted the x-rays to exit from the cryostat. Sapphire windows brazed into kovar rings, were purchased from Ceramaseal Corporation and were soft-soldered into a stainless steel end plate as shown in Fig. 1. An o-ring was fashioned from 0.092" diameter indium wire and placed in the recess of the target flange along with the end plate. A retaining ring, which was threaded onto the target flange, held the end plate in position. A vacuum seal was made by tightening the eight screws in the retaining ring, thereby causing the indium to be crushed between the flat surfaces of the end plate and the target flange.

The beryllium window, also shown in Fig. 1, was constructed by fitting a piece of 5" diameter by 0.050" thick beryllium into a stainless steel end plate having an aperture of 2½". An indium o-ring seal was made between the beryllium and its end plate and another between the end plate and the target. The tightening of the retaining ring screws caused both o-rings to be crushed simultaneously. Section B contains a more detailed discussion of the sealing procedure.

A liner (Fig. 2), 5½" in length with a diameter of 5-¾" and having a cylinder wall of 5 mil polished aluminum foil, was fitted into the target. The ends of the liner were 0.5 mil aluminized Mylar as was a partition in the vertical plane which divided the liner into two half cylinders. In each of the compartments thus formed, a 2" hole was cut at the end of the liner adjacent to the sapphire windows so that each compartment could be viewed independently by a photomultiplier tube. A diffuse reflecting surface was formed by spraying the interior of the liner with $\approx 8 \text{ mg/cm}^2$ of Tygon paint (SB-361 white). Over the paint, a coating of diphenylstilbene (DPS) was vacuum evaporated to a thickness of $100 \text{ }\mu\text{g/cm}^2$ in order to shift the wavelength of the primary helium scintillation light into the visible region where the quantum efficiency of the photocathodes is optimal.³³ The sapphire windows were coated with $50 \text{ }\mu\text{g/cm}^2$ of diphenylstilbene. At the beryllium window end of the liner, the paint and DPS were removed over a 3" diameter circle in order to permit maximum x-ray transmission. The liner thus constructed exhibited no cracking or peeling under repeated cycling to liquid helium temperature.

A 1/16" thick copper radiation shield (Fig. 3) surrounded the target. It was in thermal contact with liquid nitrogen and its walls were reduced in the beam direction over a 6" by 6" area by using 5 mil copper foil in place of the 1/16" plate. This decrease in thickness reduced both the scattering of the beam and the number of particles stopping in the shield. At the beryllium window end, a 2½" diameter opening was covered with 0.5 mil aluminized Mylar in order not to obstruct the transmission of x-rays while still shielding the target from thermal radiation. At the sapphire window side, the radiation shield was extended and designed to support the photomultiplier tubes. Fig. 3 depicts the radiation shield with its end pieces drawn back from their positions in order to reveal the structure of the phototube support and the interior of the shield.

Fig. 4 shows the entire counter assembled. The target was connected to the helium reservoir by means of an indium o-ring seal (neck seal). The thermal contact between the radiation shield and the liquid nitrogen jacket was made by fastening them together with 32 screws. A stainless steel vacuum jacket enclosed the elements of the counter and had a beryllium window 1½" in diameter by 0.010" thick to permit the transmission of x-rays. In the beam entrance and exit regions of the counter, the vacuum jacket was reduced in thickness to 0.020" over a 6" diameter circle. This was done in order to minimize scattering of the beam by the vacuum jacket and to decrease the number of particles stopping in its walls. At the end of the vacuum jacket near the photomultipliers, a 2" diameter vacuum line coupled the system to a portable pumping station. A valve arrangement allowed the target region to be

evacuated if desired. The seals on the vacuum jacket were of the conventional neoprene o-ring type. Fig. 4b is a horizontal sectioning of the counter which emphasizes the dual compartment nature of the target and also gives the material thickness in the beam direction.

In order to create surfaces of low emissivity which would decrease the loss rate of liquid helium, the greater portion of the inner cryostat was gold plated by the manufacturer. Those areas not plated were polished during counter assembly.

Amperex photomultiplier tubes were used to view the liquid helium scintillations. One of the tubes (PM-4) was a type 56TVP and the other (PM-5) a 56AVP. Lucite rings positioned the tubes $\approx \frac{1}{4}$ " from the sapphire windows. Five layers of 6 mil mumetal were wrapped around the tubes in order to insure reliable operation in the magnetic fringing field (≈ 10 gauss) of the cyclotron. There was a partition in the radiation shield between the two photomultipliers which, along with the split liner and dual sapphire windows optically isolated the compartments and their respective photomultipliers (See Fig. 4b). Light pulser tests confirmed that scintillations in compartment 4 could be seen only by PM-4 and scintillations in compartment 5 only by PM-5.

The photomultipliers were operated in a vacuum and were cooled to $\sim 200^\circ\text{K}$ because of their indirect contact to the radiation shield. The voltages were applied to the tube elements from an externally located voltage divider circuit. A 20 pin glass feed-through (Glasseal Corporation) was used to transmit the voltages through the vacuum jacket wall. The 56AVP (PM-5) gave $\approx 8\text{V}$ into 50Ω and the 56TVP (PM-4) gave $\approx 1\text{V}$ into 50Ω at a potential of 2.5 kV when a near minimum ionizing

pion-muon beam of momentum 200 MeV/c was allowed to traverse the target.

B. Assembly and Operation

The initial step in the assembly of the counter was the making of the indium o-ring seals. The sealing surfaces were cleansed of residual indium from previous seals, the end window units were attached to the target and the target connected to the helium reservoir. O-rings of 4" and 6" diameter were used at the neck and window seals respectively. After the initial tightening of the retaining ring screws, a period of ≈ 2 hours was allowed to elapse during which time the indium would flow under the applied pressures, thereby releasing the tension on the screws. They were then tightened a second time after which the indium flow ceased to be a problem. The 92 mil indium was crushed to 10 mils in the process and a seal was formed which was vacuum tight to liquid helium temperatures.

After a seal had been made for some time, the surfaces were generally bonded together. In order to facilitate removal of the windows from the target, there were holes in the retaining rings and 2 screws could be passed through them and fastened to the window unit. A nut on each of the screws was tightened against the retaining ring, thereby breaking the seal and withdrawing the unit from the recessed flange.

When the assembled system was found to be vacuum tight at room temperature, the liquid nitrogen jacket was filled. Liquid nitrogen was then introduced into the target region cooling it to $\approx 125^\circ\text{K}$. The target cooling was allowed to proceed slowly (2-3 hours) in order to

prevent vacuum leaks from developing due to non-uniform contraction of the window assemblies. When the target region attained a temperature of $\approx 125^{\circ}\text{K}$, the flow of nitrogen was halted, thereby preventing accumulation of liquid in the target. The cold nitrogen gas was withdrawn by evacuating the target region and then refilling it with cold helium gas from a 100 l helium storage dewar. The target region was evacuated and refilled with cold helium gas three times, in order to remove traces of nitrogen from the target. The remainder of the cooling process was completed with the liquid helium flowing at a slow rate from the storage dewar. Once the target region reached 4.2°K , it could be filled rapidly with liquid helium. The entire cooling process ($T = 300^{\circ}\text{K}$ to $T = 4.2^{\circ}\text{K}$) took 4-5 hours and consumed approximately 20 liters of liquid helium. The contents of the storage dewar were monitored by placing it on a Toledo balance. Operational characteristics of the counter are listed in Table II.

C. Auxilliary Equipment

Listed below are auxilliary items included in the scintillation counter, some of which were necessary to its operation while others were found to be useful:

1. A 4" oil diffusion pump (CVC type PMC 720-A) having a liquid nitrogen cooled baffle and backed by a 425 l/min Welch mechanical pump, was used in order to evacuate the scintillation counter.
2. A helium leak detector was coupled to the system to indicate vacuum leaks if they developed.

3. A small bulb (PEK 118), filled with $\frac{1}{2}$ atmosphere of hydrogen, was located within the vacuum jacket to the rear of the photomultipliers. A Huggins Laboratories high voltage supply (Model 961 D) ionized the gas at a 60 Hz rate. The "light pulser" was useful in monitoring the operation of the photomultipliers while the counter was cooling, and could also be used to observe the effects that the magnetic fringing field had on the operation of the photomultipliers.
4. A level indicator, which utilized a Wheatstone bridge circuit, was used in order to monitor the amount of liquid helium in the cryostat.³⁴ Two of the bridge resistors were fastened with a cryogenic epoxy (Helix Epoxy Products, type R313) into one end of a long stainless steel tube having a diameter of $\frac{1}{8}$ ". The resistors were positioned one above the other and were separated by $\frac{1}{4}$ ". The tube extended downward from the top of the cryostat and could be raised and lowered in order to follow the liquid level. When the lower resistor touched the liquid, the bridge was unbalanced and a sharp deflection of the galvanometer resulted. When both resistors were immersed, the bridge was balanced and the galvanometer current returned to zero. Using this type of indicator, the level of the liquid helium could be located unambiguously even when the cryostat was being filled.
5. A 0-1 atmosphere Wallace and Tiernan absolute pressure gauge (Model FA 160) was used in order to monitor the target vapor pressure during operation.

6. Also included were two copper-constantan thermocouples, one fastened to the target and the other to the nitrogen shield. The thermocouple leads were connected to a Wheelco chart recorder (Model 8012-2500) and the temperature constantly monitored.

IV. EXPERIMENTAL METHOD

The data for this experiment were obtained at the 600 MeV synchrocyclotron of the NASA Space Radiation Effects Laboratory (SREL) in Newport News, Virginia. In July 1967, an initial cyclotron run yielded data of few statistics and the results of that run have been previously reported.³⁵ During a second run of a week's duration in November 1967, the amount of experimental data was greatly increased and, in addition, data were obtained relating to the x-ray yields. The two runs differed only in minor details and apart from noting these differences where they occur, only the November run will be discussed here.

A. Si(Li) Spectrometer

The high resolution spectrometer used in this experiment was developed by other members of the Intermediate Energy Group at William and Mary, and is described in detail elsewhere.³⁶⁻³⁷ It consisted of a lithium drifted silicon detector which was cryogenically cooled, a FET (field effect transistor) preamplifier whose input stage was likewise cooled, a linear amplifier with pulse shaping, and a 1600 channel analyzer.

The Si(Li) detector was manufactured by Technical Measurements Corporation.* It was specified to be 80 mm² by 3 mm deep (Type W80-3AA) and was factory selected to have a leakage current of $\sim 10^{-11}$ A at 400 V. The input stage to a Tennelec TC130 preamplifier was modified and is shown in Fig. 5. All of the components of the input stage, as well as the detector, were housed within a "cold finger" type cryostat which

* These detectors were made by Kevex Corporation at the time of this writing.

had a 10 mil beryllium window in order to admit low energy x-rays. The detector was cooled by placing it in thermal contact with a 1" diameter by 3' long copper rod which was immersed in liquid nitrogen at its far end. Cooling lowered the noise at the input to the pre-amplifier, since the leakage current of the detector was reduced thereby. The detector was biased at 220 volts and since it was D.C. coupled to the preamplifier, it was insulated from the copper rod with ceramic spacers. The 2N3823 FET was cooled in a similar fashion but the ultimate temperature it reached could be adjusted by wrapping its case with varying thicknesses of teflon tape. This adjustment was used since the signal-to-noise ratio at the preamplifier input depended upon the temperature of the FET and was generally optimum at a temperature somewhat higher than 77°K.

A Tennelec TC200 amplifier was used in order to amplify and shape the detector pulses. It was operated in a singly-differentiated mode with differentiating and integrating time constants of 6.4 μ sec and 3.2 μ sec respectively. These settings were known to give the best energy resolution with the Si(Li) detector. Pole-zero cancellation was used in the main amplifier in order to reduce pulse pileup effects at high count rates.³⁸ The TC200 provided the input to a Victoreen (SCIPP) 1600 channel pulse height analyzer.

The response of the system was substantially linear but some non-linear effects were present which had to be taken into account in the data analysis. The system gain was set at 55.6 eV/channel (80.2 eV/channel was used during the July run). The spectrometer resolution under actual running conditions averaged 617 eV (FWHM) at 14.4 keV as measured with C_{57} .

B. Beam Characteristics, Experimental Arrangement, and Description of Counters

Pions were produced in the SREL synchrocyclotron when orbiting 600 MeV protons were incident on a vibrating beryllium target. Negative particles were bent out of the cyclotron by its magnetic field and entered a pair of 9" diameter quadrupole magnets which helped focus them into a beam. After the beam passed through the main shielding wall of the cyclotron, a bending magnet selected particles having a momentum of 200 MeV/c.

The experimental arrangement is shown in Fig. 6. A 6' thick concrete shielding wall was located between the bending magnet and the experimental apparatus. The wall contained an opening into which lead bricks were placed in such a manner that a "beam hole" 4½" wide by 6¼" high was formed. The momentum-selected beam had to pass through the hole before entering the experimental apparatus.

The average rate of particles through the beam hole was $\approx 5 \times 10^5$ /sec, with the beam containing pions, muons and electrons in the approximate proportions of 17:1:1. Stopping particles were selected on the basis of their range in matter by the use of polyethylene absorber (CH₂). The beam was "stretched" by the vibrating target such that it had a duty factor of ≈ 2.5 . There was also an "unstretched" component in the beam's time structure. Since the instantaneous "unstretched" beam rate was approximately the same as the instantaneous "stretched" rate, no beam gating was used.

The liquid helium scintillation counter was placed on two tables such that the target was positioned at beam height. The Si(Li) detector was located to one side of the beam path at a distance of 1.9" from the liquid helium (Fig. 6). A lead collimator with a 4" x 4" opening was placed adjacent to counter 3 of the beam telescope and provided part of the detector shielding. More important, however, the collimator was used with inserts of varying shapes and sizes in order that the stopping distribution and scattering of particles in the helium target could be studied. The results of these studies were subsequently used in the analysis for the x-ray yields.

Counters 1, 2, 3 and 6 were constructed in the William and Mary machine shop and consisted of commercial plastic scintillants (Pilot Chemical Co.) which were optically coupled to Amperex 56AVP photomultipliers by means of Lucite light pipes. Iron cylinders shielded the phototubes from the effects of the fringing magnetic fields of the cyclotron and the bending magnet. The sizes of the scintillants were:

Counter 1 -	8" x 8" x 1/4"
Counter 2 -	8" x 8" x 1/4"
Counter 3 -	4" x 4" x 1/8"
Counter 6 -	12" x 12" x 1/4"

Counters 1 and 2 were placed at either end of the beam hole and the 12 coincidence rate, in addition to being part of the particle stop

signature, was used in order to normalize other scaling rates for fluctuations in beam intensity. Counter 3 was placed against the beam entrance side of the vacuum jacket and controlled the entrance angle of the beam into the liquid helium target. Counter 6 was set against the beam exit side of the vacuum jacket and was operated in an anticoincidence mode. Counter C7 was a Čerenkov counter whose active region was 6" x 6" in area and 2" thick along the beam direction. It was filled with a fluorocarbon radiator (3M Co., Type FC75) which was viewed by a RCA 8575 photomultiplier. It was operated in an anticoincidence mode so as to discriminate against electrons in the beam.

Counters 4 and 5 were the compartment-photomultiplier combinations in the helium counter. The counters, when used as part of the logical requirement (i.e. in an "or" coincidence mode) for a particle stop signature, resulted in a peak to background ratio in the x-ray spectra which was a factor of two greater than the ratio in a spectrum where no logical requirements were made on the liquid helium scintillations. The counters were used in different logical configurations in the beam telescope depending on the type of run taking place. During "energy runs", in which the energies and linewidths of the x-rays were of primary interest, counters 4 and 5 were operated in an "or" coincidence mode. During "yield runs" from which the x-ray yields were to be determined, counter 5 was placed in anticoincidence in the beam telescope. Since compartments 4 and 5 were separated by only the thin Mylar partition, the making of compartment 5 into an anticoincidence counter improved the definition of a stopping particle over the "energy run" configuration.

The relative position of the detector and target was also dependent upon the type of run. During "energy runs" the detector was located along the cylinder axis of the target. During "yield runs" the detector was moved off the target axis by $\frac{1}{4}$ " in order that the liner partition would not interfere with the x-rays from compartment 4.

C. Timing and Logic

A block diagram of the logic which was used on "energy runs" is shown in Fig. 7. The fast (~ 10 nsec FWHM) outputs from the beam telescope counters were used as inputs to (Chronetics Model 101) discriminators (DISC 1-7). The outputs of the discriminators were applied to (Chronetics Model 102) coincidence units (COINC 1-4) with the result, which is evident from Fig. 7, that a particle stop signature (123, 4 or 5, $\overline{6} \overline{C7}$) generated an output from COINC 4. This output appeared ≈ 1.3 μ sec later at the "fast" input to COINC 5. During a "yield run", the particle stop signature was given by (1234 $\overline{56}$) and constituted the only difference between the "yield run" and "energy run" logic.*

An event occurring in the detector resulted in a pulse from the preamplifier which had a rise time of ≈ 100 nsec and a decay time of ≈ 50 μ sec. The pulse amplitude was doubled by the first stage of the linear amplifier, but its shape remained unchanged. The stage 1 output was used as an input to a Canberra Instruments 1410 amplifier

* The Čerenkov counter was inoperative at the time of the yield runs.

(DDLA), which was operated in a double delay line mode. A bipolar pulse was formed by the DDLA such that its zero-crossing time was independent of the pulse amplitude and therefore fixed in time relative to the detector event. The zero-crossover was sensed by an Ortec 420 single channel analyzer (SCA) which gave a timing pulse at the "slow" input to COINC 5 (hence the term "crossover timing"). Pulses were required (by the SCA discriminator) to have energies ≥ 4 keV in order to generate the "slow" input to COINC 5, since setting the requirement lower than 4 keV resulted in excessive triggering of the SCA by noise pulses which had been amplified by the DDLA. The upper limit to the energy of analyzable pulses was ≈ 80 keV due to the finite number of channels in the SCIPP. However, the efficiency of the detector for γ radiation begins to decrease for energies ≥ 20 keV attaining a value of ≈ 0.15 at 80 keV.

As has been mentioned in Sec. A, the detector pulse at the output of stage 3 of the TC200 was shaped for maximum energy resolution. This pulse was routed through the stabilizer (Fig. 7) and was digitized and stored in the memory of the analyzer if a gating pulse were present at the time of its arrival. A gating pulse was present at the analyzer only if a particle had stopped at the same time at which a detector event had occurred. For such cases, a "fast-slow" coincidence occurred at COINC 5, its output triggering a Canberra Instruments 1455 delay gate generator which in turn gave a 4 μ sec gate which was fed to the analyzer. The analyzer gate was delayed by the proper amount such that it would be in time to admit the energy pulse. If a detector event was unaccompanied by a stop signature, its energy information was not stored

in the analyzer. Conversely a stop signature alone was insufficient to gate the analyzer.

Included in the logic was a visual timing aid which performed the following functions:

1. It facilitated the adjustment of the amount of delay required in order to bring time correlated (i.e. "fast" and "slow") pulses into coincidence at COINC 5.
2. It enabled the resolving time of the "fast-slow" coincidence to be set.
3. It indicated if adjustments in timing were needed during the course of a run.

"Slow" pulses, some of the larger noise pulses from the DDLA, and uncorrelated detector events were used as "start" inputs for an EGG TH200A/N time to amplitude converter (TAC). Particle stop signatures, delayed by 2.4 μ sec were used as "stop" inputs to the TAC. The output pulse height from the TAC was proportional to the time difference between the arrival of a "start" and "stop" input. The amplitudes of the TAC output pulses corresponded to time differences between 0-1 μ sec and were supplied as input to a 400 channel analyzer (TMC 401) which was calibrated to have time interval of \approx 5 nsec/channel. The TMC timing analyzer could be operated in a "routing" mode; i.e., if a pulse were present at its "route" input, the input signal which would otherwise have been stored in channel N, would be stored in channel 200 + N. The spectrum which would result if there was no routing is shown in Fig. 8(a), where time correlated events appear in a "timing peak" which is superimposed upon a random background. The width of the timing peak

at its base was ≈ 200 nsec and was a measure of the resolution capability of the crossover timing technique. In actual operation, a routing pulse was applied to the analyzer whenever a coincidence was made at COINC 5. Thus with the amount of delay and the resolving time properly adjusted, the entire "timing peak" would appear in the upper 200 channels and a "trough" would remain in the lower 200 channels as shown in Fig. 8(b). The time interval routed was equal to the resolving time of COINC 5 and could be adjusted by varying the output widths of the DISC 9 and DISC 12 pulses. The resolving time used during the experiment was ≈ 250 nsec.

D. Stabilization

A Canberra Instruments 1495 digital spectrum stabilizer was used in order to reduce drifts of spectral peaks due to time variations of the spectrometer gain. A Fe^{55} source was accumulated during experimental runs and the stabilizer sensed drifts in the location of the source's 5.9 keV K_{α} x-ray peak. The stabilizer then adjusted the gain of the spectrometer in such a way as to oppose the sensed drift by incrementing a servopotentiometer.

The stabilizer was operated during the experiment as follows. It was predetermined that channel 222 would be the location for the center of the Fe^{55} K_{α} x-ray peak. An equal number of channels on the upper and lower sides of the peak were chosen as "windows" by means of selection switches on the stabilizer. The lower window covered the energy range from channels 216-220 and the upper window from channels 224-228. Peaks in the spectra were ≈ 11 channels FWHM. Two other parameters

of stabilizer operation were also set by means of selection switches:

1. The integral scaler, set at 32, which added counts in the lower and upper windows together, and
2. the differential scaler, set at 8, which constantly monitored the difference between the number of counts in the upper and lower windows.

Starting from a reset condition, if the difference in the number of counts between the upper and lower windows reached ± 8 before the integral scaler reached 32, this was interpreted as a drift of the stabilization peak and the system gain was changed slightly by the stabilizer. If on the other hand, the integral scaler reached 32 before the differential scaler reached ± 8 , the system gain was not changed by the stabilizer. In either case the scalers were reset and the scaling process was repeated. The scaler settings were chosen from elementary statistical considerations: 16 counts in each of the windows would allow a statistical difference of approximately 8 counts in the differential scaler if no drifts were present.

Fe^{55} was a convenient stabilization source. Its x-rays were lower in energy and were resolved from the lowest experimental peaks (see for example Fig. 10). In addition, the source had no radiations of higher energy which could contribute background in the energy region of interest. The intensity of the source was $\approx 50 \mu\text{Ci}$ but it was fastened to the detector housing in such a manner that only a portion of the x-rays could enter the beryllium window. Under these conditions, the x-rays were incident on the detector at ≈ 250 counts/min. During a run, only those x-rays from the source which were in random coincidence with stopping particles were stored in the analyzer.

E. Experimental Technique and Calibration

Runs were generally of three hours duration after which time enough data had been accumulated so that each run could be analyzed individually with a computer fit program. Runs were alternated between "pion runs" and "muon runs" during which pions and muons, respectively, were selected as stopping particles. Selection was made on the basis of a range curve which is shown in Fig. 9.

Typical pionic and muonic x-ray spectra are shown in Figs. 10 and 11, respectively. The pionic x-ray spectra were contaminated with muonic x-rays but not in such a way as to introduce complications into the analysis of the peaks. In fact, the $\mu\text{-K}_\alpha$ peak in a pionic spectrum was used as a measure of the instrumental width of the spectrometer in the analysis of the broadening of the $\pi\text{-K}_\alpha$ line. The muonic x-ray spectra contained no pionic x-ray lines and had an improved peak to background ratio over that of the pionic spectra.

The 6.40 keV x-rays and 14.389 keV γ -rays of Co^{57} were used to calibrate the spectrometer (See Fig. 12). Calibrations were made before and after each run in order that the system drifts could be taken into account in the data analysis. During calibration runs the beam remained on and the detector was located in the same position as it was during experimental runs. Thus the spectrometer was calibrated with the same rate of background radiation incident on the detector as during experimental runs. During calibration runs, the stopping particle requirement was removed from the "fast-slow" coincidence. Any incident radiation which satisfied the SCA requirements could

thereby be stored in the analyzer. Calibration runs were of 30 minutes duration with the 14.389 keV γ -rays incident at ≈ 550 counts/min. The detector was shielded from the Fe^{55} source and the spectrometer was placed in a nonstabilized mode since it was unable to fully resolve the Fe^{55} x-rays from those of Co^{57} .

V. DATA ANALYSIS:ENERGY

A. Analysis of Spectra

A least squares fitting procedure was used in order to determine the centers, widths and amplitudes of each of the peaks appearing in the experimental spectra. The analysis was performed on an IBM S/360 computer. The peaks were assumed to be Gaussian in shape and to be superimposed on a background which could be represented by a straight line of non-zero slope. For those cases in which a peak was entirely resolved from neighboring peaks; i.e., if there was a number of channels to either side of a peak which contained only background information, then the peak was fit to the following single Gaussian function:

$$f(x) = A \exp \left[\frac{-2.77 (x-c)^2}{\Gamma_{ch}^2} \right] + s(x-c) + B, \quad (1)$$

where: A is the amplitude of the peak

Γ_{ch} is the full width at half maximum (FWHM) of the peak
in channels

c is the peak's center channel location

B is the height of the background in the center channel of
the peak

s is the slope of the background under the peak.

There were some cases however, in which two peaks would be only partially resolved and were therefore fit to the following two-Gaussian expression:

$$g(x) = A \exp \left[\frac{-2.77 (x-c)^2}{\Gamma_{ch}^2} \right] + A' \exp \left[\frac{-2.77 (x-c')^2}{\Gamma'_{ch}{}^2} \right] + s(x-c) + B, \quad (2)$$

where A' , c' and Γ'_{ch} are the amplitude, center and FWHM, respectively, of the second peak.

The functions $f(x)$ and $g(x)$ represent families of curves because of the indefinite values of their parameters. In order to find the member curve which best fit a portion of the data, either Eq. (1) or Eq. (2) was selected as the fitting function depending on the overall appearance of the data, and initial estimates of the parameter values were supplied in the computer program. The program adjusted the values of the parameters and chose as final values those which minimized the dispersion of data about the curve. The measure of the dispersion was taken to be χ^2 which was defined:

$$\chi^2 = \sum_{i=1}^n \left[\frac{y_i - f_i}{\sigma_i} \right]^2, \quad (3)$$

where: f_i is the value of $f(x)$ or $g(x)$ evaluated at the x_i th analyzer channel

y_i is the number of counts in x_i

$$\sigma_i = \sqrt{y_i}$$

n is the number of channels included in the fit.

For a "good" fit, χ^2 should generally take on values within the range

$$\chi^2 = n-p \pm \sqrt{2(n-p)}, \quad (4)$$

where p is the number of free parameters in the fitting function.

Each of the peaks was fit several times, a different number of channels being included in each fit. The various fits were compared for consistency and one was selected to represent the group. The number of channels included in any fit was chosen to be between 2 FWHM and 4 FWHM. A range of less than 2 FWHM was not used since this interval would exclude some of the information contained in the peak and would result in increased uncertainty in the values of the parameters.

In Table III are listed the identity of the various spectral peaks, the type of analysis used in each case, the average number of channels included in the fits, and the average χ^2 which resulted from these fits. The values obtained for χ^2 reflect the reasonable agreement between the shape of the peaks in the spectra and the function chosen to fit them.

B. Energy Determination

Since the spectrometer response was essentially linear, the energy E_u of an unknown spectral peak located in channel x_u is given by:

$$E_u = E_r + M(x_u - x_r) , \quad (5)$$

where E_r and x_r are the energy and center channel of a reference peak and M is the gain of the spectrometer in energy per channel. The gain of the system was determined by means of a calibration source which emitted radiation of energies E_1 and E_2 whose respective peak centers

were located in channels x_1 and x_2 . Thus:

$$M = \frac{E_2 - E_1}{x_2 - x_1} . \quad (6)$$

Furthermore, the calibration source was also used as a reference energy so that Eq. (5) becomes:

$$E_u = E_1 + M(x_u - x_1) \quad (7)$$

The calibration energies were chosen to be two lines of Co^{57} . The higher energy E_2 was the 14.389 ± 0.006 keV nuclear γ -ray.³⁹ The lower energy E_1 was the 6.40 ± 0.001 keV K_{α} x-ray from the source.⁴⁰ (The x-rays are characteristic of Fe^{57} which results after Co^{57} electron captures.) The value chosen for E_1 was an average of the $K_{\alpha 1}$ and $K_{\alpha 2}$ energies weighted in accordance with their relative intensities.⁴¹

The values and errors used for x_1 and x_2 were compensated for drifts. To illustrate: if $x_{1b} \pm \Delta x_{1b}$ was the center channel location of the 6.4 keV peak in the calibration prior to a run and $x_{1a} \pm \Delta x_{1a}$ its location following the run, then x_1 was taken to be:

$$x_1 = \frac{x_{1b} + x_{1a}}{2} \quad (8)$$

and its error taken to be:

$$\Delta x_1 = \left| \frac{x_{1b} - x_{1a}}{2} \right| + \Delta x_{1a} . \quad (9)$$

The first term in Eq. (9) was always the larger of the two. In addition, $\Delta x_{1a} \approx \Delta x_{1b}$ for all cases.

The statistical error on E_u was determined from the following general rule for the propagation of errors.⁴² If several independent quantities w_1, w_2, \dots, w_n having errors $\Delta w_1, \Delta w_2, \dots, \Delta w_n$, respectively, are the independent variables of a function ϕ :

$$\phi = \phi (w_1, w_2, \dots, w_n) , \quad (10)$$

then the error on ϕ is given by

$$(\Delta\phi)^2 = \sum_{i=1}^n \left(\frac{\partial\phi}{\partial w_i} \right)^2 (\Delta w_i)^2 . \quad (11)$$

It follows, therefore, from Eqs. (6) and (7) that:

$$\begin{aligned} (\Delta E_u)^2 &= \frac{(x_u - x_2)^2}{(x_2 - x_1)^2} (\Delta E_1)^2 + \frac{(x_u - x_1)^2}{(x_2 - x_1)^2} (\Delta E_2)^2 + \frac{(E_1 - E_2)^2 (x_u - x_2)^2}{(x_2 - x_1)^4} (\Delta x_1)^2 \\ &+ \frac{(E_1 - E_2)^2 (x_u - x_1)^2}{(x_2 - x_1)^4} (\Delta x_2)^2 + \frac{(E_1 - E_2)^2}{(x_2 - x_1)^4} (\Delta x_u)^2 . \end{aligned} \quad (12)$$

Since there were several "pion runs" and "muon runs", each preceded and followed by a calibration run, a number of independent determinations was made of the energy of each experimental peak ($E_{ui} \pm \Delta E_{ui}$). These measurements were combined to form the weighted average \bar{E}_u given by:

$$\bar{E}_u = \frac{\sum_i E_{ui} (\Delta E_{ui})^{-2}}{\sum_i (\Delta E_{ui})^{-2}}, \quad (13)$$

which had a corresponding error $\Delta \bar{E}_u$ given by:

$$\Delta \bar{E}_u = \left[\sum_i (\Delta E_{ui})^{-2} \right]^{-1/2} \quad (14)$$

The values obtained for the energy \bar{E}_u were corrected for the effects of Compton scattering as will be discussed in Sec. C. The error $\Delta \bar{E}_u$ was enhanced by 0.034 keV because of nonlinear effects that were present in the spectrometer. These nonlinearities will be discussed in Sec. D. The error on the energy was thus given by:

$$\Delta E_u (\text{tot}) = \Delta \bar{E}_u + 0.034 \text{ keV}. \quad (15)$$

C. Correction of Energies for the Effects of Compton Scattering

It will be shown in Sec. VII D that approximately 83% of the helium x-rays which reached the detector would have undergone no Compton scattering in the target, 14% would have undergone single scattering, and 3% would have undergone double scattering. A pionic (muonic) helium x-ray of energy E after undergoing a single Compton scatter has a final energy E' which is given by:

$$E' = \frac{E m_e c^2}{m_e c^2 + E(1 - \cos \theta)}, \quad (16)$$

where θ is the angle between the initial and final photon directions. Neglecting double scattering, the spectrum for the transition consists of x-rays of energy E together with a Compton-scattered spectrum with a range of energies E' given by:

$$\frac{E m_e c^2}{2E + m_e c^2} \leq E' \leq E. \quad (17)$$

The mean energy for this spectrum is then:

$$E'_{\text{mean}} = \frac{E(E + m_e c^2)}{2E + m_e c^2}. \quad (18)$$

Since the resolution of the spectrometer was ≈ 620 eV and the maximum energy degradation of a singly scattered photon was ≈ 700 eV in the energy range of the helium x-rays, the scattered x-rays were included in the unscattered analyzer peak.

Spectral peaks were assumed to be Gaussian and to be superimposed on a linear background for purposes of computer fitting to determine their energies. If half of the number of counts in the Compton scattered peak in this approximation is considered as background and the other half as part of the unscattered radiation, then only about 8% of the scattered radiation can affect the measured energy of the analyzer peak.

The resulting measured energy E_u would then be given by the weighted average of a peak which consists of 91% unscattered radiation of energy E and 9% scattered radiation of energy E'_{mean} . Thus:

$$E_u = 0.91E + 0.09E'_{\text{mean}}. \quad (19)$$

The quantity $\Delta \equiv E - E_u$ represents the value by which the measured energy E_u is decreased from the x-ray energy E . Its value was calculated from Eqs. (18) and (19) and added to \bar{E}_u in order to correct \bar{E}_u for the effects of Compton scattering. The magnitude of the correction ranged from 11 eV at 8.2 keV to 31 eV at 13.5 keV. The error on Δ was assumed to be the same as Δ itself and was combined with $\Delta E_u(\text{tot})$ using Eq. (11).

D. Discussion of Errors

1) Spectrometer nonlinearity

There were two types of nonlinearity inherent in the analyzer:

1. The differential nonlinearity. A measure of the tendency of the individual channels to vary in width from the average channel width.
2. The integral nonlinearity. A measure of the overall non-linear response of the analyzer.

There was an additional contribution to the spectrometer nonlinearity, namely, an inherent nonlinearity in the detector itself. Zulliger and Aitken⁴³ have demonstrated the existence of nonlinearities in similarly

manufactured Si(Li) detectors for photon energies less than 30 keV. These authors claim that this nonlinearity is related to lost carriers near the surface dead layer, this loss presumably due to an increased trapping probability in that region.

The 0.034 keV error which was added to the statistical error in Eq. (15) in order to account for spectrometer nonlinearity was determined from a consistency measurement of a line of known energy. The line was the 10.532 ± 0.001 keV $\text{Se}^{75} K_{\alpha}$ x-ray where, again, the value used for its energy is an average of the $K_{\alpha 1}$ and $K_{\alpha 2}$ energies weighted according to their relative intensities.^{40,41} The Se^{75} and Co^{57} spectra were accumulated simultaneously and resulted in a measured value of the Se^{75} line of 10.498 ± 0.002 keV, the error being statistical only. The measured and known values could be made consistent if 0.034 keV was used as the error of the measured value. Therefore 0.034 keV error was added to all experimentally measured energies. No attempt was made to correct the energies themselves on the basis of the Se^{75} measurement since this test was performed some time after completion of the cyclotron run.

A measurement of the analyzer nonlinearity confirmed the existence of a detector caused contribution to the spectrometer nonlinearity. This measurement was performed during the cyclotron run in order that experimental conditions might be reproduced as much as possible. The gain of the system and other equipment settings were the same as those used during experimental runs.*

* The beam was off at the time of the measurement.

The measurement was made using a 60 Hz mercury switch pulser of a type designed by J. A. Biggerstaff of Oak Ridge National Laboratory. It had a linearity specification of better than 5 parts in 10^5 . The pulser output was ≈ 50 nsec in rise time and 100 μ sec in decay time, thereby simulating the detector pulse. The pulser was coupled to the preamplifier input through a 5 pF test capacitor located within the detector housing. Pulser peaks were accumulated in the analyzer at intervals of 15 channels within the same group of channels in which the helium x-rays were observed. Three sets of pulser data were taken in order to be able to account for drifts. Each of the peaks was fit to a single Gaussian to obtain its center. The average centers of corresponding peaks of the three runs were fit to a straight line of pulser dial setting vs. channel with a least squares program. The results of the fit gave an uncertainty in the slope of the line of 0.2 eV/channel (using the experimental gain of 55.6 eV/channel for the slope of the line). This uncertainty was used to calculate the error $\Delta E_u(\text{nonlin})$ of the energy of a spectral peak due to spectrometer nonlinearity exclusive of a detector caused contribution:

$$\Delta E_u(\text{nonlin}) = |x_u - x_1| \Delta M. \quad (20)$$

During the cyclotron run $|x_u - x_1| \leq 70$ channels and with $\Delta M = 0.2$ eV/channel we obtain $\Delta E_u(\text{nonlin}) \leq 0.014$ keV. The total uncertainty in the energy of a spectral peak, including the detector caused contribution was greater than 0.034 keV and thus it is shown that a detector caused contribution to the spectrometer nonlinearity was present.

2) Background

Since the liquid helium was housed within the cryostat, it was possible that particles stopping in the elements of the cryostat could generate mesic x-rays. If these x-rays were to occur with significant intensities, they could cause systematic errors to arise in the data analysis. From geometrical considerations, the following elements were considered as potential sources of contaminant x-rays.

1. iron — since the target was constructed of stainless steel
2. aluminum — since the liner and detector housing were of aluminum metal
3. oxygen and aluminum — since sapphire is aluminum oxide (the target windows were sapphire) and
4. beryllium — since the x-ray windows were fabricated from beryllium metal.

In order to facilitate the search for contaminant x-rays, the individual pionic spectra were added together, the same being done for the muonic spectra. The resultant summed spectra were then examined visually to determine whether contamination peaks were present. In the pionic summed spectrum there was a peak at 30.5 ± 0.2 keV which contained 720 ± 110 counts.* For comparison, the helium π - K_{α} peak contained 5310 ± 200 counts. This contamination peak was interpreted as being the aluminum π - M_{α} x-ray whose energy was calculated to be ≈ 30.4 keV.† In

* For these purposes, the number of event counts in this and other peaks was determined by summing the total number of counts in the peak and subtracting from it the appropriate number of background counts. The errors are statistical.

† Approximate energy values in this section were calculated using the Bohr formula, this being sufficiently accurate for the discussion.

the muonic summed spectrum, a contamination peak appeared at 33.4 ± 0.2 keV with 100 ± 20 counts. The helium $\mu\text{-K}_\alpha$ line for comparison had 3000 ± 120 counts. This second contamination line was identified as the beryllium $\mu\text{-K}_\alpha$ x-ray, the energy of which was known to be 33.4 keV.⁴⁴ There were no further indications of peaks in the summed spectra other than those of the helium x-rays.

The presence of mesic x-rays from iron in the helium spectra was discounted since the transition energy of interest (≈ 12.0 keV for pions) takes place between states of such high quantum number ($n_i = 8$, $n_f = 7$) that it occurs mainly by a radiationless Auger effect.⁶ That there were no x-rays from aluminum or oxygen within the energy range of the helium x-rays could be confirmed by inspection of the summed spectra since the contaminant x-rays of concern would be sufficiently resolved from the helium lines. The aluminum $\pi\text{-M}_\alpha$ line, having an energy of ≈ 14.1 keV, would occur in channel 369 and the oxygen $\pi\text{-M}_\alpha$, at ≈ 11.5 keV would occur in channel 322 (see Fig. 10). No evidence of either of these lines or their muonic counterparts was seen in the summed spectra.

Since a small amount of beryllium $\mu\text{-K}_\alpha$ contamination was seen in the muonic summed spectrum, the possibility existed that the beryllium $\mu\text{-L}_\beta$ x-ray (≈ 8.33 keV) was contaminating the helium $\mu\text{-K}_\alpha$ line. The beryllium $\mu\text{-L}_\beta$ line was, however, estimated to be present in a negligible amount. This conclusion followed from an independent measurement of the beryllium muonic x-ray spectrum which gave the ratio of the intensity of the $\mu\text{-L}_\beta$ to $\mu\text{-K}_\alpha$ lines of less than 0.03.⁴⁵ It was possible that the helium $\mu\text{-K}_\alpha$ line present in the pionic spectrum (Fig. 10) was contaminated by the beryllium $\pi\text{-L}_\alpha$ line (≈ 8.21 keV). In order to

confirm that this was not the case, the intensity ratio:

$$\frac{I_{\mu-K_{\alpha}}}{I_{\mu-K_{\beta}} + I_{\mu-K_{\gamma}} + \dots} \quad (21)$$

for muonic helium was determined for both the pionic and muonic summed spectra. The ratio was the same in both cases to within statistical errors and therefore indicated negligible contamination.

Another background problem which was considered was the presence of the $\mu-K_{\beta}$ peak adjacent to the $\pi-K_{\alpha}$ peak in the pionic x-ray spectra (Fig. 10). Since these peaks were not fully resolved, both should have been fit simultaneously with a double Gaussian plus linear background function. However, in the individual spectra there were too few counts to permit a double Gaussian fit and therefore the $\pi-K_{\alpha}$ peak was fit to a single Gaussian plus linear background function. That there was no systematic error introduced by fitting the $\pi-K_{\alpha}$ peak alone was confirmed as follows. The $\pi-K_{\alpha}$ peak in the summed spectrum was first fit alone with a single Gaussian function and then together with the $\mu-K_{\beta}$ peak using a double Gaussian function. The $\pi-K_{\alpha}$ peak centers were found to be the same to within statistical errors using either fitting technique. The same was true for the widths.

3) Count Rate Effects

Because of pulse pileup, the channel location of a peak will change as the rate of incidence of radiation on a detector is changed. A measurement of the shift in the center channel location of the 14.389 keV γ -ray peak of Co^{57} as a function of its incident rate was made over a range of rates from $\approx 250 - 10,000$ counts/min. The result of the

measurement can be expressed as follows: if the rate of incidence of Co^{57} γ -rays on the detector was increased by 2000 counts/min, the location of its peak center was shifted ≈ 0.1 channels toward lower energy.

During calibration runs, the beam was left on and the 14.389 keV γ -ray of Co^{57} was incident at a rate of ≈ 550 counts/min. For this rate of incidence of these γ -rays from the source, the location of the center of the calibration peak would be shifted by ≈ 0.03 channels according to the above result. At the experimental gain of 55.6 eV/channel, this represents a shift in energy of the peak of ≈ 1.7 eV and hence an error of approximately the same magnitude in the measurement of the helium x-ray energies. This error, however, is negligible in comparison to other sources of error.

The rate of incidence of the x-rays from the Fe^{55} stabilization source, which was in place only during experimental runs, was ≈ 250 counts/min. Since the rate of incident radiation from the Fe^{55} source was much lower than the rate from the Co^{57} source, it follows that the use of Fe^{55} as a stabilization source introduced negligible count rate errors into energy measurements.

VI. DATA ANALYSIS: NATURAL LINEWIDTHS

A. Introduction

The linearity of the spectrometer insures that photons of a given energy which are incident on the detector result on the average in counts being stored in the analyzer channel which corresponds to that energy. However, because of the finite resolution of the spectrometer, a distribution of energies about the incident photon energy is recorded. Radiation arising from transitions between discrete nuclear or atomic states is not monoenergetic but possesses a characteristic energy distribution. Thus both the finite resolution of the spectrometer and the natural linewidth of the radiation affect the shape of a spectral peak.

The shape of a spectral peak can be described mathematically⁴⁶ by associating with an analyzer count a random variable \underline{E} (random variables are denoted by underscoring). To the random variable there corresponds a probability density function $f(E)$ such that the probability that \underline{E} assumes a value between E and $E + dE$ is given by $f(E)dE$. The shape of the spectral peak $F(E)$ is then:

$$F(E) = \text{constant} \times f(E) , \quad (1)$$

where the proportionality constant normalizes the probability density function to the number of counts in the peak.

In determining $f(E)$, use is made of the fact that if two independent random variables \underline{x}_1 and \underline{x}_2 are related to a third \underline{y} through

$$\underline{y} = \underline{x}_1 + \underline{x}_2, \quad (2)$$

then the probability density function $f(y)$ corresponding to \underline{y} is given by the convolution integral

$$f(y) = \int_{-\infty}^{\infty} f_1(y - x_2) f_2(x_2) dx_2, \quad (3a)$$

or equivalently

$$f(y) = \int_{-\infty}^{\infty} f_1(x_1) f_2(y - x_1) dx_1, \quad (3b)$$

where $f_1(x_1)$ and $f_2(x_2)$ are the probability density functions corresponding to \underline{x}_1 and \underline{x}_2 , respectively. Thus if \underline{E} is considered as the sum of a number of independent random variables whose probability density functions are known, a series of convolutions can be performed in order to yield $f(E)$.

B. Determination of Peak Shapes

1) Photon Emission Line Shape

The time dependent part of the wave function of a quantum state of energy E_j , having a mean life τ_j , is proportional to

$$\exp(-iE_j t/\hbar) \exp(-t/2\tau_j). \quad (4)$$

The probability that the state is occupied after a time t is then

$$\exp(-t/\tau_j). \quad (5)$$

The probability that the state has an energy E between E and $E + dE$ is given by:

$$L(E, \Gamma_j) dE = \frac{\Gamma_j}{2\pi} \frac{dE}{(E-E_j)^2 + (\Gamma_j/2)^2}, \quad (6)$$

where

$$\Gamma_j \equiv \hbar/\tau_j. \quad (7)$$

The probability distribution function $L(E, \Gamma_j)$ is seen to be Lorentzian with a FWHM given by Γ_j .

If a state of energy E_i , having a long mean life against radiative decay compared to τ_j , undergoes a radiative transition to the state E_j , the resultant distribution of photon energies is given by:

$$L(E_\gamma, \Gamma_{\text{nat}}) dE_\gamma = \frac{\Gamma_{\text{nat}}}{2\pi} \frac{dE_\gamma}{(E_\gamma - E_{ij})^2 + (\Gamma_{\text{nat}}/2)^2} \quad (8)$$

where: $\Gamma_{\text{nat}} = \Gamma_j$ is the FWHM or natural linewidth of the distribution
 $E_{ij} = E_i - E_j$ is the mean energy difference between the two states.

In pionic He^4 , the mean life of the 2p state against radiative decay is $\approx 4 \times 10^{-13} \text{ sec}^{47}$ while the mean life of the 1s state against nuclear capture is $\approx 10^{-17} \text{ sec}$ [Sec. II, Eq. (36)]. Thus the $\pi\text{-K}_\alpha$ emission line from He^4 can be described by the random variable \underline{E}_γ whose corresponding probability density function is $L(\underline{E}_\gamma, \Gamma_{\text{nat}})$ of Eq. (8). The natural linewidth Γ_{nat} of the $\pi\text{-K}_\alpha$ transition is equal to the natural linewidth of the 1s level and $E_{ij} = E_{\pi\text{-K}_\alpha}$, where $E_{\pi\text{-K}_\alpha}$ is the 2p-1s transition energy.

2) Instrumental Line Shape

There are two sources of instrumental broadening of spectral peaks. The first is spectrometer noise and the second is the statistical fluctuations in the number of electron-hole pairs produced in the charge conversion process by which a photon loses its energy in the detector.

The most important component of spectrometer noise is the largely thermal noise which is generated in the detector and input components to the preamplifier, since this noise undergoes maximum amplification. The noise results in random fluctuations of the zero-voltage level (base line) of the amplifier. From the effects of noise, an analyzer peak would exhibit a Gaussian distribution in energies. The random variable $\underline{\Delta E}_{\text{noise}}$ in this case describes the deviation in energy of analyzer counts from the incident photon energy. Its corresponding normalized Gaussian distribution is:

$$G_1(\underline{\Delta E}_{\text{noise}}, \Gamma_{\text{noise}}) = \left(\frac{\pi}{4 \ln 2}\right)^{\frac{1}{2}} \Gamma_{\text{noise}} \exp \left[-4 \ln 2 \left(\frac{\underline{\Delta E}_{\text{noise}}}{\Gamma_{\text{noise}}} \right)^2 \right], \quad (9)$$

where Γ_{noise} is the FWHM of the distribution.

The fluctuations in the number of electron-hole pairs produced in the charge conversion process result in variations of the amount of charge deposited at the preamplifier input. As a consequence of this, there is a distribution in energy of analyzer counts about the incident photon energy. The shape of this distribution resulting from the charge conversion process is related to a Poisson distribution.⁴⁸ Since the Poisson distribution for a large number of events approximates a Gaussian distribution, we assume this shape to be Gaussian. Thus, the random variable $\underline{\Delta E}_{\text{det}}$ describes the distribution in energy of analyzer counts about the incident photon energy due to the charge conversion process. The corresponding distribution is:

$$G_2(\Delta E_{\text{det}}, \Gamma_{\text{det}}) = \left(\frac{\pi}{4 \ln 2} \right)^{1/2} \Gamma_{\text{det}} \exp \left[-4 \ln 2 \left(\frac{\Delta E_{\text{det}}}{\Gamma_{\text{det}}} \right)^2 \right], \quad (10)$$

where Γ_{det} is the FWHM of the distribution.

Since both sources of broadening are present in the spectrometer, the resultant distribution in energy of analyzer counts about the incident photon energy is described by the random variable $\underline{\Delta E}_{\text{inst}}$, where:

$$\underline{\Delta E}_{\text{inst}} = \underline{\Delta E}_{\text{noise}} + \underline{\Delta E}_{\text{det}}. \quad (11)$$

The corresponding distribution is the convolution of the functions G_1 and G_2 which gives the well known result — a Gaussian distribution:

$$G_3(\Delta E_{\text{inst}}, \Gamma_{\text{inst}}) = \left(\frac{\pi}{4 \ln 2} \right)^{\frac{1}{2}} \Gamma_{\text{inst}} \exp \left[-4 \ln 2 \left(\frac{\Delta E_{\text{inst}}}{\Gamma_{\text{det}}} \right)^2 \right], \quad (12)$$

where:

$$\Gamma_{\text{inst}} = \left[(\Gamma_{\text{noise}})^2 + (\Gamma_{\text{det}})^2 \right]^{\frac{1}{2}}. \quad (13)$$

Γ_{inst} , termed the instrumental width, is the FWHM of the distribution.

Agreement between the assumed instrumental line shape and actual line shape is reflected in the satisfactory values obtained for χ^2 as a result of the least squares fit to the Co^{57} γ -ray line (see Table III). It should be noted that the natural linewidth of the Co^{57} γ -ray is negligible.

3) Resultant Peak Shape

The determination of the energy distribution of the $\pi\text{-K}_\alpha$ spectral peak results from a convolution of the distribution functions governing the natural and instrumental line shape. The relationship among the random variables is:

$$\underline{E} = \underline{E}_\gamma + \underline{\Delta E}_{\text{inst}}. \quad (14)$$

where \underline{E} represents the random variable corresponding to the observed energy. The distribution function corresponding to \underline{E}_γ is given by Eq. (8) where $E_{ij} = E_{\pi\text{-K}_\alpha}$ and Γ_{nat} is the 1s level width of the pionic He^4 atom. From Eqs. (3), (8) and (12), then, $f(E)$ is given by:

$$f(E) = \int_{-\infty}^{\infty} dE_{\gamma} \frac{\Gamma_{\text{nat}}}{2\pi} \left[\frac{1}{(E_{\gamma} - E_{\pi-K_{\alpha}})^2 + (\Gamma_{\text{nat}}/2)^2} \right] \\ \times \left[\left(\frac{\pi}{4 \ln 2} \right)^{1/2} \Gamma_{\text{inst}} \exp \left[-4 \ln 2 \left(\frac{E - E_{\gamma}}{\Gamma_{\text{inst}}} \right)^2 \right] \right], \quad (15)$$

from which $F(E) \equiv Af(E)$ can be written:

$$F(E) = A \int_{-\infty}^{\infty} dx (1 + x^2)^{-1} \exp \left[- \left(\frac{2\Gamma_{\text{nat}}^{-1} (E - E_{\pi-K_{\alpha}}) - x}{\eta} \right)^2 \right], \quad (16)$$

where: $x \equiv \frac{2}{\Gamma_{\text{nat}}} (E_{\gamma} - E_{\pi-K_{\alpha}}), \quad (17)$

$$\eta = \frac{\Gamma_{\text{inst}}}{\Gamma_{\text{nat}} (\ln 2)^{1/2}}, \quad (18)$$

and A is a constant. The integral of Eq. (16) is termed the Voigt integral and the resultant line shape $F(E)$, a Voigt profile. The integral cannot be evaluated in closed form but has been numerically integrated by Davies and Vaughan⁴⁹ for a number of specific values of the parameter η which characterizes a profile.

The results of Davies and Vaughan are tabulated in such a way as to permit a determination of Γ_{nat} . They define the Gaussian fraction G by:

$$G \equiv \frac{\Gamma_{\text{inst}}}{\Gamma_{\text{v}}} , \quad (19)$$

where Γ_{v} is the FWHM of the Voigt profile. For a given G there corresponds a unique Lorentzian fraction L :

$$L \equiv \frac{\Gamma_{\text{nat}}}{\Gamma_{\text{v}}} . \quad (20)$$

These quantities, reproduced from the table of Davies and Vaughan, are presented in Table IV. Thus it is seen that knowledge of the instrumental width Γ_{inst} of the spectrometer and of the total width Γ_{v} of a spectral peak determines the natural linewidth Γ_{nat} .

C. The Pionic 1s Level Width

For each of the pionic x-ray runs, the $\pi\text{-K}_{\alpha}$ and $\mu\text{-K}_{\alpha}$ peaks of the resulting spectrum were fit to single Gaussian functions with linear background terms. The resulting FWHM of a peak in energy units Γ_{eng} was expressed in terms of its FWHM in channels Γ_{ch} using:

$$\Gamma_{\text{eng}} = M\Gamma_{\text{ch}} , \quad (21)$$

where M is the gain of the spectrometer in units of energy per channel. Since little, if any, broadening of the $\pi\text{-K}_{\alpha}$ line was indicated, the

Gaussian approximation to its Voigt profile was considered to be satisfactory. Accordingly the FWHM resulting from the computer fit was chosen as Γ_v . The FWHM of the μ -K $_{\alpha}$ line in the pionic spectrum was chosen to be the instrumental width Γ_{inst} since its natural line-width is negligibly small ($\sim 10^{-10}$ eV). In addition, the selection of the μ -K $_{\alpha}$ peak as a measure of the instrumental width eliminated many sources of systematic error since it was accumulated simultaneously with the pionic x-ray data. Γ_{nat} was determined by using the values thus obtained for Γ_{inst} and Γ_v to derive G. The value of L corresponding to G was obtained by a linear interpolation of Table IV whence Γ_{nat} followed from Eq. (20).

The error on Γ_{nat} was determined as follows. The error in energy of either the instrumental width Γ_{inst} or Voigt width Γ_v is given by:

$$\Delta\Gamma_{eng} = \Gamma_{eng} \left[\left(\frac{\Delta\Gamma_{ch}}{\Gamma_{ch}} \right)^2 + \left(\frac{\Delta M}{M} \right)^2 \right]^{1/2}, \quad (22)$$

Since, in interpolation, L was approximately a linear function of G, Γ_{nat} can be expressed using Eqs. (19) and (20) as:

$$\Gamma_{nat} = A_1 \Gamma_{inst} + A_2 \Gamma_v, \quad (23)$$

where A_1 and A_2 are constants whose values depend upon the two known pairs of G and L in Table IV between which the interpolation was made. Thus the error on Γ_{nat} was thus given by:

$$\Delta\Gamma_{\text{nat}} = \left[A_1^2 (\Delta\Gamma_{\text{inst}})^2 + A_2^2 (\Delta\Gamma_{\text{v}})^2 \right]^{1/2} \quad (24)$$

Each of the pion runs yielded a value and error for the natural width of the $\pi\text{-K}_\alpha$ transition. The resultant value was taken to be a weighted average of all the runs. In those cases where the $\mu\text{-K}_\alpha$ line exhibited a larger width than the corresponding $\pi\text{-K}_\alpha$ line, the FWHM of the $\mu\text{-K}_\alpha$ was taken to be Γ_{v} and the FWHM of the $\pi\text{-K}_\alpha$ was taken to be Γ_{inst} . This was done in order that the results would not be weighted in favor of a positive Γ_{nat} .

The spectrometer resolution is a function of energy and its dependence thereon was measured in the laboratory by accumulating simultaneously a spectrum from the sources of Co^{57} and Se^{75} . The results of the measurement are shown in Fig. 13 which indicates a relative increase in instrumental width of 4.8 eV for each keV of incident energy. Since the $\mu\text{-K}_\alpha$ and $\pi\text{-K}_\alpha$ lines are separated by 2.5 keV, this indicates that the instrumental width at the energy of the $\pi\text{-K}_\alpha$ peak was larger by 12 eV than the instrumental width at the energy of the $\mu\text{-K}_\alpha$ peak. The correction to the natural width appropriate to this observed increase in instrumental width was 20 eV, this amount accordingly was subtracted from the resultant Γ_{nat} .

In Table V are listed the results of the measurements of the natural linewidth of the $\pi\text{-K}_\alpha$ line. Negative linewidths are shown for those cases in which the FWHM of the $\mu\text{-K}_\alpha$ line was larger than that of the $\pi\text{-K}_\alpha$. The resultant value is $\Gamma_{\text{nat}} = 10 \begin{smallmatrix} + 60 \\ - 10 \end{smallmatrix}$ eV where the quoted error is one standard error.

It should be noted that the natural linewidth reported in Table V for the July 1967 cyclotron run ($\Gamma_{\text{nat}} = 160 \pm 100$ eV) is different from the previously reported value³⁵ of 0 ± 86 eV. The reason for this is that in determining the previously reported value, the FWHM of the $\mu\text{-K}_{\alpha}$ line from the muon run was chosen as the measure of the instrumental width.

D. Negligible Sources of Error

1) Integral Nonlinearity

The overall nonlinearity of the spectrometer leads to an uncertainty in the gain M . Simultaneous accumulation of a Co^{57} and Se^{75} spectrum permitted a measurement of the uncertainty. A gain M_1 was determined using the 6.4 keV and 14.389 keV Co^{57} lines in the spectrum and another, M_2 , using the 6.4 keV line of Co^{57} and the 10.532 keV line of Se^{75} . The uncertainty in the gain of the system was estimated from:

$$\frac{\Delta M}{M} \approx \frac{|M_1 - M_2|}{M_1} = 0.009 . \quad (25)$$

By comparison, the statistical error on the FWHM of a typical analyzer peak was $\Delta\Gamma_{\text{ch}}/\Gamma_{\text{ch}} \approx 0.1$. From Eq. (22) it is seen that the nonlinearity of the spectrometer contributes negligibly to $\Delta\Gamma_{\text{eng}}$ and therefore negligibly to $\Delta\Gamma_{\text{nat}}$.

2) Drifts

Since calibration spectra were obtained before and after each experimental run, drifts of the spectrometer and their effect on peak widths could be evaluated. Spectrometer drifts were found to be random

in nature; i.e. the center channel location of the calibration peaks fluctuated about some mean value during the course of the cyclotron run. Drifts were caused mainly by variations in the system gain. Thus, the amount of drift which a peak underwent was dependent upon its energy.

Since the $\mu\text{-K}_\alpha$ and $\pi\text{-K}_\alpha$ lines which were used in order to measure Γ_{nat} were accumulated simultaneously, both peaks were subject to the same gain variations during the time of data accumulation. Therefore, only relative drifting between the two peaks had an effect on the measurement of Γ_{nat} .

If M_b is the system gain in energy per channel as determined by a calibration taken prior to an experimental run, M_a the gain as determined after the run, and x_{2b} and x_{2a} the center channel locations of the upper calibration peak (energy E_2) before and after the run, respectively, then the drift in channels of an experimental spectrum peak (energy E_u) can be estimated from:

$$\Delta x_u = x_{2b} - x_{2a} + (M_a^{-1} - M_b^{-1}) (E_2 - E_u). \quad (26)$$

The largest drifts in a particular run which were observed resulted in an estimated drift of the center of a $\mu\text{-K}_\alpha$ line of 1.06 channels and of a $\pi\text{-K}_\alpha$ line center of 1.36 channels. A typical peak width of 11 channels and a system drift that is Gaussian results in a FWHM of the $\mu\text{-K}_\alpha$ peak of $[(11)^2 + (1.06)^2]^{\frac{1}{2}} = 11.05$ channels and of the $\pi\text{-K}_\alpha$ peak of 11.08 channels. At the experimental gain of 55.6 eV/channel this

would introduce a relative difference of 2 eV between the widths of the two peaks. This error is negligibly small in comparison to the statistical errors on the measured widths (see Table V).

3) Finite Channel Width and Differential Nonlinearity

The effect of the finite width of analyzer channels on the measured width of a peak was determined as follows. A number of Gaussian functions each having the same amplitude and a FWHM of 11 channels but with centers located at intervals of 0.1 channel apart were used with a computer program to generate a corresponding number of analyzer peaks. Then, with the least squares fitting program, each peak was fit to a single Gaussian function and the spread in widths which resulted was seen to be less than 1 eV.

Since the differential nonlinearity of the system is a measure of the tendency of individual channels to fluctuate about a mean channel width and is a 2% effect according to specifications, the error introduced into the measurement of a peak width was considered to be of the same order of magnitude as the error due to the finite channel width.

Therefore, in comparison to the statistical errors on the measured widths, these sources of error are negligible.

4) Molecular Effects

If molecular effects such as Doppler and collision broadening, due to the motions of the pionic and muonic atoms in the liquid helium, affected the experimental spectra, they would have broadened both the $\mu\text{-K}_\alpha$ and $\pi\text{-K}_\alpha$ peaks equally. That the experimental peaks were comparable in width to the calibration peaks indicated that molecular effects were small.

VII DATA ANALYSIS: YIELDS

A. Experimental Arrangement

A brief recapitulation of the experimental arrangement used for the yield measurement is presented here in order to bring together items pertinent to the discussion of yields.

A schematic representation of the experimental arrangement is shown in Fig. 14. The diagram defines a coordinate system in which the beam travels along the negative x direction and the partition of the liner is located in the y-z plane. The beam entered the helium target after passing through a 3" x 3" lead collimator. Pulses originating in compartment 5 were set in the anticoincidence mode in the beam telescope circuit such that a particle-stop signature was given by 1234 $\bar{5}$ $\bar{6}$. This arrangement restricted the effective target to a region of compartment 4 which was 3" in length both in the y and z direction and whose length in the x direction was bounded by the cylinder wall of the liner. The effective target region for the 3" x 3" yield geometry is indicated by the dotted lines in the figure. The effective target volume V_{eff} depends upon the collimator size and its position relative to the target. For a 3" x 3" yield geometry with the collimator centered on the target, the effective volume is 404 cm³. An analyzable event was a particle-stop signature in coincidence (resolving time \approx 250 ns) with a detector pulse.

The x-rays were transmitted from the liquid helium to the Si(Li) detector through a series of four high transmission windows which are also shown in Fig. 14. The first was a 50 mil beryllium window which was sealed to the target, the second a 0.5 mil aluminized Mylar window

in the radiation shield, the third a 10 mil beryllium window which was sealed to the vacuum jacket, and the fourth a 10 mil beryllium window in the detector housing. The 50 mil beryllium window was 2½" in diameter, this dimension being defined by an annular stainless steel ring. Certain regions of the target could not be "seen" by the detector due to the limited aperture of this window.

The Si(Li) detector was 56 mm² in area* by 3 mm in depth and was placed to the side of the beam path at a distance of 1.81" from the 50 mil beryllium window. It was displaced 0.25" from the y-z plane toward compartment 4 in order that the partition between the compartments would not obstruct x-rays directed toward the detector.

B. Derivation of Yield Expression

If $n_i(\vec{x})$ is the density of stopping particles at the location of the i^{th} volume element ΔV_i of the target, then the number of x-rays N_i from that element which arrive at the detector is given by:

$$N_i = n_i(\vec{x}) \cdot \Delta V_i \cdot Y(E) \cdot \epsilon_{sa,i}(\vec{x}) \cdot \epsilon_{msk,i}(\vec{x}) \cdot \epsilon_{tr,i}(\vec{x}, E) \cdot \epsilon_{det}(E) , \quad (1)$$

where: $Y(E)$ is the number of x-rays of energy E emitted per stopped particle (yield),

$\epsilon_{sa,i}(\vec{x}) = d\Omega_i/4\pi$ is the solid angle efficiency of the i^{th} volume element,

$\epsilon_{msk,i}(\vec{x})$ is the amount of masking by the annulus of the 50 mil beryllium window,

* 56 mm² is the measured value of the detector area (see Sec. C).

$\epsilon_{tr,i}(\vec{x},E)$ is the transmission efficiency of the liquid helium, exit windows, and air between the volume element and detector,

$\epsilon_{det}(E)$ is the detector efficiency for photon detection and includes the transmission efficiency of the 10 mil beryllium window on the detector housing, the p-type silicon dead layer and the thin layer of gold on the surface of the detector.

Assuming that the effective target volume is subdivided into M equal volume elements ΔV , defining

$$\epsilon_{t,i}(\vec{x},E) \equiv \epsilon_{sa,i} \cdot \epsilon_{msk,i} \cdot \epsilon_{tr,i} , \quad (2)$$

and summing Eq. (1) over the M elements, we obtain the total number of x-rays N_t of energy E detected during a yield run:

$$N_t(E) = V_{eff} \cdot Y \cdot \epsilon_{det} \cdot \frac{1}{M} \sum_{i=1}^M n_i \epsilon_{t,i} , \quad (3)$$

where $V_{eff} = M\Delta V$ is effective target volume.

If the average density of stopping particles in the effective target volume is given by:

$$\bar{n} = \frac{1}{M} \sum_{i=1}^M n_i , \quad (4)$$

then we can define the average system efficiency ϵ_{avg} of the system by:

$$\epsilon_{\text{avg}} \equiv \frac{1}{\bar{n}} \frac{1}{M} \sum_{i=1}^M n_i \epsilon_{t,i} \quad (5)$$

We then obtain the following expression for the yield $Y(E)$ of x-rays of energy E :

$$Y(E) = \frac{N_t(E)}{N_r \epsilon_{\text{det}} \epsilon_{\text{avg}}} \quad (6)$$

where $N_r \equiv \bar{n} V_{\text{eff}}$ is the total number of particles stopped during the yield run.

The error ΔY on the yield is then:

$$\Delta Y = Y \left[\left(\frac{\Delta N_t}{N_t} \right)^2 + \left(\frac{\Delta N_r}{N_r} \right)^2 + \left(\frac{\Delta \epsilon_{\text{det}}}{\epsilon_{\text{det}}} \right)^2 + \left(\frac{\Delta \epsilon_{\text{avg}}}{\epsilon_{\text{avg}}} \right)^2 \right]^{1/2} \quad (7)$$

C. Detector Efficiency

The transmission efficiency of a substance is given by:

$$\epsilon_s(E) = \exp(-\mu_s(E) \rho_s x_s), \quad (8)$$

where μ_s , ρ_s , and x_s are the mass absorption coefficient, density, and thickness, respectively, of the substance.*

* All mass absorption coefficients are assumed to be known. A discussion of the methods used to determine various coefficients is given in Appendix A.

The detector efficiency is given by:

$$\epsilon_{\text{det}}(E) = \epsilon_{\text{Be}}(E) \cdot \epsilon_{\text{Au}}(E) \cdot \epsilon_{\text{Si}}(E) , \quad (9)$$

where ϵ_{Be} , ϵ_{Au} , and ϵ_{Si} are the transmission efficiencies of the 10 mil beryllium window on the detector housing, gold layer, and p-type silicon dead layer, respectively. In principle, there was sufficient information available to allow a determination of the detector efficiency since its specifications were:

1. gold layer thickness: 500 Å
2. p-type silicon dead layer thickness: 1μ
3. detector thickness: 3 mm
4. detector area: 80 mm².

However, the detector specifications were nominal, with the values for the detector area and silicon dead layer thickness subject to the following qualifications:

1. Although the detector cross sectional area as defined by the physical dimensions of the detector was 80 mm², its effective cross sectional area as defined by the sensitive region of the detector, decreases adjacent to the side of the detector through which the x-rays enter.
2. Since lithium tends to continue drifting, the dead layer thickness increases with time if the detector is stored at room temperature or left unbiased.⁵⁰

These effects are important for low energy photons. The half thickness of silicon for a photon beam of energy of 6.4 keV is 26μ. At 14.4 keV the half thickness is 260μ. Thus, variations in dead layer thicknesses on the order of microns will affect the detector efficiency in the range of the above energies.

The observed intensity ratio of Co⁵⁷ K x-rays (approximately 6.4 keV in energy) to 14.4 keV γ -rays depends on the detector efficiency or, equivalently, on the detector specifications. This ratio was found to vary among detectors having the "same" specifications, which indicated the nominal nature of the specifications. Different thicknesses of gold layers were excluded as a cause of the variations since it was observed that one particular detector whose gold layer was thicker than the gold layer on the detector used in this experiment provided a higher Co⁵⁷ K x-ray to γ -ray ratio. Thus an investigation of the detector efficiency was undertaken, the course of which is outlined below.

The thickness of the gold layer was assumed to be known from the specifications; the p-type silicon dead layer thickness and the detector area were assumed to be unknown. A measurement of the dead layer thickness and area was made by using a Co⁵⁷ source of known radioactivity. The detector efficiency was calculated as a function of energy from Eq. (9) using the dead layer thickness as measured.

1) Experimental

If a radioactive source emits N_0 photons when positioned at a distance d from a detector which is circular in cross sectional area, having a radius r and a half thickness much less than the detector thickness, then the number of photons detected is given by:

$$N = \frac{N_0 \epsilon_{\text{det}}}{2} \left[1 - \frac{d}{(d^2 + r^2)^{1/2}} \right], \quad (10)$$

which for $r \ll d$ becomes:

$$N = \frac{N_o \epsilon_{det} A}{4\pi d^2} \quad (11)$$

where A is the cross sectional area of the detector.

The error introduced in N by the assumption of $r \ll d$ was less than 1% for the geometry which was used in the efficiency measurement.

In order to perform the efficiency measurement, a calibrated Co^{57} source (IAEA, Vienna), having an activity of $(1.74 \pm 0.03) \times 10^5$ disintegrations per second, was placed at a distance of 2.19 ± 0.02 inches from the detector and its spectrum was accumulated for one hour. The number of K x-rays emitted by the source was $N_{ox} = (24.0 \pm 0.8) \times 10^7$ and the number of 14.4 keV γ -rays was $N_{o\gamma} = (5.28 \pm .2) \times 10^7$. These results follow from the discussion of Appendix B. (These numbers have been corrected for the absorption by the 18 mg/cm^2 of polyethylene of the source holder and by the air between the source and detector.)

The number of K x-rays N_x detected was $(1.62 \pm 0.02) \times 10^5$ and the number of 14.4 keV γ -rays N_γ was $(6.90 \pm 0.06) \times 10^4$. The number of x- and γ -rays detected was determined by a least squares fit of the spectrum peaks. The function used to fit the 14.4 keV peak was a single Gaussian with a linear background term; the function used to fit the x-ray peaks was two Gaussians with a linear background term. The number of counts in a peak of amplitude B and full width at half maximum Γ is then given by:

$$N = \left(\frac{\pi}{2.77} \right)^{\frac{1}{2}} B\Gamma \quad (12)$$

2) Results

The thickness of the silicon dead layer was determined from Eqs. (9) and (11) by assuming that the effective area of the detector was not a function of energy in the 6.4 to 14.4 keV region. Thus:

$$\frac{\epsilon_{\text{Si}}(6.4)}{\epsilon_{\text{Si}}(14.4)} = \frac{\epsilon_{\text{Au}}(14.4)}{\epsilon_{\text{Au}}(6.4)} \frac{\epsilon_{\text{Be}}(14.4)}{\epsilon_{\text{Be}}(6.4)} \frac{N_{\text{x}}}{N_{\text{ox}}} \frac{N_{\text{o}\gamma}}{N_{\gamma}} . \quad (13)$$

Using Eq. (8), we then obtain the dead layer thickness $x_{\text{Si}} = 22 \pm 4\mu$. Using this value in Eq. (9), we calculate the detector efficiency for each of the pionic and muonic x-ray energies. The results are listed in the second column of Table VI.

The detector area was obtained from Eq. (11). The result obtained using the K x-rays was $A = 56 \pm 7 \text{ mm}^2$ and the result using the 14.4 keV γ -ray was $A = 56 \pm 2 \text{ mm}^2$. These results are seen to justify the assumption that the effective detector area was not a function of energy.

D. The Average Efficiency of the System

During the energy runs, the collimation was less restrictive (4" x 4" rather than 3" x 3") than during the yield runs. In addition, particles stopping in either compartment were accepted as stops by the beam telescope logic. Under energy run conditions, only about 3% of the particles after having entered the helium, scattered in such a way as to come to rest in the 50 mil beryllium window at the end of the target region. This was determined from the intensity of the beryllium x-rays which contaminated the muonic helium spectrum. On the basis of

the small number of scatterings observed in the energy runs and the fact that with the yield run geometry particles would tend to out-scatter to an even lesser degree, scattering of particles out of the helium target was assumed negligible.

2) Stopping Distribution

We define three dimensionless functions $\alpha_x(x)$, $\alpha_y(y)$ and $\alpha_z(z)$ through:

$$n_i = K \alpha_x(i) \alpha_y(i) \alpha_z(i) , \quad (14)$$

where n_i is the density of stopping particles and K is a normalization constant. Eq. (5) can then be written:

$$\epsilon_{\text{avg}} = \frac{M^{-1} \sum_{i=1}^M K \alpha_x(i) \alpha_y(i) \alpha_z(i) \epsilon_{t,i}}{M^{-1} \sum_{i=1}^M K \alpha_x(i) \alpha_y(i) \alpha_z(i)} . \quad (15)$$

The form of Eq. (15) allows the observed nonuniform stopping distribution of particles to be taken into account.

Since the target thickness was 0.87 g/cm^2 which was much smaller than the spread of the beam (4.2 g/cm^2 FWHM), α_x was set equal to a constant. In order to determine the stopping distributions in the y and z directions, a $2'' \times 2''$ collimation was provided for the target and the number of stops per 10^6 $12'$ s was recorded for a number of different locations of the center of the collimator. The result for each location

was divided by the effective target volume for that location thereby giving the density of stops in terms of the number of 12's. In Fig. 15a, the stopping density vs. the z coordinate location of the collimator center is shown. Only a 14% variation in stopping density is noted. In Fig. 15b, however, a substantial variation in stopping density is seen at various y coordinate locations of the collimator center. Since the variation in stopping density was small along the z direction as compared to that along the y direction and since ϵ_{avg} is more sensitive to variations of the value of α_y than of α_z , α_z was taken to be constant. Eq. (15) therefore becomes:

$$\epsilon_{avg} = \frac{M^{-1} \sum_{i=1}^M \alpha_y(i) \epsilon_{t,i}}{M^{-1} \sum_{i=1}^M \alpha_y(i)} . \quad (16)$$

The function:

$$\alpha_y(y) = 1 - \exp[0.7 (y - 11.3)] \quad (17)$$

was chosen to fit the data. The solid line in Fig. 15a is α_y multiplied by 780. Substitution of Eq. (17) into Eq. (16) allows a direct determination of the denominator since:

$$\frac{1}{M} \sum_{i=1}^M \alpha_y(i) = \frac{1}{y_2 - y_1} \int_{y_1}^{y_2} \alpha_y(y) dy \quad (18)$$

where $y_2 - y_1$ is the length of the effective target region in the y direction.

3) Monte Carlo Calculation

A Monte Carlo calculation, programmed for the IBM S/360 computer, was developed in order to determine ϵ_{avg} as given by Eq. (16). The following outlines the major aspects of the calculation:

1. The detector surface was subdivided mathematically into 56 squares of 1 mm^2 area.
2. A random point i was chosen inside the effective target region. The extent of the region in the y and z directions was chosen to be 3" x 3" according to the collimator dimensions.
3. For each of the 1 mm^2 detector elements, the solid angle efficiency with respect to the random point was calculated and then all elemental solid angles were summed in order to find the solid angle efficiency at the random point. Further, if the 50 mil beryllium window annulus was interposed between the random point and any of the detector elements, the elemental solid angle was set equal to zero in the above summation. In this manner the masking of the beryllium window aperture was taken into account and $\epsilon_{\text{sa},i} \cdot \epsilon_{\text{msk},i}$ was determined for the random point.
4. The transmission efficiency was calculated from the random point to the center of the detector using [see Eq.(8)]

$$\begin{aligned} \epsilon_{\text{tr},i} &= \exp(-\mu_{\text{He}} \rho_{\text{He}} x_{\text{He}} - \mu_{\text{Be}} \rho_{\text{Be}} x_{\text{Be}} - \mu_{\text{air}} \rho_{\text{air}} x_{\text{air}}) \\ &= \epsilon_{\text{t},i} / (\epsilon_{\text{sa},i} \cdot \epsilon_{\text{msk},i}). \end{aligned} \tag{19}$$

The mass absorption coefficients used were exclusive of a Compton scattering contribution.

5. The function $\alpha_y(y)$ was evaluated at the random point, thus allowing the evaluation of one term in the series given by Eq. (16).
6. The sequence given by steps 2 through 5 was repeated for 5000 random points. This insured a convergence of the resultant value of ϵ_{avg} to within 1%.

The Monte Carlo calculation was carried out for each of the x-ray energies. The values of ϵ_{avg} as calculated with the computer program were corrected for the effect of beam dispersion in the target. The magnitude of the correction will be discussed in Sec. 4. The effect of Compton scattering will be discussed in Sec. 5.

4) Correction and Error of ϵ_{avg} for Beam Dispersion

Since the stopping beam underwent some dispersion in the target, an effective target region other than the one defined by the dimensions of the collimator should be used in order to calculate ϵ_{avg} . A correction to the average system efficiency for beam dispersion was made as follows. The average system efficiency ϵ_{avg} was calculated for a uniform stopping distribution ($\alpha_y = \text{constant}$) first for the effective target region defined by the collimator dimensions (3" x 3") and then for the effective target region defined by the dimensions of the liner (5-3/4" x 5-3/4"). The size of the larger effective target region is consistent with the assumption that no particles were scattered out of the target.

The results showed that ϵ_{avg} decreased by an average of 10% when the larger effective target region was used in the calculations. A

correction was made to the values of ϵ_{avg} as determined in Sec. 3 for beam dispersion by decreasing each by 5%. A conservative error of 5% was applied to ϵ_{avg} because of uncertainty in the amount of beam dispersion in the target.

5) Compton Scattering Effects

The Compton scattering cross section is a slowly varying function of energy in the energy region of the helium x-rays.⁵¹ In this energy range, it can be expressed as $\mu_c = 0.189 \text{ cm}^2/\text{g}$ for He^4 . If x-rays which originate in the target have to travel an average distance of \bar{x}_{He} before reaching a target wall, the fractional number which undergo a Compton scatter before reaching the wall is given by:

$$f = 1 - \exp(-\mu_c \rho_{\text{He}} \bar{x}_{\text{He}}). \quad (20)$$

From the geometry of the target, \bar{x}_{He} was estimated to be 3.3" and thus from Eq. (20) we obtain $F = 0.18$.

It was shown in Sec. VB that since scattered helium x-rays lose insufficient energy to be resolved from unscattered ones by the spectrometer, an experimental peak consists of both scattered and unscattered components. Since scattered x-rays act as an additional source of radiation in the target, the average system efficiency for the yield geometry is given by:

$$\epsilon_{\text{avg}} = \epsilon_{\text{avg}}(c) + f\epsilon'_{\text{avg}}(c) + f^2\epsilon'_{\text{avg}}(c) + \dots \quad (21)$$

where: $\epsilon_{\text{avg}}(c)$ is the average system efficiency for the 3" x 3" yield geometry including the effect of Compton scattering in the helium mass absorption coefficient.

$\epsilon'_{\text{avg}}(c)$ is the average system efficiency for the 5-3/4" x 5-3/4" yield geometry including the effect of Compton scattering in the helium mass absorption coefficient.

A larger geometry is used for the scattered x-rays since they can be scattered anywhere in the target and still reach the detector. The effects of Compton scattering on the values of ϵ_{avg} as calculated with Eq. (16) were estimated as follows. Three quantities were calculated for each helium x-ray energy from Eq. (21). Each calculation was performed under different assumptions.

1. $\epsilon_{\text{avg}}(1)$ This quantity was calculated assuming a uniform stopping distribution of particles in the target and also assuming $\mu_c = f = 0$. This is a case in which Compton scattering is neglected.
2. $\epsilon_{\text{avg}}(2)$ This quantity was calculated assuming a uniform stopping distribution, $\mu_c = 0.189 \text{ cm}^2/\text{g}$ and $f = 0$. This is a case in which x-rays are lost because of Compton scattering (out-scattering) and in which no in-scattering occurs.
3. $\epsilon_{\text{avg}}(3)$ This quantity was calculated assuming a uniform stopping distribution, $\mu_c = 0.189 \text{ cm}^2/\text{g}$, and $f = 0.18$. This case corresponds to the physical case for a uniform stopping distribution in which both in- and out-scattering occur in the proper amounts.

The results showed that $\epsilon_{\text{avg}}(2)$ was less than $\epsilon_{\text{avg}}(1)$ by 17% and indicates that there occurred 17% out-scattering of the helium x-rays. The results also showed that $\epsilon_{\text{avg}}(3) = \epsilon_{\text{avg}}(1)$ to within 1%. Thus, although 17% of the x-rays was lost due to out-scattering, this loss was

compensated for by in-scattered x-rays of which 3% was doubly scattered. Therefore we neglected Compton scattering effects in calculation of ϵ_{avg} .

6) Discussion of Errors and Tabulation of ϵ_{avg}

The estimates on the errors of the mass absorption coefficients of helium and beryllium, discussed in Appendix A, were 15% and 5%, respectively. The coefficients were varied by these amounts in the Monte Carlo calculation in order to find the resultant uncertainties in ϵ_{avg} . The value of ϵ_{avg} was found to vary by less than 2% due to the uncertainty in the helium mass absorption coefficient and less than 2% due to that in the beryllium mass absorption coefficient. The error on ϵ_{avg} due to an estimated 5% error on the mass absorption coefficient of air was negligible.

An important source of error was the relative position of the detector to the center of the beam collimator, since this dimension essentially determined the solid angle of the system by defining the location of the beam in the target. The distance was $5'' \pm 0.2''$ and leads to a 10% uncertainty in the solid angle of the system as measured to the beam center.

The discussion in Sec. D4 led to an estimate of the error on ϵ_{avg} of 5% due to beam dispersion in the target. According to the discussion in Sec. C, the area of the detector was $56 \pm 2 \text{ mm}^2$, this causing a 4% uncertainty in ϵ_{avg} . The resultant values and errors on ϵ_{avg} are listed in Table VI.

E. The Numbers of X-Rays Observed

The numbers of x-rays in the $\pi\text{-K}_\alpha$ and $\mu\text{-K}_\alpha$ peaks were obtained from Eq. (12). The amplitude and FWHM of each peak was determined by a least

squares computer fit of the data to a function whose form was a single Gaussian with a linear background term. The π -K $_{\beta}$ and π -K $_{\gamma}$ peaks were fit simultaneously to a function whose form was a double Gaussian with a linear background term. The μ -K $_{\beta}$ and μ -K $_{\gamma}$ peaks had too few counts such that a double Gaussian fit to the peaks would not converge to yield reasonable values for the parameters. Therefore, a single Gaussian with linear background was assumed as the fitting function and the number of counts in both peaks was determined by subtracting from the total number of counts in the channel range of the peaks the number of background counts as determined by the computer fit.

A correction to the above values for the effects of Compton scattering was made as follows. According to the discussion of Sec. D5, a spectral peak consisted of approximately 17% in-scattered radiation of a mean energy slightly lower than the unscattered radiation. Therefore the experimental peaks were not strictly Gaussian in shape but exhibited an increased number of counts on their low-energy side. If only half these counts are included in the peak by the computer fit, an 8% enhancement in the amplitude of the peak is necessary in order to take into account the missing 8%. The resultant number of x-rays observed during the yield runs, as listed in Table VII, have therefore been increased by 8%. An 8% uncertainty due to this effect has also been combined with the statistical error on the amplitude of each of the peaks.

F. The Number of Stopping Particles

In order to obtain the number of pions or muons N_r which stopped in the target, a correction was applied to the number of 123456 scaler counts observed during each yield run. The number of scaler counts N_s was corrected by subtracting from it appropriate amounts for each of the following effects:

1. Background. The yield range curve (Fig. 9) was used in order to distinguish real particle stops from background. The background included stopping particles other than the ones of interest and particles not stopping in compartment 4 and yet not rejected by the anticoincidence logic of the beam telescope. The quantity subtracted is termed N_b and was exclusive of those particles which stopped in compartment 5.
2. Partition stops. Subtraction of a quantity N_p was made for the number of particles stopping in the partition between the compartments.
3. Stops in compartment 5. A number of the particles penetrated the partition and stopped in compartment 5 without being rejected by the anticoincidence logic. Of these, a smaller number of particles came to rest in that region of compartment 5 such that their x-rays had to pass through the partition in order to reach the detector (the so-called shadow region of Fig. 14). These should not count as legitimate stops since the resultant x-rays were considerably attenuated by the partition. This number N_5 was subtracted from N_s in order to account for this effect.

Thus N_r is given by the following expression:

$$N_r = N_s - N_b - N_p - N_5 . \quad (22)$$

2) Subtraction of Background from N_s

The background in the range curve (indicated by the dashed line in Fig. 9) was obtained by joining the right and left sides of the peaks

with a smooth curve.* The shape of the background was in part caused by the beam telescope anticoincidence efficiency. Since the anticoincidence efficiency was not perfect (see Appendix C), the level of background depended upon the number of incident particles. This dependence caused the left side of a peak in the range curve to exhibit a higher level of background than its right side. In addition to the background due to non-perfect anticoincidence efficiency, there was approximately 3% muon contamination in the pion peak in the range curve but no corresponding contamination of the muon peak by pions. There was also, probably, some contamination of both peaks with electrons. Since the beam was momentum-selected, it was assumed that the background under the pion peak contained no stopping pions and the background under the muon peak contained no stopping muons.

In order to determine $N_s - N_b$, it was assumed that for the same absorber thickness:

$$\frac{N_s - N_b}{N_s} = \frac{N_s' - N_b'}{N_s'} , \quad (23)$$

where: N_s' is the number of 123456's as recorded in the range curve.

N_b' is the background as determined from the same range curve.

During the yield runs pions were stopped with 6.13" of polyethylene absorber and muons with 10.5". The number of 123456 coincidences obtained

* The two open-circled points on the high-velocity side of the muon peak were obtained with an extrapolation which was based on the assumption that the muonic and pionic range curve peaks were of the same shape but of different amplitudes.

during the pion and muon yield runs, respectively, were:

$$\begin{aligned} N_{s,\pi} &= 116.3 \times 10^6 \\ N_{s,\mu} &= 26.3 \times 10^6 . \end{aligned} \tag{24}$$

The corresponding values of N_s' obtained from the range curve were:

$$\begin{aligned} N_{s,\pi}' &= 465 \times 10^3 \\ N_{s,\mu}' &= 59 \times 10^3 , \end{aligned} \tag{25}$$

and the values of the corresponding N_b' were:

$$\begin{aligned} N_{b,\pi}' &= (83 \pm 40) \times 10^3 \\ N_{b,\mu}' &= (37 \pm 2) \times 10^3 , \end{aligned} \tag{26}$$

where the errors on the above values of N_b' have been chosen to be equal to the differences in background levels between the right and left sides of the peaks in the range curve (see Fig. 9). Thus from Eqs. (23), (24), (25) and (26) we obtain:

$$\begin{aligned} N_{s,\pi} - N_{b,\pi} &= (95.4 \pm 10.4) \times 10^6 \\ N_{s,\mu} - N_{b,\mu} &= (9.73 \pm 0.88) \times 10^6 . \end{aligned} \tag{27}$$

3) Partition Stops

The weight of the helium in the 3" x 3" effective target region was 50.5g. The weight of a 3" x 3" portion of the partition was 0.884g with the bulk of this weight due to TiO_2 , the primary constituent of the pigment of the diffuse reflecting paint. An estimate was made of the fraction of particles which stopped in the partition from the ratio 0.0172 of the weight of the partition to the total weight of the helium in the 3" x 3" effective target region. N_p , as determined by multiplying $(N_s - N_b)$ by that ratio was:

$$N_{p,\pi} = (1.64 \pm .18) \times 10^5 \quad (28)$$

$$N_{p,\mu} = (0.167 \pm 0.015) \times 10^5.$$

In the calculation of N_p , $(N_s - N_b)$ was used rather than N_s alone, since it was felt that the source of the major portion of the background was the beam telescope anticoincidence efficiency rather than real stopping particles.

4) Loss of X-Rays from Compartment 5 and Determination of N_r

Pions or muons of momentum 200 MeV/c lose an energy of ≈ 2 MeV in traversing the 6.96 cm of helium in either target compartment.⁵² When a 200 MeV/c beam was incident on the target, the resulting pulses from the phototube viewing compartment 5 were distributed in height up to a maximum of $\approx 6V$ into 50Ω .

If we assume that all of the 200 MeV/c particles traversing compartment 5 give 3V pulses while losing 2 MeV of energy, then these particles

would trigger the 200 mV discriminator of counter 5 after losing 130 keV of energy. Since pions or muons having only 130 keV of energy travel $\sim 50\mu$ in liquid helium, with the 3V pulse assumption, only those particles in a stopping beam which travel $\lesssim 50\mu$ in compartment 5 would fail to be rejected as stops by the beam telescope logic. However, not all of the 200 MeV/c particles which traversed compartment 5 gave pulses as high as 3V. Therefore not all of the particles were rejected as stops before they penetrated appreciable distances into compartment 5.

A negligible number of x-rays from the shadow region were incident on the detector because of the high degree of attenuation of these x-rays by the partition. This attenuation was estimated by assuming that the absorption of x-rays by the 16 mg/cm^2 thick reflecting paint on the partition was characteristic of the titanium in the pigment of the paint.

The loss of x-rays from particles stopping in compartment 5 was estimated as follows. The volume of the shadow region was 52.2 cm^3 as determined from geometrical considerations and the 3" x 3" effective target volume was 404 cm^3 . If then, the shadow region contained the same density of stopping particles as the effective target region, as much as 11.4% of the helium x-rays would be lost due to their attenuation by the partition. Since some particles did stop in compartment 5, the density of stopping particles in the shadow region which did not trigger the anticoincidence circuit was assumed, for calculational purposes, to be half that in the effective target region and thus N_5 was determined from:

$$N_5 = 0.057 (N_s - N_b) . \quad (29)$$

From Eq. (29) we obtain therefore:

$$N_{5,\pi} = (5.43 \pm 5.43) \times 10^6$$

$$N_{5,\mu} = (0.56 \pm 0.56) \times 10^6 ,$$
(30)

where the uncertainty on N_5 was taken to be equal to N_5 itself. Since x-rays from particles which stopped in compartment 5 outside the shadow region without triggering the anticoincidence circuit could reach the detector almost as easily as if they had stopped in compartment 4, these stopping particles were neglected as a potential source of lost x-rays. Further, particles were assumed not to have stopped in the back wall of compartment 5 without triggering the anticoincidence circuit.

The respective number of pion and muon stops in the yield runs can be determined from Eqs. (22), (27), (28) and (30). We obtain:

$$N_{r,\pi} = (88.3 \pm 11) \times 10^6$$

$$N_{r,\mu} = (9.01 \pm 0.99) \times 10^6 .$$
(31)

H. Negligible Sources of Error

The following items were considered and subsequently dismissed as possible sources of error in the yield measurements.

1. The maximum stop rate observed during the (pion) yield run was $R(1234\bar{5}\bar{6}) = 27 \times 10^3/\text{sec}$ (corrected for the beam duty

factor of 2.5) and since the beam telescope resolving time was approximately 20 nsec, the probability that two particles would stop simultaneously in the target was considered negligible.

2. Possible loss of x-ray information because of improper time adjustment in the "fast-slow" coincidence circuit was considered negligible since improper timing would have been readily detectable with the visual timing aid (see Sec. IV C).
3. Although the yield data were accumulated using a 3" x 3" collimator in the beam, the range curve was taken with a 4" x 4" collimator. The determination of N_r was based largely upon the assumption, implicit in Eq. (23), that a range curve taken with a 3" x 3" collimator would have resulted in the same shape as the one taken with the 4" x 4" collimator. The validity of the assumption was indicated by the fact that the ratio of the $^{123456}\bar{56}$ rate at an absorber thickness of 6.13" to the rate at 10.5" of absorber for the range curve was the same (to within 7%) as the ratio of these rates for the yield runs.
4. The random coincidence rate was calculated to be less than 0.5% of the stop rate and hence the number of random stops was considered negligible.

G. Tabulation of Yields

The absolute pionic and muonic x-ray yields, as calculated with Eq. (6), are listed in Table VIII(a). Since the total number of counts in the muonic yield spectrum was too few to allow the computer fit program to resolve the $\mu\text{-K}_\beta$ and $\mu\text{-K}_\gamma$ peaks, resolution was achieved as

follows. The individual muonic x-ray spectra obtained during the cyclotron run were combined such that a double Gaussian fit to the $\mu\text{-K}_\beta$ and $\mu\text{-K}_\gamma$ peaks did converge. Their relative line intensities were thereby found to be:

$$R \equiv \frac{I_{\mu\text{-K}_\gamma}}{I_{\mu\text{-K}_\beta}} = 0.239 \pm 0.10 \quad (32)$$

If the number of $\mu\text{-K}_\beta$ and $\mu\text{-K}_\gamma$ x-rays which were observed during the yield run (Table VII) is multiplied by $(1 + R)^{-1}$, the total number of $\mu\text{-K}_\beta$ x-rays observed during the yield run is obtained.

Some relative yields are listed in Table VIII(b). Since the number of stops does not enter into the measurement of a relative yield, ΔN_r was set equal to zero when deriving relative yield quantities from Table VIII(a).

VIII. DISCUSSION OF RESULTS

A. Energies

1) Tabulation of Results

The measured values of the energies of the pionic and muonic x-rays in He⁴ are listed in Table IX. The values obtained from the July 1967 and November 1967 runs are listed in the second and third columns of the Table. The weighted averages of these values are listed in the "combined" column. The measured values of the energies from the July run as reported here differ slightly from the values as reported previously.³⁵ These differences, however, are nominal. They arise from the use in this work of (1) a more recent value of the Co⁵⁷ γ -ray calibration energy and (2) a more comprehensive data analysis.

Eartly²⁸ has recently measured the energies and yields of the helium x-rays. His results are given in Table X. Where comparison is possible, the measured energy values reported by Eartly are in agreement with the values reported in this work, the latter having greater precision.

2) Muonic X-Ray Energies

The experimental values of the μ -K _{α} and μ -K _{β} energies, listed in the "combined" column of Table IX, are in agreement with their calculated values [Table I(a)] to within experimental errors. This agreement indicates that proper techniques were used to determine the helium x-ray energies. However, the measured value of the μ -K _{γ} energy is 112 ± 70 eV higher in energy than its calculated value. A reasonable explanation

for this discrepancy is contamination of the $\mu\text{-K}_\gamma$ line with $\mu\text{-K}_\delta$ (10.54 keV) and perhaps higher-energy unresolved transitions.

3) Pionic X-Ray Energies and the Nuclear Force Shift

We obtain the experimental value for the nuclear force shift $\Delta E_{\text{nuc1}}(\text{exp})$ by subtracting the measured $\pi\text{-K}_\alpha$ transition energy, listed in the "combined" column of Table IX, from the electromagnetically calculated value listed in Table I(b). Thus:

$$\Delta E_{\text{nuc1}}(\text{exp}) = 80 \pm 50 \text{ eV.} \quad (1)$$

The experimental value for the nuclear force shift of the 1s state can also be obtained, in principle, from the measured value of either the $\pi\text{-K}_\beta$ or $\pi\text{-K}_\gamma$ transition energies. However, as in the case of the $\mu\text{-K}_\gamma$ line, the measured energy of the $\pi\text{-K}_\gamma$ transition is higher than its expected energy. This discrepancy is attributed to the presence of $\pi\text{-K}_\delta$ and perhaps higher-energy unresolved transitions in the $\pi\text{-K}_\gamma$ peak.

The $\pi\text{-K}_\beta$ transition was not used to determine a value for the nuclear force shift for the following reasons. In order to determine the center channel location of the $\pi\text{-K}_\beta$ peak, both the $\pi\text{-K}_\beta$ and $\pi\text{-K}_\gamma$ data were least squares fit simultaneously to a two-Gaussian function. This fitting procedure could have introduced an error in the center channel location of the $\pi\text{-K}_\beta$ peak since, as has been shown, the $\pi\text{-K}_\gamma$ peak contained higher order transitions and therefore was not Gaussian in shape.

The predicted values for the nuclear force shift, reproduced from Sec. II, are:

$$\begin{aligned}
 \Delta E_{\text{nucl}}(\text{Deser}) &= 41 \pm 14 \text{ eV} \\
 \Delta E_{\text{nucl}}(\text{Brueckner}) &= 99 \pm 14 \text{ eV} \\
 \Delta E_{\text{nucl}}(\text{Karplus}) &= 51 \pm 14 \text{ eV} \\
 \Delta E_{\text{nucl}}(\text{Wolfenstein}) &= 41 \pm 10 \text{ eV} \\
 \Delta E_{\text{nucl}}(\text{Ericson}) &= 111 \text{ eV} \\
 90 \text{ eV} &\leq \Delta E_{\text{nucl}}(\text{Boyd}) \leq 160 \text{ eV}
 \end{aligned}
 \tag{2}$$

All of the predicted values are seen to agree with the experimentally determined value for the nuclear force shift. At the present level of precision of measurement, therefore, all of the theories result in magnitudes and direction of the nuclear force shift which are consistent with its measured value.

B. Natural Linewidth

The experimental value of the natural linewidth of the $\pi\text{-K}_\alpha$ transition, or equivalently, the natural linewidth of the $1s$ level of the pionic He^4 atom, listed in Table V, is:

$$\Gamma_{\text{nat}}(\text{exp}) = 10 \begin{matrix} + 60 \\ - 10 \end{matrix} \text{ eV}
 \tag{3}$$

The $\pi\text{-K}_\beta$ and $\pi\text{-K}_\gamma$ data were not used to find $\Gamma_{\text{nat}}(\text{exp})$ for reasons

identical to those in Sec. A which were given for not using these data to find $\Delta E_{\text{nucl}}(\text{exp})$.

The predictions for the natural linewidth, reproduced from Sec. II, are:

$$\Gamma_{\text{nat}}(\text{Brueckner}) = 53 \text{ eV}$$

$$\Gamma_{\text{nat}}^{+}(\text{Eckstein}) = 400 \pm 240 \text{ eV}$$

$$\Gamma_{\text{nat}}^{-}(\text{Eckstein}) = 141 \pm 85 \text{ eV}$$

$$\Gamma_{\text{nat}}(\text{Ericson}) = 69 \text{ eV}$$

$$8 \text{ eV} \leq \Gamma_{\text{nat}}(\text{Boyd}) \leq 116 \text{ eV}$$

Comparing these to the experimental value of 10^{+60}_{-10} eV, we conclude that, at the present level of experimental precision, the values predicted for the natural linewidth of the 1s level in pionic He⁴ by the theories of Brueckner, Ericson and Boyd are consistent with the experimentally measured value. It should be noted that Γ_{nat}^{-} (Eckstein) which gives satisfactory agreement with experiment, is derived from coupling constants which have opposite signs and leads to disagreement between the Eckstein theory and the experimentally measured final state branching ratios of Shiff et.al.²⁰ If Γ_{nat}^{+} (Eckstein), derived from coupling constants of like sign, is used for comparison, then the predicted branching ratios are in agreement with the results of Shiff et.al., but the total 1s level width is much larger than the value measured in this experiment.

If the coupling constants should be of the same sign, then a possible explanation for the disagreement between theory and experiment is that Eckstein, in her calculation, neglects distortion of the pion wave function due to the strong interaction. She assumes a hydrogenic wave function for the pion. However, since the nuclear force is repulsive for the 1s state, the overlap of the pion with the nucleus would be less than that given by the hydrogenic wave functions and would result in a reduction in capture rates. Krell and Ericson¹⁰ have discussed this effect for the pionic O^{16} atom and have found a corresponding reduction by a factor of ≈ 2.5 in the density of 1s state pions at the center of the O^{16} nucleus when the strong interaction is considered.

C. Yields

The pionic and muonic x-ray yields are listed in Table VIII. It is noted that the total muonic K series yield is consistent with unity. The low total pionic K series is presumably because of capture of pions from high ns orbits.

These results, with the exception of the total pionic K series x-ray yield, are in satisfactory agreement with those of Eartly which are listed in Tables X(b) and X(c). The agreement between the total pionic yield is less satisfactory, being 0.095 ± 0.014 as determined in this experiment and 0.18 ± 0.05 as reported by Eartly.

Eartly has carried out a calculation of the cascade process of pions and muons in He^4 to which his yield data are fit. He finds that he is unable to reproduce the relative K_α /all K yields without the

inclusion of Stark mixing of angular momentum states in levels of high principal quantum number.

IX TABLES

TABLE

- I. (a) Calculated energies of muonic x-rays in He^4 .
 (b) Calculated energies of pionic x-rays in He^4 (electromagnetic effects only).
- II. Operating characteristics of liquid helium scintillation counter.
- III. (a) Spectral peaks fit with a one Gaussian plus linear background function (5 free parameters).
 (b) Spectral peaks fit with a two Gaussian plus linear background function (8 free parameters).
- IV. Lorentzian and Gaussian fractions.
- V. Results of the analysis of the natural linewidth of the $\pi\text{-K}_\alpha$ transition.
- VI. Detector efficiency and average system efficiency.
- VII. Numbers of x-rays observed during yield runs.
- VIII. (a) Absolute pionic and muonic x-ray yields from liquid He^4 .
 (b) Relative pionic and muonic x-ray yields from liquid He^4 .
- IX. Experimental values obtained for the He^4 pionic and muonic x-ray energies.
- X. (a) Eartly's experimental values obtained for He^4 pionic and muonic x-ray energies.
 (b) Eartly's absolute pionic and muonic x-ray yields in He^4 .
 (c) Eartly's relative pionic and muonic x-ray yields in He^4 .

Table I(a) - Calculated energies of muonic x-rays in He⁴.

<u>Transition</u>	<u>Dirac Energy</u>	<u>$-\Delta E_{fns}$</u>	<u>$-\Delta E_{vp}$</u>	<u>E_{calc}</u>
$\mu-K_{\alpha}$	8.209 keV	-0.002 keV	0.020 keV	8.227 keV
$\mu-K_{\beta}$	9.729 keV	-0.002 keV	0.020 keV	9.747 keV
$\mu-K_{\gamma}$	10.260 keV	-0.002 keV	0.020 keV	10.278 keV

Table I(b) - Calculated energies of pionic x-rays in He⁴
(electromagnetic effects only).

<u>Transition</u>	<u>K. G. energy</u>	<u>$-\Delta E_{fns}$</u>	<u>$-\Delta E_{vp}$</u>	<u>E_{calc}</u>
$\pi-K_{\alpha}$	10.752 keV	-0.005 keV	0.0334 keV	10.780 keV
$\pi-K_{\beta}$	12.742 keV	-0.005 keV	0.0334 keV	12.770 keV
$\pi-K_{\gamma}$	13.439 keV	-0.005 keV	0.0334 keV	13.467 keV

Table II - Operating characteristics of liquid helium
scintillation counter.

Nominal helium reservoir capacity	15 l
Liquid helium loss rate	0.75 l/hr
Liquid nitrogen loss rate	negligible
Amount of helium in beam path (4"x 4" cross section).	160 g
Vacuum attained during operation (at pumping station) . . .	3×10^{-7} Torr
Beryllium interposed between liquid helium and Si(Li)	70 mils
Aluminized Mylar interposed between liquid helium and Si(Li). . .	1 mil

Table III(a) - Spectral peaks fit with a one Gaussian plus linear background function (5 free parameters).

<u>Peak</u>	<u>Spectrum</u>	<u>χ^2 (avg)</u>	<u>No. channels (avg)</u>
π -K _{α}	pionic	28	31
μ -K _{α}	muonic	30	35
μ -K _{α}	pionic	28	30
14.389 keV	Co ⁵⁷	53	42

Table III(b) - Spectral peaks fit with a two Gaussian plus linear background function (8 free parameters).

<u>Peaks</u>	<u>Spectrum</u>	<u>χ^2 (avg)</u>	<u>No. Channels</u>
π -K _{β} and π -K _{γ}	pionic	49	52
μ -K _{β} and μ -K _{γ}	muonic	25	31
K x-rays	Co ⁵⁷	54	42

Table IV - Lorentzian and Gaussian fractions.^{a)}

<u>η</u>	<u>Lorentzian fraction</u>	<u>Gaussian fraction</u>	<u>η</u>	<u>Lorentzian fraction</u>	<u>Gaussian fraction</u>
0	1	0	1.4286	0.552	0.656
0.1000	0.993	0.083	1.5385	0.527	0.675
0.2000	0.972	0.162	1.6666	0.500	0.694
0.3000	0.941	0.235	1.8181	0.472	0.715
0.4000	0.904	0.301	2.0000	0.442	0.734
0.4444	0.886	0.327	2.2222	0.410	0.758
0.5000	0.863	0.359	2.5000	0.375	0.780
0.6666	0.794	0.441	2.8571	0.338	0.804
0.8000	0.742	0.494	3.3333	0.299	0.829
1.0000	0.672	0.559	4.0000	0.257	0.855
1.0526	0.655	0.574	5.0000	0.212	0.882
1.1111	0.637	0.589	6.6666	0.164	0.910
1.1765	0.618	0.605	10.0000	0.113	0.939
1.2500	0.597	0.622	∞	0	1
1.3333	0.575	0.639			

a) Reproduced from the table of Davies and Vaughan⁴⁹

Table V - Results of the analysis of the natural linewidth of the π - K_{α} transition,

<u>Run No.</u>	<u>$\Gamma_{\text{inst.}}$ a)</u>	<u>Γ_{v}</u>	<u>Γ_{nat}</u>
665-2	556±68 eV	593±27 eV	67±128 eV
678-2	650±96	645±40	-10±192
678-4	542±58	579±38	69±121
696-3	593±89	427±43	-276±134
450-2 b)	457±61	549±27	161±98
combined			10 + 60 c) - 10

a) The FWHM of the μ - K_{α} line in the pionic x-ray spectrum

b) These results obtained from July 1967 cyclotron run

c) Includes a 20 eV subtraction correction (see Section VI C)

Table VI - Detector efficiency and average system efficiency.

<u>Energy</u>	<u>ϵ_{det}</u>	<u>ϵ_{avg}</u>
8.2 keV	0.679±0.04	(1.19±0.15) x 10 ⁻⁴
9.7	0.780±0.03	(1.50±0.19) x 10 ⁻⁴
10.3	0.807±0.02	(1.59±0.20) x 10 ⁻⁴
10.7	0.826±0.02	(1.63±0.20) x 10 ⁻⁴
12.7	0.885±0.01	(1.77±0.22) x 10 ⁻⁴
13.5	0.900±0.01	(1.82±0.23) x 10 ⁻⁴

Table VII - Numbers of x-rays observed during yield runs.

<u>Transition(s)</u>	<u>Number</u>
$\pi\text{-K}_\alpha$ a)	400±67
$\pi\text{-K}_\beta$	715±100
$\pi\text{-K}_\gamma$	137±38
$\pi\text{-K}_\beta$ and $\pi\text{-K}_\gamma$	852±106
$\mu\text{-K}_\alpha$ b)	435±44
$\mu\text{-K}_\beta$ and $\mu\text{-K}_\gamma$	351±34

a) The pionic x-ray yield run was of 3 hours duration

b) The muonic x-ray yield run was 3-3/4 hours duration.

Table VIII(a) - Absolute pionic and muonic
x-ray yields from liquid He⁴.

<u>Transition(s)</u>	<u>Yield</u>
$\mu\text{-K}_\alpha$	0.596±0.110
$\mu\text{-K}_\beta$	0.268±0.054
$\mu\text{-K}_\gamma$	0.059±0.023
Total $\mu\text{-K}$	0.923±0.130
$\pi\text{-K}_\alpha$	0.0336±0.0080
$\pi\text{-K}_\beta$	0.0518±0.0110
$\pi\text{-K}_\gamma$	0.00946±0.00320
Total $\pi\text{-K}$	0.0949±0.0140

Table VIII(b) - Relative pionic and muonic
x-ray yields from liquid He⁴.

$$\begin{aligned}
 Y_{\mu\text{-K}_\alpha} / Y_{\text{all K}} &= 0.647 \pm 0.052 \\
 Y_{\mu\text{-K}_\alpha} / Y_{\mu\text{-K}_\beta} &= 2.23 \pm 0.53 \\
 Y_{\pi\text{-K}_\alpha} / Y_{\text{all K}} &= 0.354 \pm 0.060 \\
 Y_{\pi\text{-K}_\alpha} / Y_{\pi\text{-K}_\beta} &= 0.649 \pm 0.180
 \end{aligned}$$

Table IX - Experimental values obtained for the He^4
muonic and pionic x-ray energies.

<u>Transition</u>	<u>July 1967 run</u>	<u>Nov. 1967 run</u>	<u>Combined</u>
$\mu\text{-K}_\alpha$	8.19 ± 0.05 keV	8.20 ± 0.04 keV	8.20 ± 0.04 keV
$\mu\text{-K}_\beta$	9.72 ± 0.06 keV	9.74 ± 0.05 keV	9.73 ± 0.05 keV
$\mu\text{-K}_\gamma$ ^{a)}	10.37 ± 0.10 keV	10.39 ± 0.08 keV	10.39 ± 0.07 keV
$\pi\text{-K}_\alpha$	10.72 ± 0.06 keV	10.69 ± 0.05 keV	10.70 ± 0.05 keV
$\pi\text{-K}_\beta$	12.72 ± 0.07 keV	12.73 ± 0.06 keV	12.72 ± 0.06 keV
$\pi\text{-K}_\gamma$	13.51 ± 0.10 keV	13.55 ± 0.07 keV	13.54 ± 0.07 keV

a) Includes higher energy unresolved transitions (see Sec. VIII).

Table X(a) - Eartly's experimental values obtained for He⁴
pionic and muonic x-ray energies (see reference 28).

<u>Transition</u>	<u>Energy</u>
$\pi\text{-K}_{\alpha}$	10.80 ± 0.15 keV
$\pi\text{-K}_{\beta}$	12.85 ± 0.15 keV
$\mu\text{-K}_{\alpha}$	8.25 ± 0.15 keV

Table X(b) - Eartly's absolute pionic and muonic
x-ray yields from He⁴ (see reference 28).

<u>Transition(s)</u>	<u>Yield</u>
Total μ	0.79 ± 0.13
Total π	0.18 ± 0.05

Table X(c) - Eartly's relative pionic and muonic
x-ray yields from He⁴ (see reference 28).

$$Y_{\mu\text{-K}_{\alpha}} / Y_{\text{all K}} = 0.58 \pm 0.05$$

$$Y_{\pi\text{-K}_{\alpha}} / Y_{\text{all K}} = 0.40 \pm 0.05$$

X. ACKNOWLEDGEMENTS

The author wishes to acknowledge the following persons for their contributions and support:

Dr. John R. Kane, with whom the author worked in preparation for the experiment and in the taking of experimental data, for his guidance and aid during all phases of this research and during the preparation of the manuscript.

Dr. Morton Eckhause for his continued interest in this experiment, for valuable suggestions and discussions during the course of this research, and for his guidance in the preparation of the manuscript.

Dr. Robert T. Siegel, his advisor, for his continued interest in this experiment, helpful discussions and advice, and careful reading of the manuscript.

Mr. David C. Buckle for his aid and support both during the preparation for the experiment and in the taking of experimental data.

Dr. Robert E. Welsh for his assistance and helpful advice and careful reading of the manuscript.

Mr. Stanley Hummel and the William and Mary machine shop staff for construction of the scintillation counters and much of the cryogenic equipment used in this experiment.

Dr. Raymond W. Southworth and the staff at the William and Mary computer center for assistance rendered during computer analysis of the data.

Drs. Carl M. Andersen, David A. Jenkins and Richard L. Kiefer for reading the manuscript.

Dr. David K. Anderson for calling to the authors attention the results of Figureau and Ericson.

Miss Betty Orrick for aid rendered both during the taking of experimental data and in the initial phases of data analysis.

Mr. Charles Bailey Spence, Jr. for aid rendered during the taking of experimental data.

Drs. Robert J. Harris, Jr. and William B. Shuler for helpful advice and for loan of their Si(Li) spectrometer.

Miss Dianne Britton for typing the manuscript.

This work was supported in part by the National Aeronautics and Space Administration.

XI APPENDICES

A. Mass Absorption Coefficients

In this appendix, the methods used to determine the mass absorption coefficients of helium, beryllium, and silicon and also the results of a determination of the x-ray transmission of the beryllium window are described. All other mass absorption coefficients used but not mentioned here may be found in references (53-55).

1) Helium

Since experimental measurements of the mass absorption coefficient of helium were not available, a determination was made by extending a calculation of Wheeler⁵⁶ up to a photon energy of 15 keV. The calculation uses a six-parameter Hylleras wave function for the ground state of the helium atom. For the final state, it uses a hydrogenic wave function for a nucleus of charge $Z = 2$ for the bound electron and a hydrogenic wave function of $Z = 1$ for the free electron. Wheeler estimates his calculation to be accurate to better than 10%.

Extension of the calculation into energy ranges greater than 2 keV incident photon energy invalidates the dipole approximation used in the photo effect matrix element, but Bethe and Salpeter⁵⁷ have shown that the effect of using the approximation in calculations of the total photoelectric cross section introduces errors $\sim (v/c)^2$, where v is the velocity of the ejected electron. At 13.5 keV, the largest of the helium x-ray energies, this introduces errors of $\sim 6\%$. Accordingly, the error on the mass absorption coefficient of helium was taken to be 15%. The results of the calculation are presented graphically in Fig. 16.

Since the specifications, as supplied by Linde, of the liquid helium were an impurity concentration of less than 50 ppm and since care was taken to purge the target before filling, the impurity concentration in the target helium was assumed to be negligible.

2) Beryllium

Experimental data were available on the mass absorption coefficient of beryllium.⁵³ However, since beryllium has a low Z, the presence of impurities in the sample can greatly alter the mass absorption coefficient.

The mass absorption coefficient of the beryllium windows used in the experiment was determined using

$$\mu_{\text{Be}} = \sum_i \mu_i \omega_i, \quad (1)$$

where the μ_i are the mass absorption coefficients of the elements present in the beryllium window and ω_i their fractional weight concentrations. A chemical analysis supplied with the beryllium stock indicated the presence of iron and oxygen in amounts significant enough (0.14% iron and 1% oxygen) to increase the mass absorption coefficient by $\approx 40\%$.

The transmission of the 50 mil beryllium window was measured at three energies using the radioactive sources of Co⁵⁷ and Se⁷⁵. The results are shown in Fig. 17 together with its calculated transmission. The agreement between the experimental and calculated transmission was better than 5% in the 8-14 keV region of the helium x-rays.

3) Silicon

The McGinnies tables⁵⁵ give the mass absorption coefficients of silicon for energies between 10 and 100 keV and hence it was necessary to extrapolate the curve in order to determine the coefficient for energies between 6.4 and 10 keV. Bearden's⁵³ determination of the mass absorption coefficient of aluminum was used as a guide in choosing extrapolated points. The mass absorption coefficient of silicon was a factor of 1.2 ± 0.1 times that of aluminum for energies of 10 and 15 keV. Thus, in order to determine the mass absorption coefficient for silicon between 6.4 and 10 keV, Bearden's values for aluminum were multiplied by 1.2.

The results are presented graphically in Fig. 18. Since the precision of the Bearden measurements was $\sim 1\%$, an error of 10% was estimated for the silicon mass absorption coefficient due to extrapolation uncertainties.

B. Intensities of Radiations from the Calibrated Co^{57} Source

In this appendix, we determine the number of 14.4 keV γ -rays and the number of K series x-rays emitted per second by the calibrated Co^{57} source used to measure the detector efficiency. The source (IAEA, Vienna) activity on the day of the measurement was $(1.74 \pm 0.03) \times 10^5$ disintegrations per second.

The nucleus of Co^{57} de-excites by electron capture, resulting in the population of some excited levels of Fe^{57} . The number of 14.4 keV γ -rays emitted per Co^{57} nucleus disintegration has been determined to be 0.086 ± 0.004 by Sprouse and Hanna.⁵⁸ If the ratio of the number

of captures of $L + M + \dots$ electrons to the number of captures of K electrons is ϵ_{cap} , then the ratio of the number of K shell vacancies resulting from the capture process is $(1 + \epsilon_{\text{cap}})^{-1}$. Thus the number of K x-rays per Co^{57} disintegration which result as a direct consequence of the capture process is:

$$f_{\text{kx}}(\text{cap}) = \frac{\omega_{\text{k}}}{1 + \epsilon_{\text{cap}}} , \quad (2)$$

where ω_{k} is the K fluorescent yield of iron. Thomas et.al.⁵⁹ have measured $\epsilon_{\text{cap}} = 0.118 \pm 0.014$ using $\omega_{\text{k}} = 0.293 \pm 0.005$. Therefore, $f_{\text{kx}}(\text{cap}) = 0.262 \pm 0.006$.

Transitions between the states of Fe^{57} also result in the production of x-rays by internal conversion. If N_{γ} is the number of γ -rays of energy E emitted per Co^{57} disintegration, then the number of K x-rays accompanying the γ -rays is:

$$f_{\text{kx}}(E) = \alpha_{\text{k}}(E) N_{\gamma}(E) \omega_{\text{k}} , \quad (3)$$

where $\alpha_{\text{k}}(E)$ is the K conversion coefficient for the transition. From the Sprouse and Hanna values of N_{γ} and the Albridge and Hall⁶⁰ values of α_{k} for the major transitions, we determine the following:

$$f_{\text{kx}}(136 \text{ keV}) = 0.00399 \pm 0.0004$$

$$f_{\text{kx}}(122 \text{ keV}) = 0.00555 \pm 0.0004$$

$$f_{\text{kx}} (14.4 \text{ keV}) = 0.225 \pm 0.015 .$$

Combining these and f_{kx} (cap), we obtain the total number of iron K series x-rays emitted per Co^{57} disintegration:

$$\sum f_{\text{kx}} = 0.497 \pm 0.016 .$$

Thus the number of 14.4 keV γ -rays emitted per second by the calibrated Co^{57} source was $15,000 \pm 700$ and the number of K x-rays per second was $86,500 \pm 3000$.

C. Anticoincidence Efficiency of Beam Telescope During Yield Runs

If an incident particle, registering a 1234 logical sequence, exited compartment 4 without triggering either counter 5 or counter 6, a 1234 $\bar{5}\bar{6}$ coincidence was generated and the particle labeled erroneously as a stop. This conclusion was also valid, of course, for a particle which did trigger counter 5 or 6 but, due to the finite time resolution of the circuits, these triggers were electronically out of coincidence with the 1234 signal. The beam telescope anticoincidence efficiency is given by the ratio of the number of true stops to the total number of stops.

In order to investigate the anticoincidence efficiency, the rates of various logical sequences were measured using the yield geometry but with the absorber removed from the beam. These signal rates, each corrected for a beam duty factor of 2.5, were:

$$\begin{aligned}
 R(12) &= 1.2 \times 10^6 / \text{sec} \\
 R(4) &= 570 \times 10^3 / \text{sec} \\
 R(5) &= 680 \times 10^3 / \text{sec} \\
 R(6) &= 680 \times 10^3 / \text{sec} \\
 R(1234) &= 170 \times 10^3 / \text{sec} \\
 R(12346\bar{5}) &= 13 \times 10^3 / \text{sec} .
 \end{aligned}$$

Using a resolving time of $\tau = 20$ nsec (the anticoincidence pulse width was 15 nsec and the width of the coincidence pulses was 5 nsec), we find the $12346\bar{5}$ random coincidence rate to be $R(6)R(1234)\tau = 2.3 \times 10^3 / \text{sec}$, much less than the $13 \times 10^3 / \text{sec}$ rate which was observed. The $12346\bar{5}$ logical signal could have been formed in two ways, either of which indicates an anticoincidence efficiency of less than unity: (1) A particle incident on the target, after exiting from compartment 4, bypassed compartment 5 subsequently scattering from the surrounding material of the cryostat into counter 6. (2) An incident particle, having passed through compartment 5, generated an anticoincidence pulse which was slightly out of time with the 1234 signal. Since $R(5) > R(4)$, it was probable that particles which triggered compartment 4 also triggered compartment 5. Therefore, it was assumed that the second effect was primarily responsible for the large $12346\bar{5}$ rate.

XII LIST OF REFERENCES

1. M. Conversi, E. Pancini and O. Piccioni, Phys. Rev. 71, 209 (1947).
2. E. Fermi and E. Teller, Phys. Rev. 72, 399 (1947).
3. J. A. Wheeler, Phys. Rev. 71, 320 (1947).
4. H. K. Ticho, Phys. Rev. 74, 1337 (1948).
5. M. Camac, A. D. McGuire, J. B. Platt and H. S. Schulte, Phys. Rev. 88, 134 (1952).
6. D. West, Repts. Prog. Phys. 21, 271 (1958). A comprehensive review of mesonic atoms is given here.
7. L. N. Cooper and E. M. Henley, Phys. Rev. 92, 801 (1953).
8. R. Hofstadter, Rev. Mod. Phys. 28, 214 (1956).
9. A. B. Mickelwait and H. C. Corben, Phys. Rev. 96, 1145 (1954).
10. M. Krell and T. E. O. Ericson, CERN Report TH.1018, (1969).
11. S. Deser, M. L. Goldberger, K. Baumann and W. Thirring, Phys. Rev. 96, 774 (1954).
12. V. K. Samaranyake and W. S. Woolcock, Phys. Rev. Letters 15, 936 (1965).
13. K. A. Brueckner, Phys. Rev. 98, 769 (1955).
14. K. A. Brueckner, R. Serber and K. M. Watson, Phys. Rev. 84, 258 (1951).
15. R. Karplus and S. Halpern, Bull. Am. Phys. Soc. 2, 5 (1957).
16. L. Wolfenstein, Bull. Am. Phys. Soc. 2, 39 (1957).
17. M. Ericson and T. E. O. Ericson, Ann. Phys. 36, 323 (1966).
18. S. G. Eckstein, Phys. Rev. 129, 413 (1962).
19. A. Figureau and M. Ericson, Nucl. Phys. B10, 349 (1969).
20. M. Shiff, R. H. Hildebrand and C. Giese, Phys. Rev. 122, 265 (1961).

21. M. Krell and T. E. O. Ericson, *J. Comput. Phys.* 3, 202 (1968).
22. M. Krell, Private communication.
23. T. L. Trueman, *Nucl. Phys.* 26, 57 (1961).
24. J. H. Boyd and V. R. Veirs, *Bull. Am. Phys. Soc.* 14, 525 (1969).
25. T. B. Day, *Nuovo Cimento* 18, 3605 (1960).
26. D. N. Michael, *Phys. Rev.* 158, 1343 (1967).
27. M. Leon and H. A. Bethe, *Phys. Rev.* 127, 636 (1962).
28. D. P. Eartly, thesis, University of Chicago (1969).
29. E. H. Thorndike and W. J. Shaler, *Rev. Sci. Instr.* 30, 838 (1959).
30. H. Fleishman, H. Einbinder and C. S. Wu, *Rev. Sci. Instr.* 30, 1130 (1959).
31. J. E. Simmons and R. B. Perkins, *Rev. Sci. Instr.* 32, 1173 (1961).
32. J. R. Kane and R. T. Siegel, *Bull. Am. Phys. Soc.* 10, 515 (1965).
33. J. R. Kane, R. T. Siegel and A. Suzuki, *Rev. Sci. Instr.* 34, 817 (1963).
34. R. V. Colvin, Sigurds Araj's and D. S. Miller, *Rev. Sci. Instr.* 33, 122 (1962).
35. R. J. Wetmore, D. C. Buckle, J. R. Kane and R. T. Siegel, *Phys. Rev. Letters* 19, 1003 (1967).
36. R. J. Harris, Jr. and W. B. Shuler, *Nucl. Instr. and Meth.* 51, 341 (1967).
37. R. J. Harris, Jr., thesis, College of William and Mary (1968).
38. C. H. Nowlin and J. L. Blankenship, *Rev. Sci. Instr.* 36, 1830 (1965).
39. W. Mehlhorn and R. G. Albridge, *Z. Physik* 175, 506 (1963) as referenced in C. M. Lederer, J. M. Hollander and I. Perlman, Table of Isotopes, J. Wiley and Sons, Inc. New York (1967).

40. J. A. Bearden, Rev. Mod. Phys. 39, 78 (1967).
41. A. H. Wapstra, A. J. Nijgi and R. Van Lieshout, Nuclear Spectroscopy Tables, Amsterdam, North Holland (1959) p. 81.
42. A. Worthing and J. Geffner, Treatment of Experimental Data, J. Wiley and Sons Inc. New York (1943).
43. H. R. Zulliger and D. W. Aitken, IEEE Trans. Nucl. Sci., NS-14, 563 (1967).
44. R. J. Harris, Jr., W. B. Shuler, M. Eckhause, R. T. Siegel and R. E. Welsh, Phys. Rev. Letters 20, 505 (1968).
45. W. W. Sapp, private communication.
46. J. E. Freund, Mathematical Statistics, Prentice-Hall, Inc. Englewood Cliffs, N. J. (1962).
47. G. R. Burbidge and A. H. de Borde, Phys. Rev. 89, 189 (1953).
48. U. Fano, Phys. Rev. 72, 26 (1947).
49. J. Tudor Davies and J. M. Vaughan, Astrophys. J. 137, 1302 (1963).
50. R. S. Frankel, president, Kevex Corporation (private communication).
51. C. M. Davison and R. D. Evans, Rev. Mod. Phys. 24, 79 (1952).
52. SREL 600 Mev Cyclotron Handbook (unpublished).
53. A. J. Bearden, J. Appl. Phys. 37, 1681 (1966).
54. G. W. Grodstein, U. S. Nat. Bur. Stand. Supplement to Circular 583 (1957).
55. R. T. McGinnies, U. S. Nat. Bur. Stand. Supplement to Circular 583 (1959).
56. J. A. Wheeler, Phys. Rev. 43, 258 (1933).
57. H. A. Bethe and E. E. Salpeter, Quantum Mechanics of One- and Two- Electron Atoms, p. 311, Academic Press Inc. New York (1957).

58. G. D. Sprouse and S. S. Hanna, Nucl. Phys. 74, 177 (1965).
59. H. C. Thomas, C. F. Griffin, W. E. Phillips and E. C. Davis, Jr., Nucl. Phys. 44, 268 (1964).
60. R. G. Albridge and D. C. Hall, Bull. Am. Phys. Soc. 10, 244 (1965).

XIII. FIGURES

Figures

1. Liquid helium target assembly.
2. Liquid helium target liner.
3. Thermal radiation shield for liquid helium target.
- 4(a). Liquid helium scintillation counter assembled (upstream view).
- 4(b). Liquid helium scintillation counter assembled (top view).
5. Schematic diagram of preamplifier input stage.
6. Plan view of experimental arrangement.
7. Block diagram of energy run logic.
- 8(a). Display from visual timing aid (unrouted).
- 8(b). Display from visual timing aid (routed).
9. Range curve.
10. He^4 pionic x-ray spectrum.
11. He^4 muonic x-ray spectrum.
12. Co^{57} calibration spectrum.
13. Graph of instrumental linewidth vs. energy.
- 14(a). Schematic diagram of experimental arrangement used for yields (top view).
- 14(b). Schematic diagram of experimental arrangement used for yields (downstream view).
15. Distribution of stopping particles in liquid helium target.
16. Graph of mass absorption coefficient of He^4 in the 3-15 keV region.

17. Transmission of x-rays through 50 mil beryllium window.
18. Graphs of mass absorption coefficients of aluminum and silicon.

HELIUM TARGET

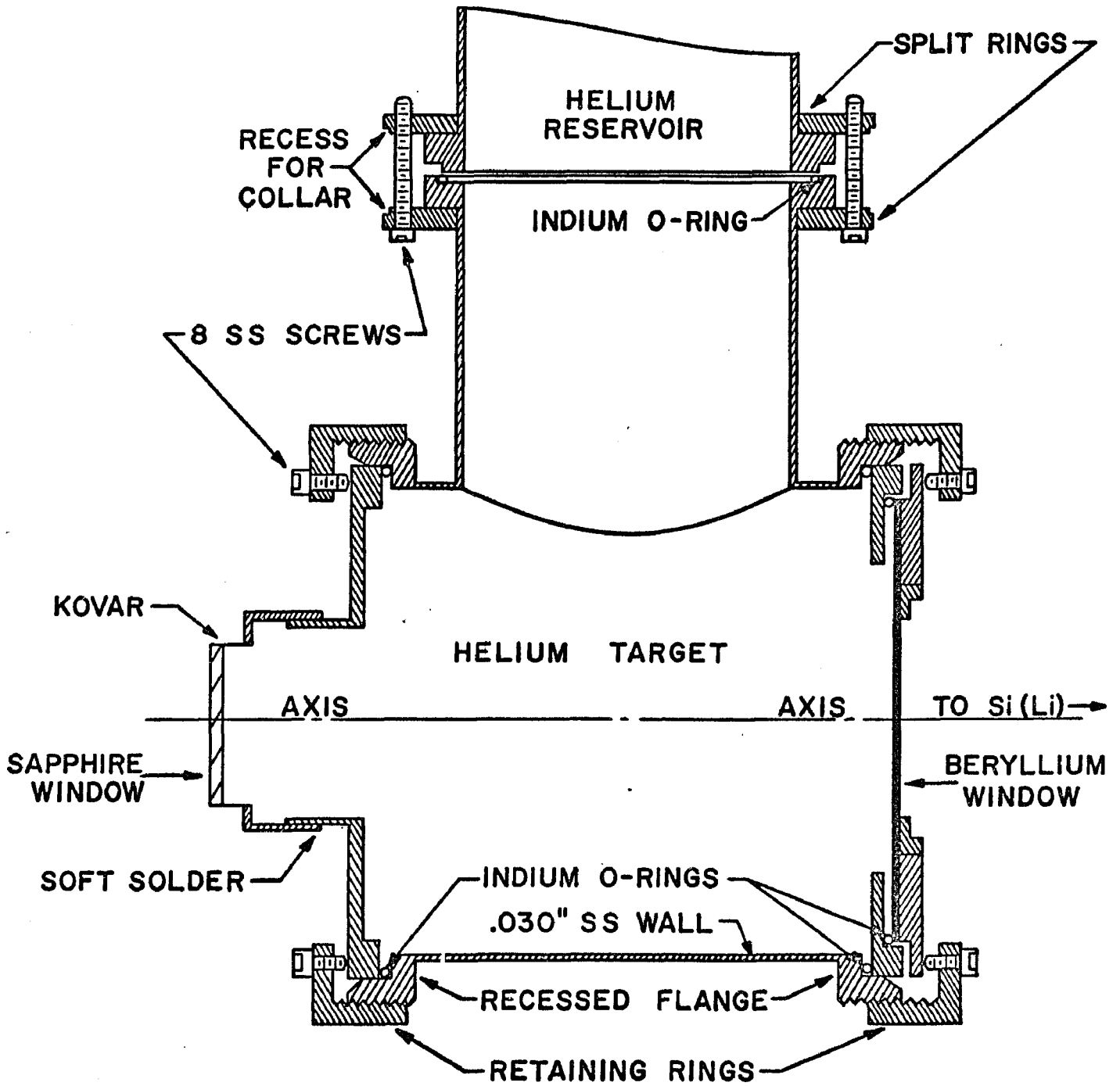


FIG. 1

LINER

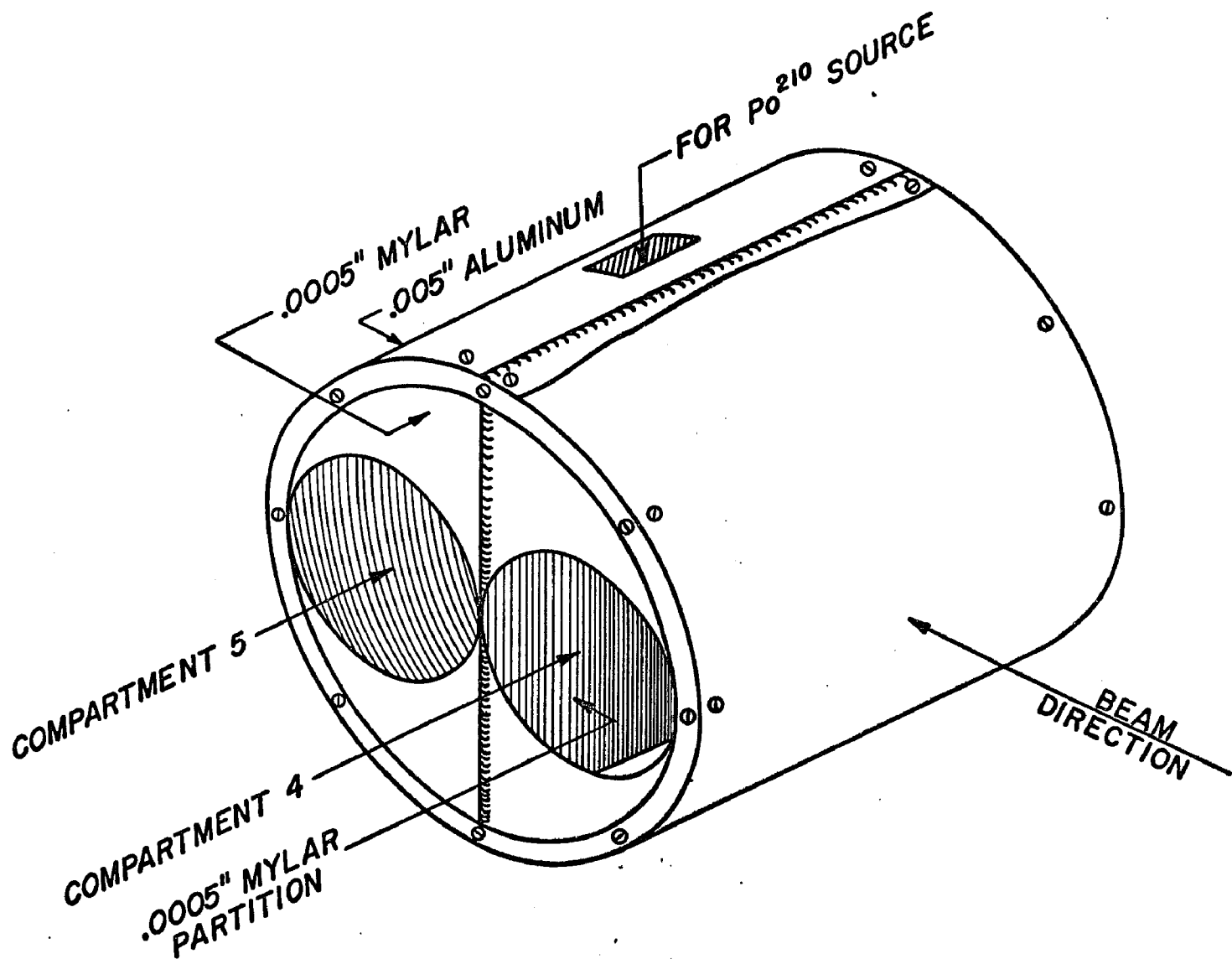


FIG. 2

RADIATION SHIELD

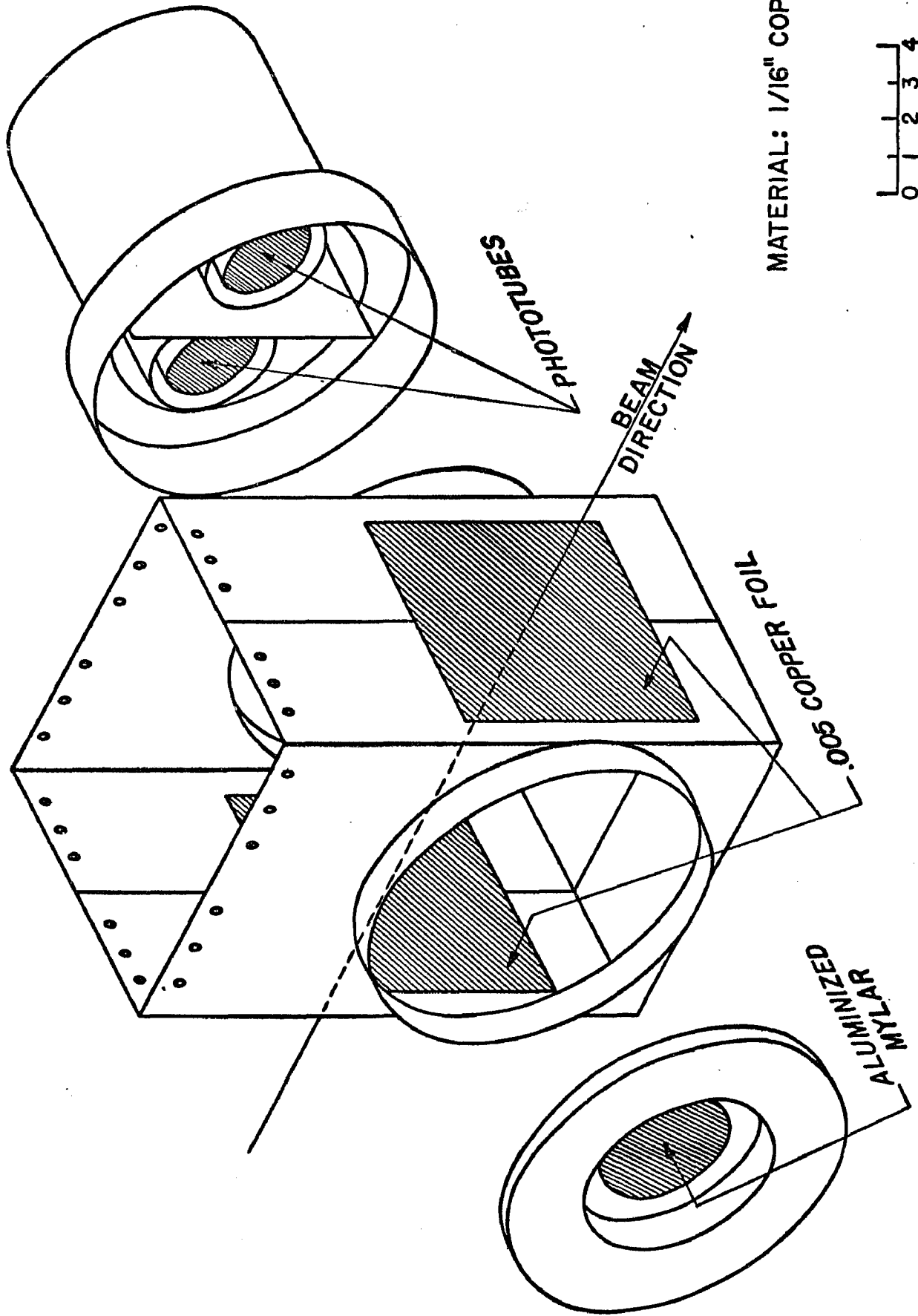


FIG. 3

COUNTER ASSEMBLY

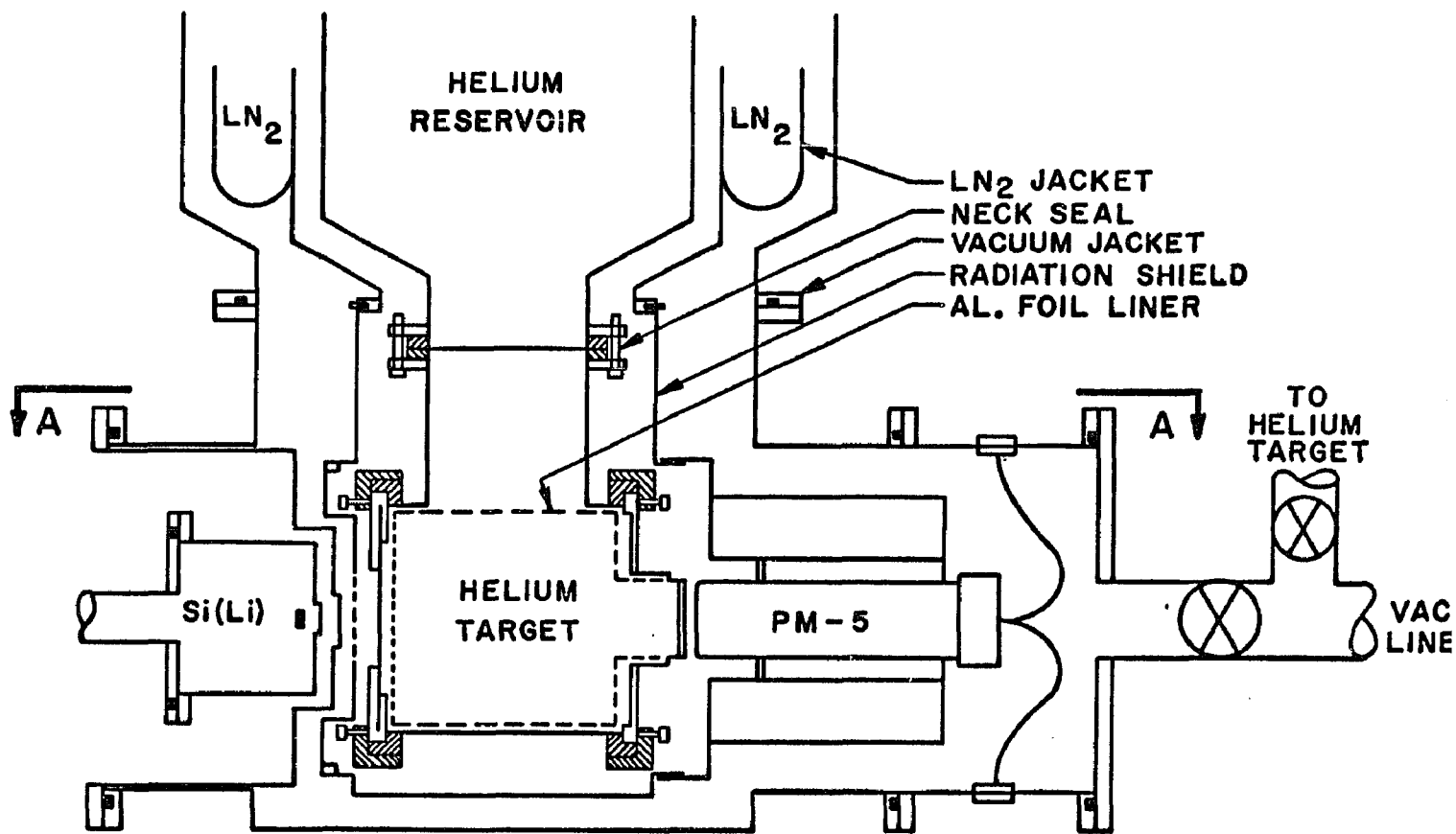
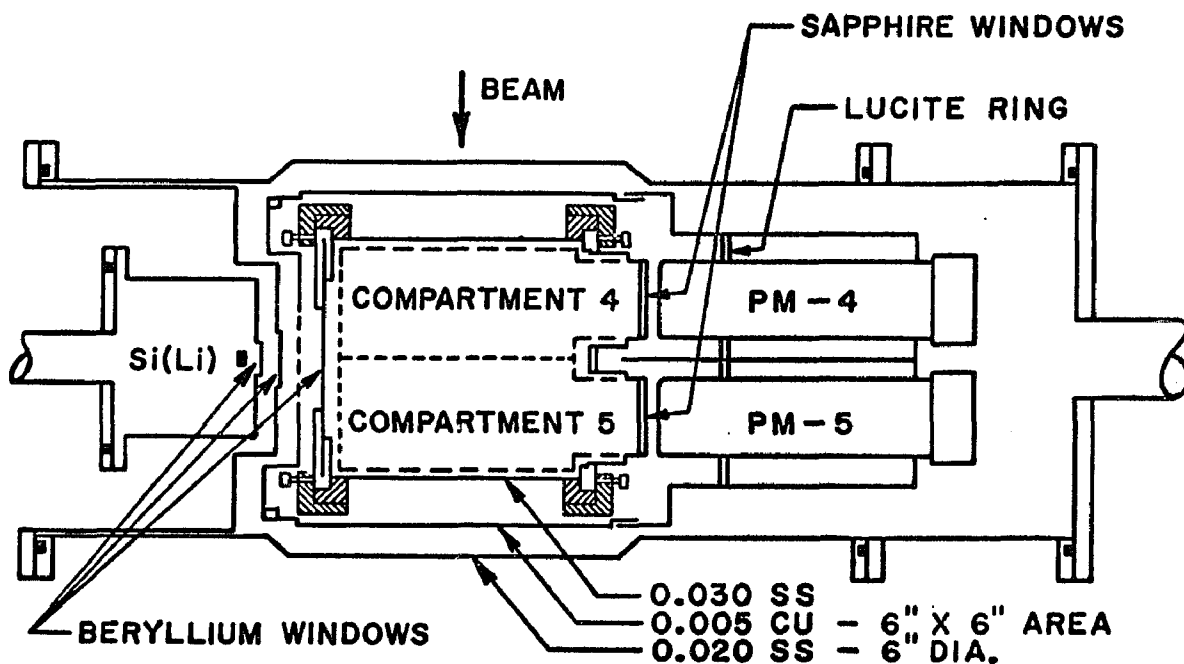


FIG. 4(a)



SECTION A-A



FIG. 4(b)

PREAMPLIFIER INPUT STAGE

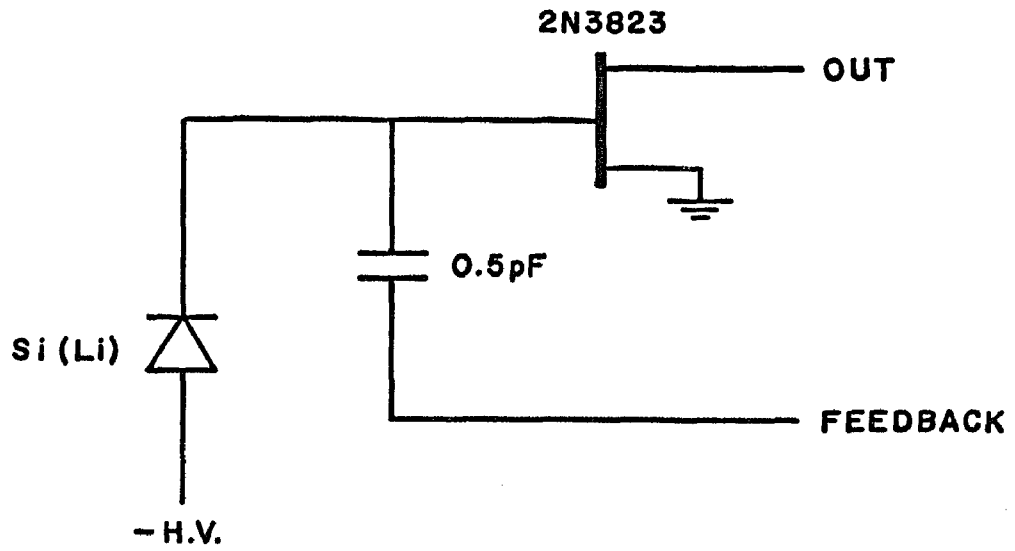
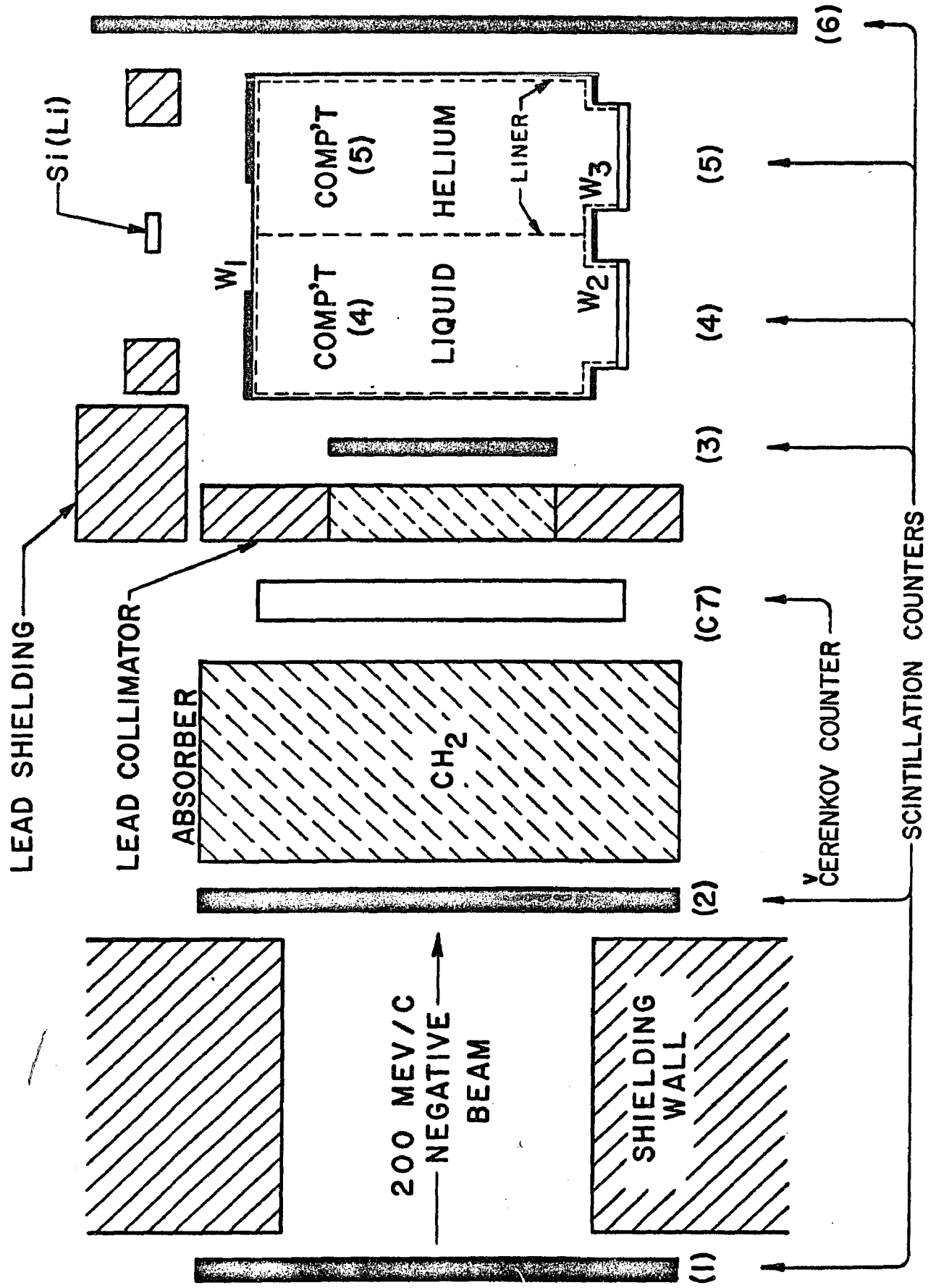
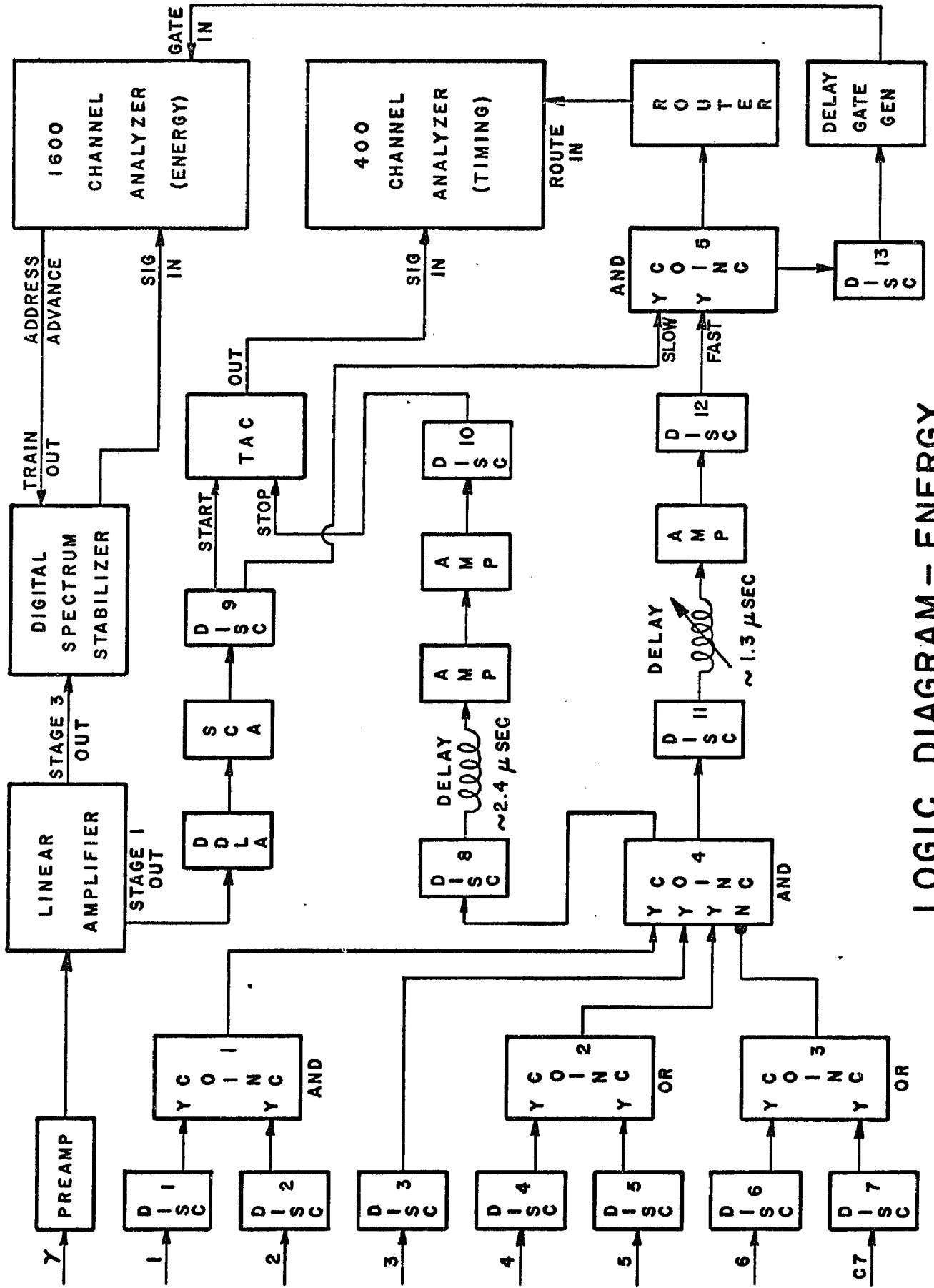


FIG. 5

EXPERIMENTAL ARRANGEMENT





LOGIC DIAGRAM - ENERGY

TIMING SPECTRUM

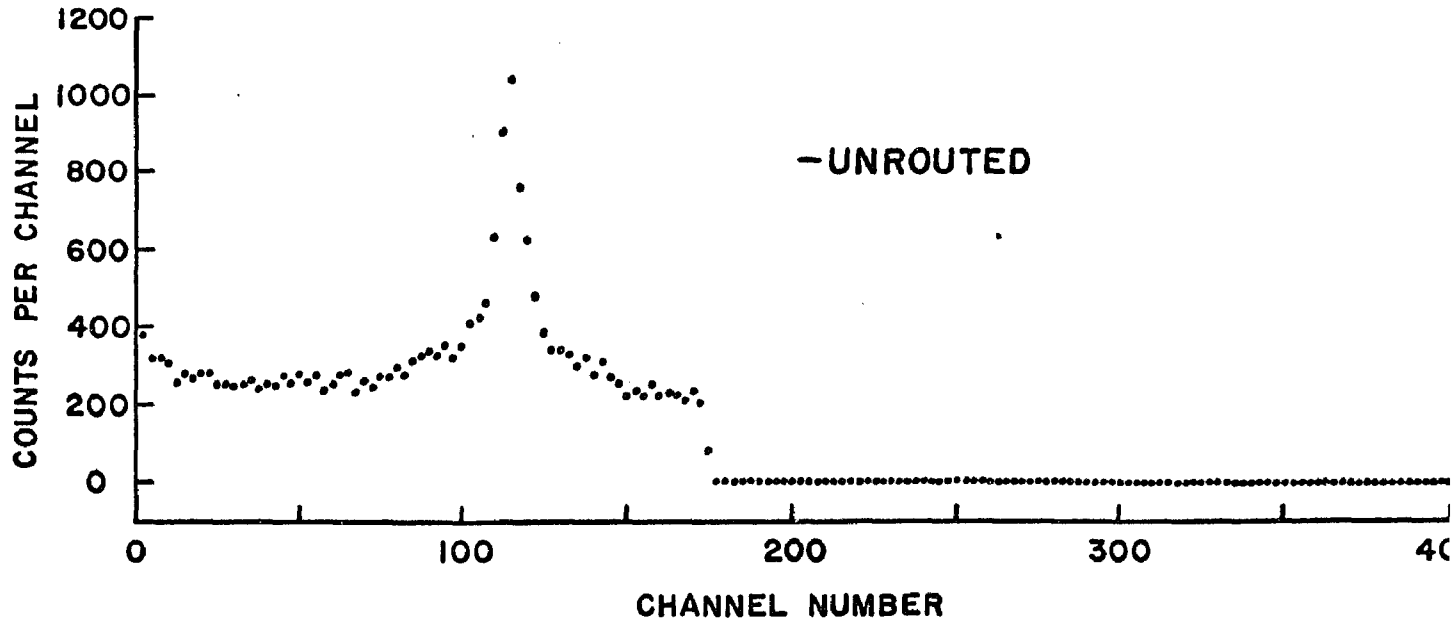


FIG. 8(a)

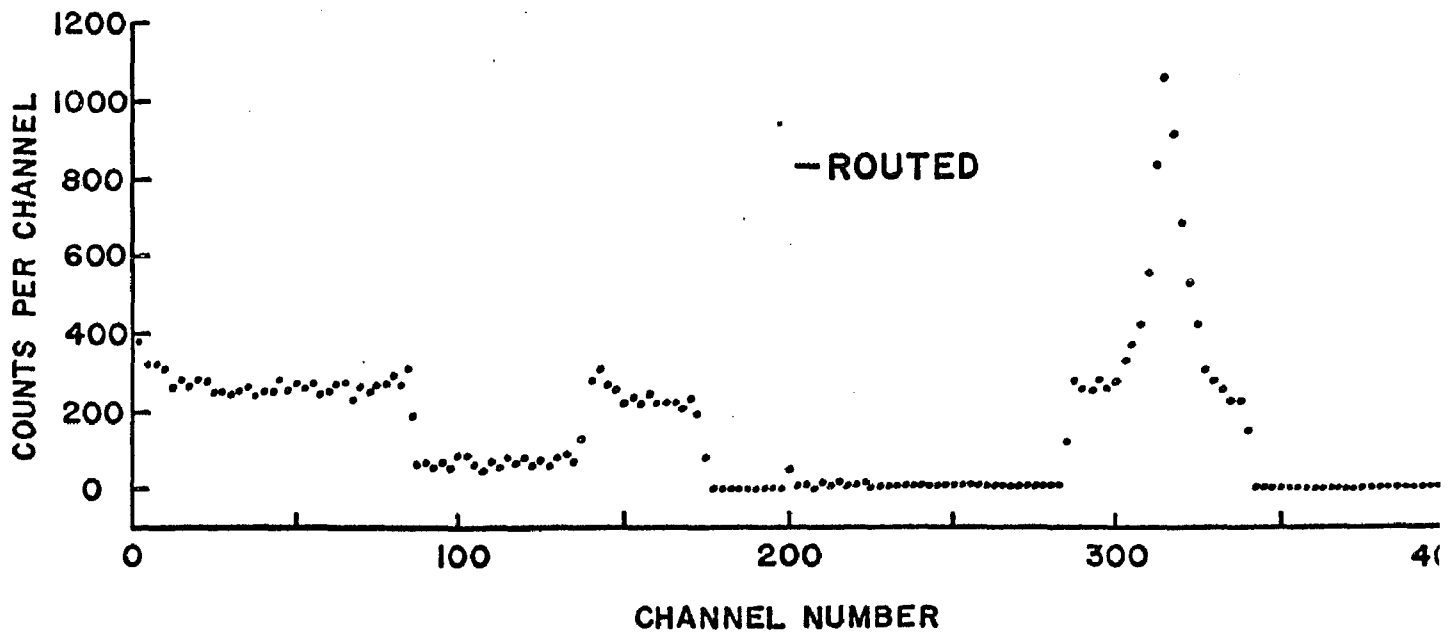


FIG. 8(b)

RANGE CURVE

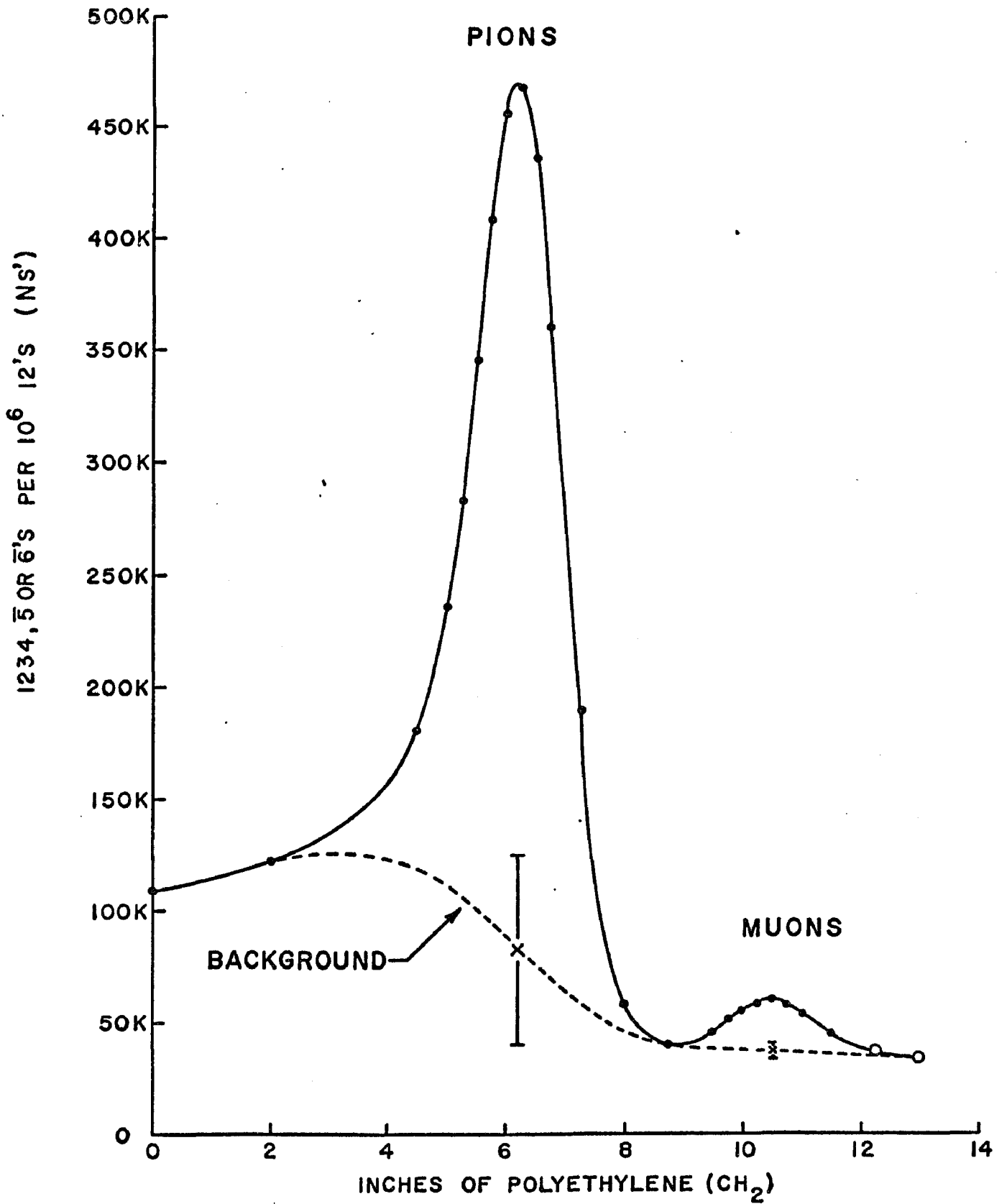


FIG. 9

PIONIC X-RAYS IN HELIUM

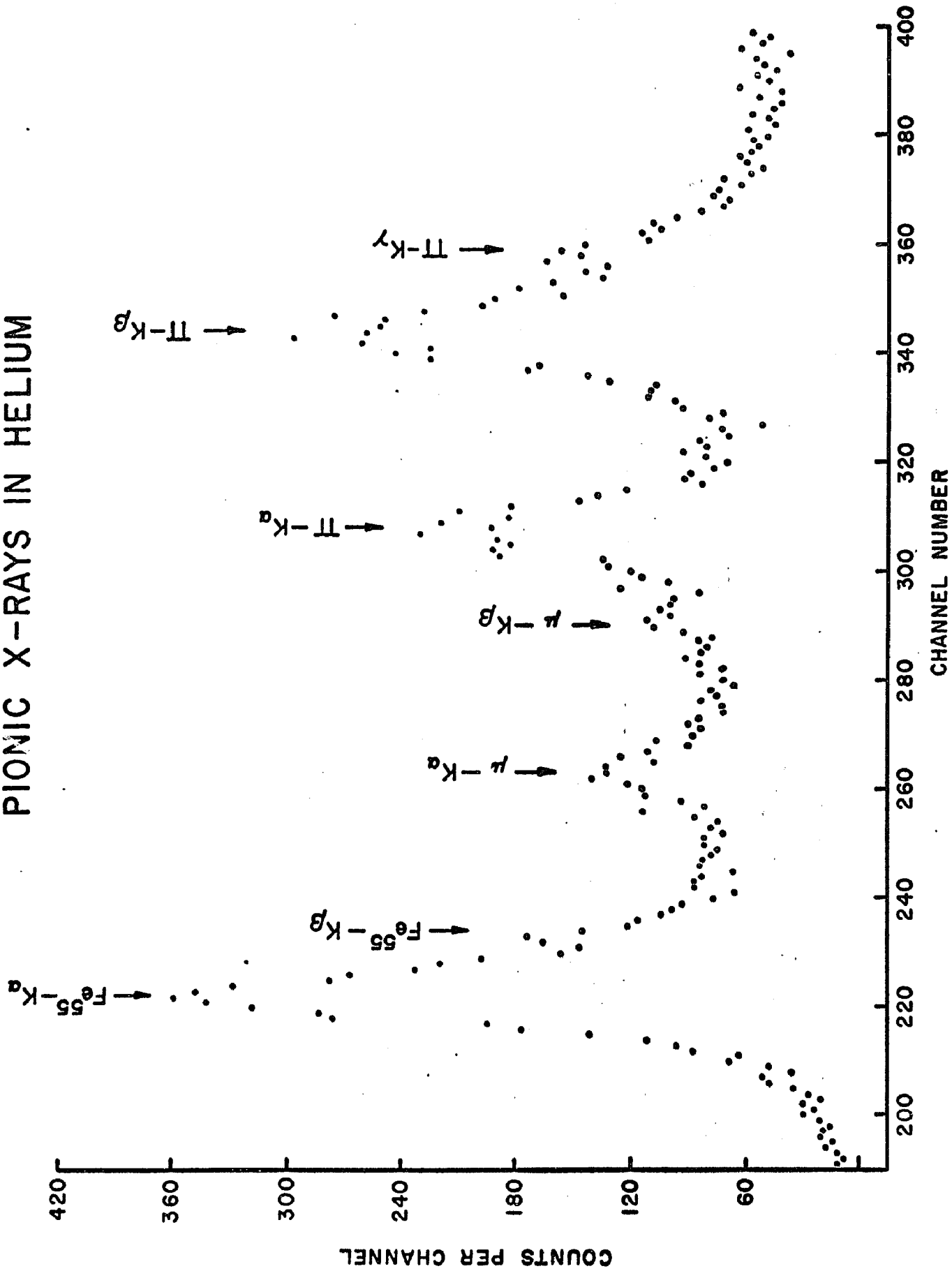


FIG. 10

MUONIC X-RAYS IN HELIUM

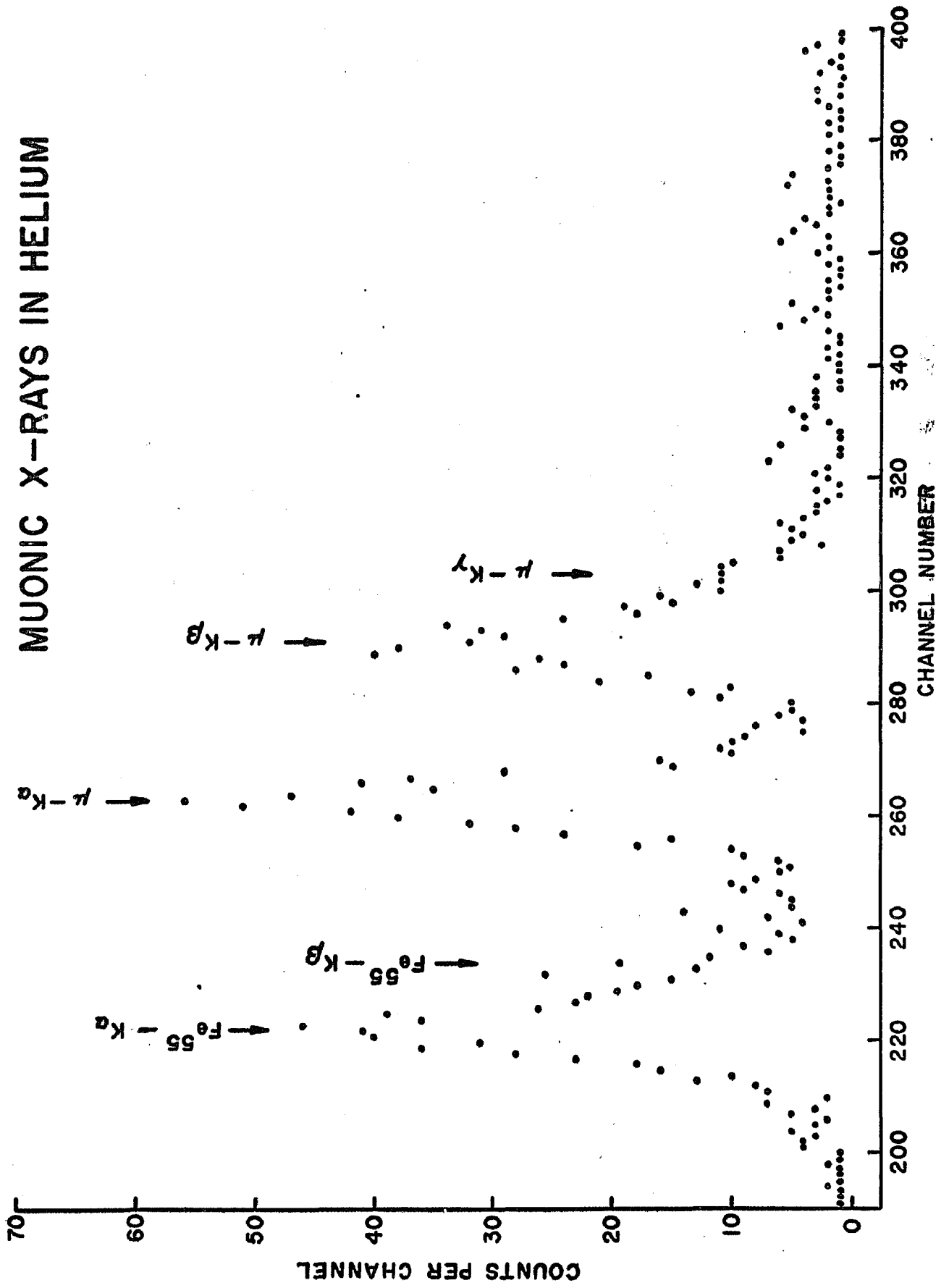


FIG 11

Co^{57} SPECTRUM

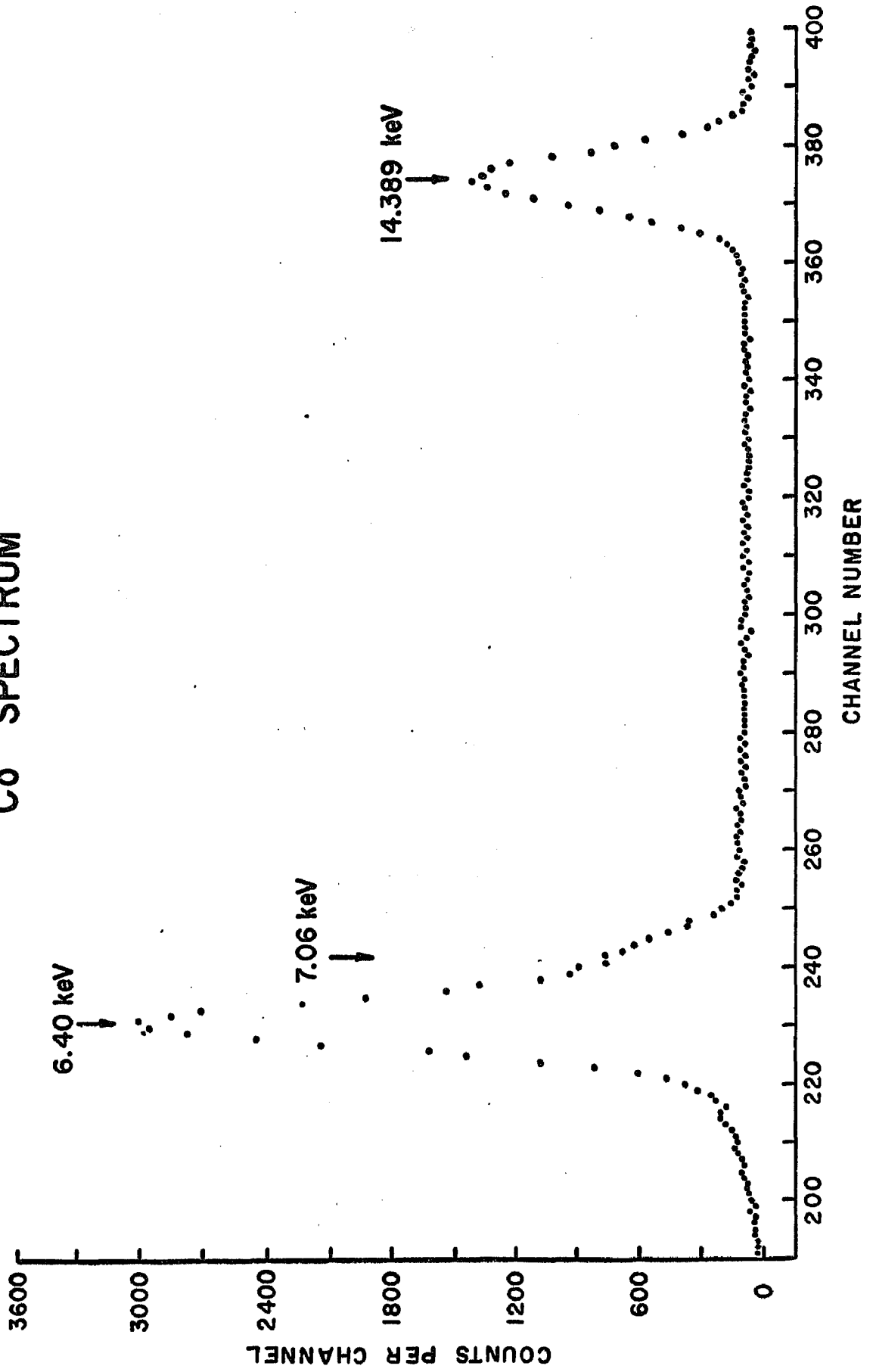


FIG. 12

SYSTEM RESOLUTION VS ENERGY

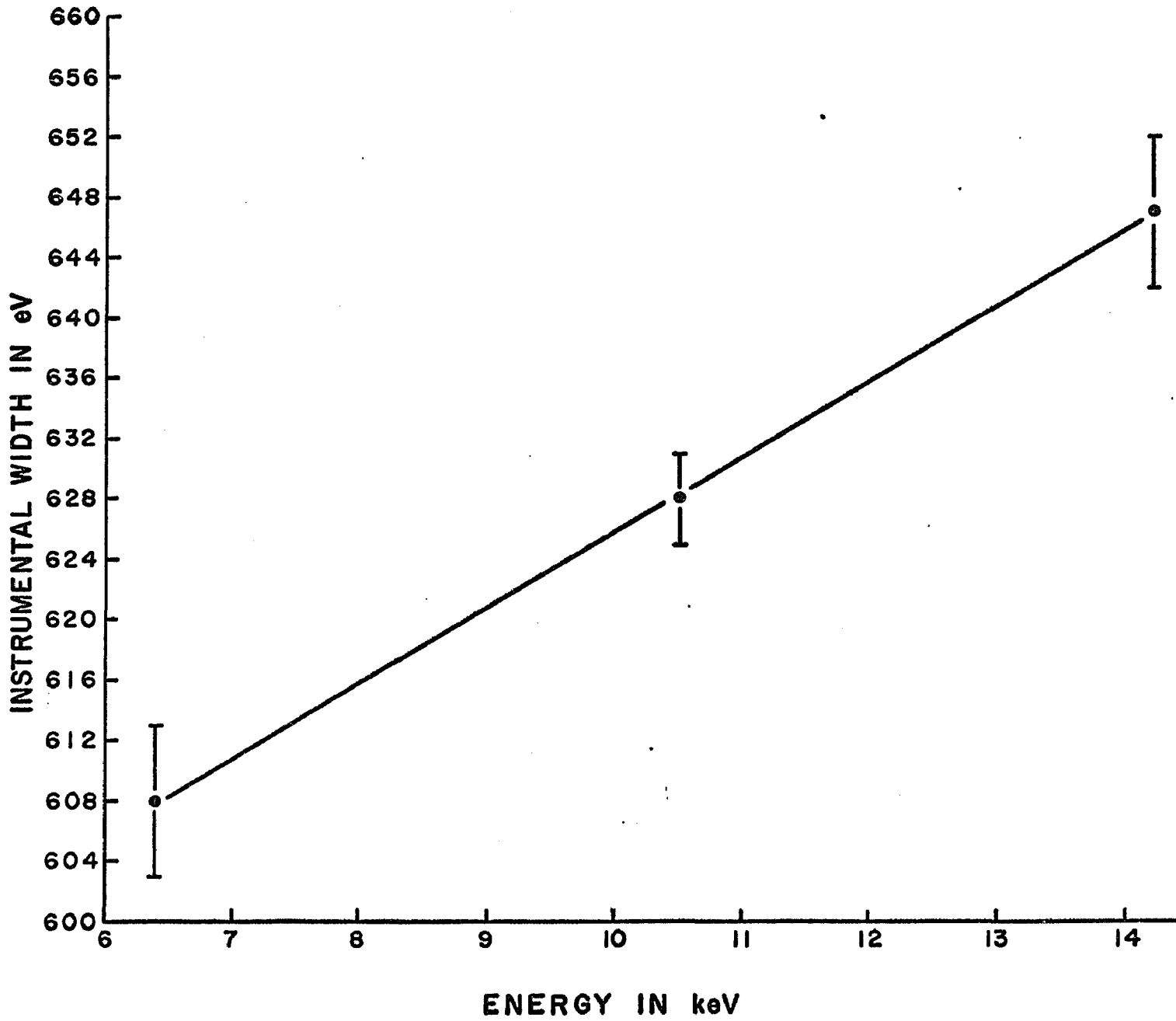


FIG. 13

EXPERIMENTAL ARRANGEMENT - YIELDS

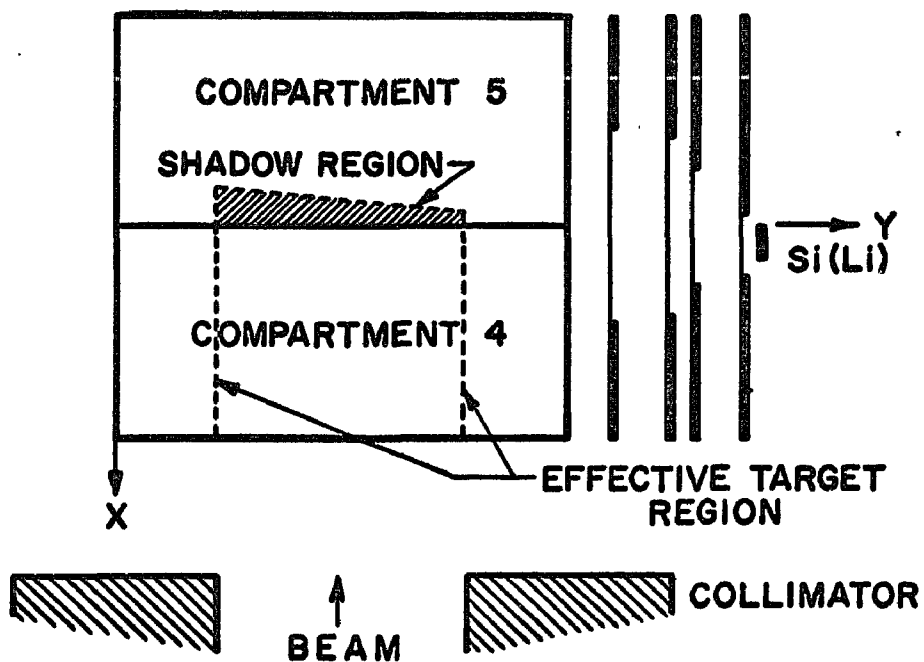


FIG. 14(a)

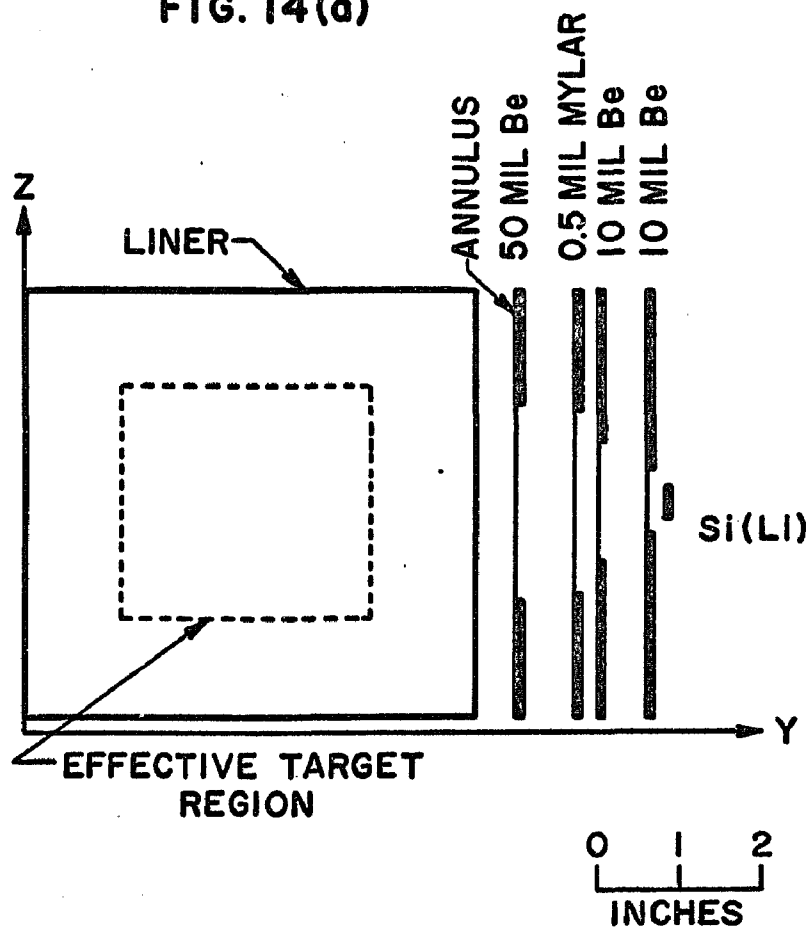


FIG. 14(b)

STOPPING DISTRIBUTIONS

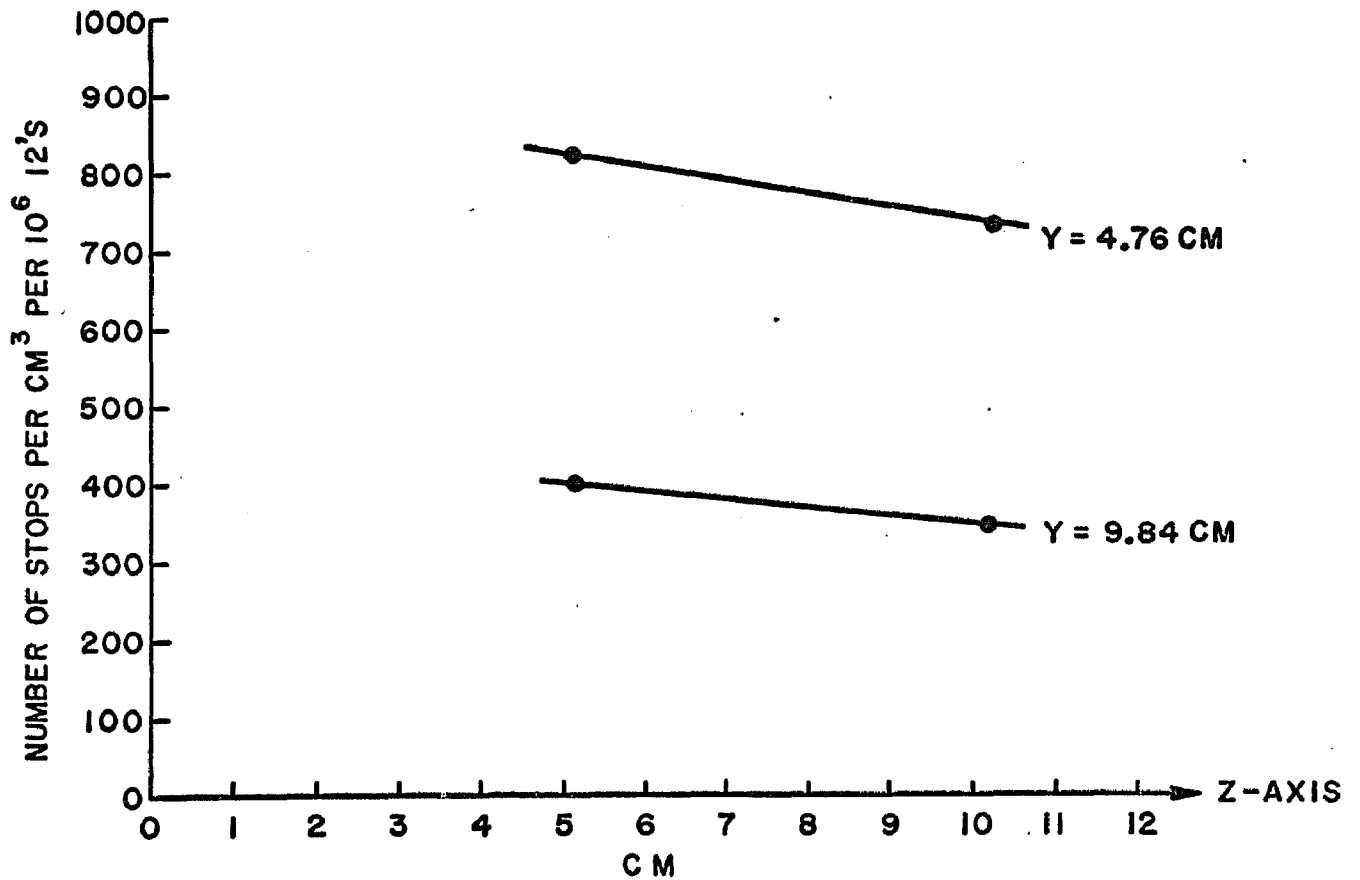
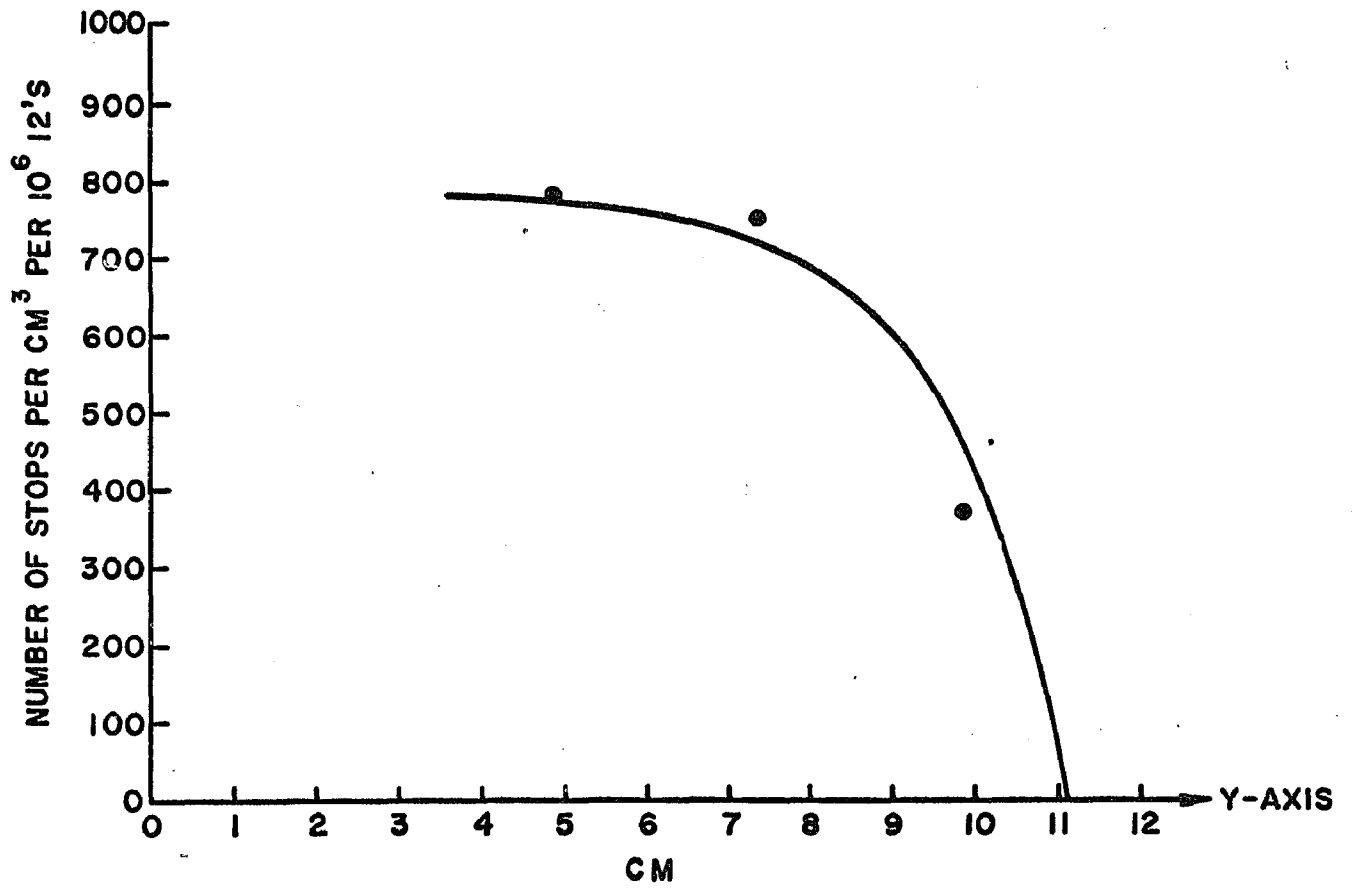


FIG. 15

MASS ABSORPTION COEFFICIENT OF HELIUM

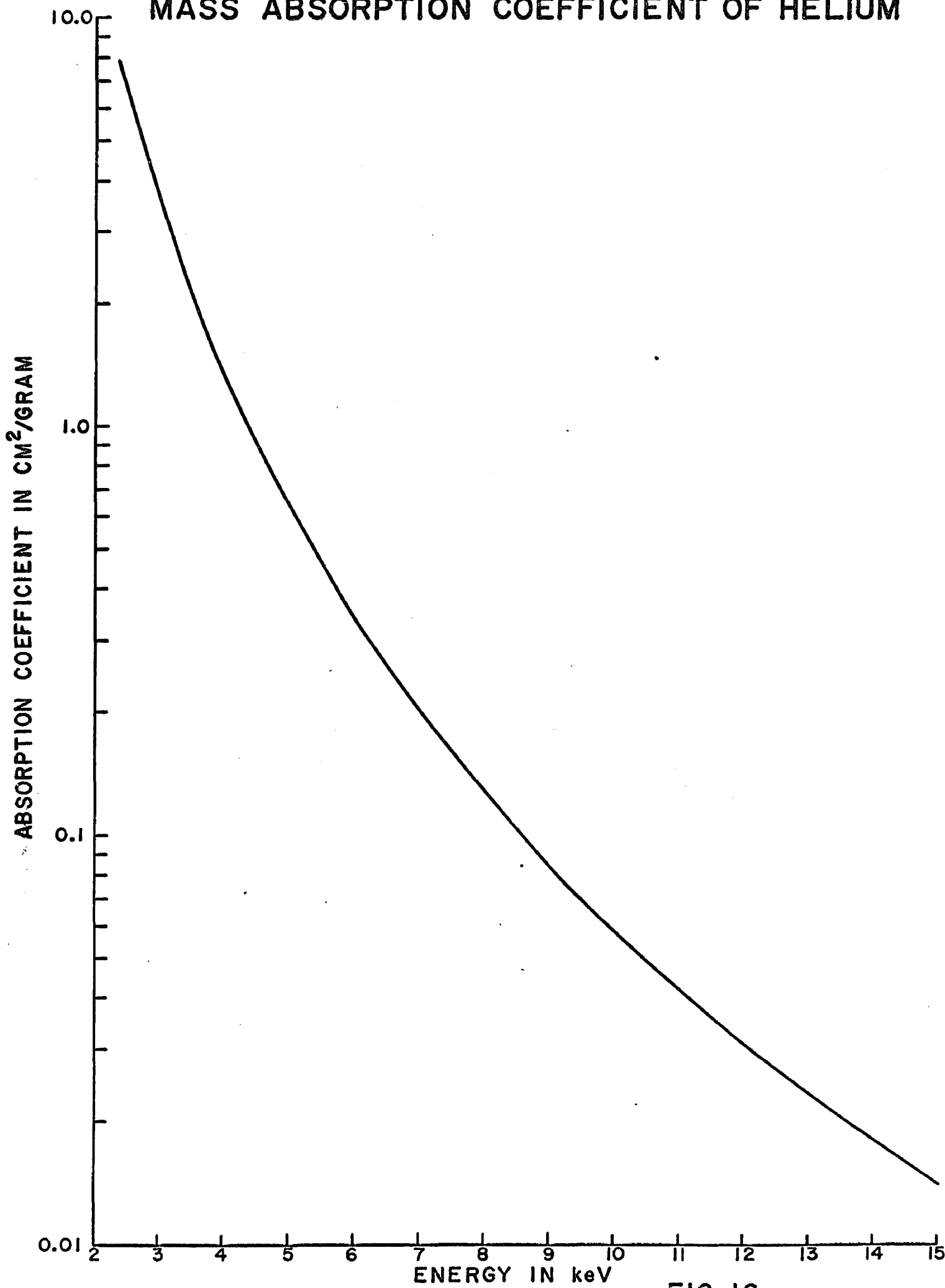


FIG. 16

TRANSMISSION OF 50 MIL BERYLLIUM WINDOW

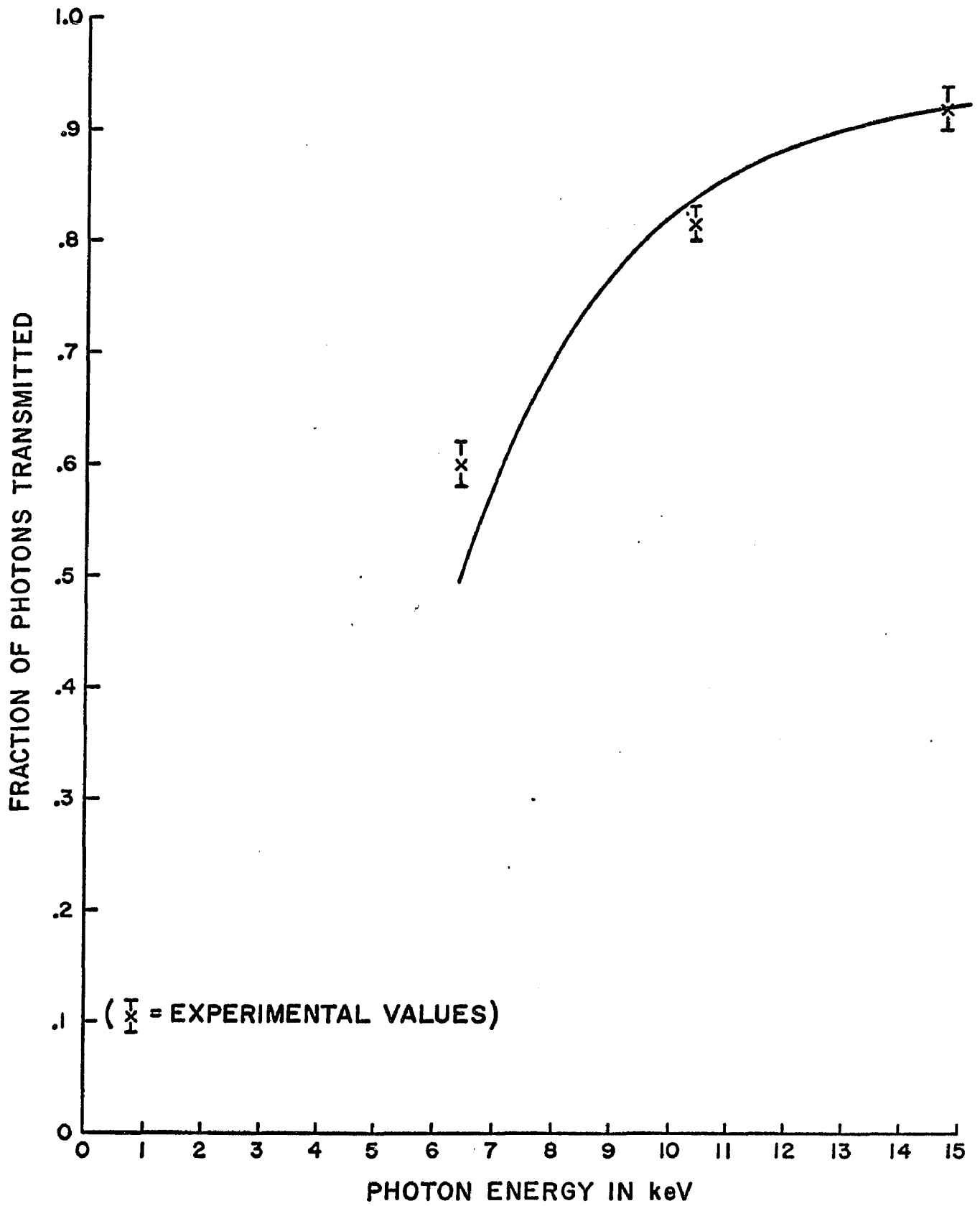


FIG. 17

MASS ABSORPTION COEFFICIENTS OF ALUMINUM AND SILICON

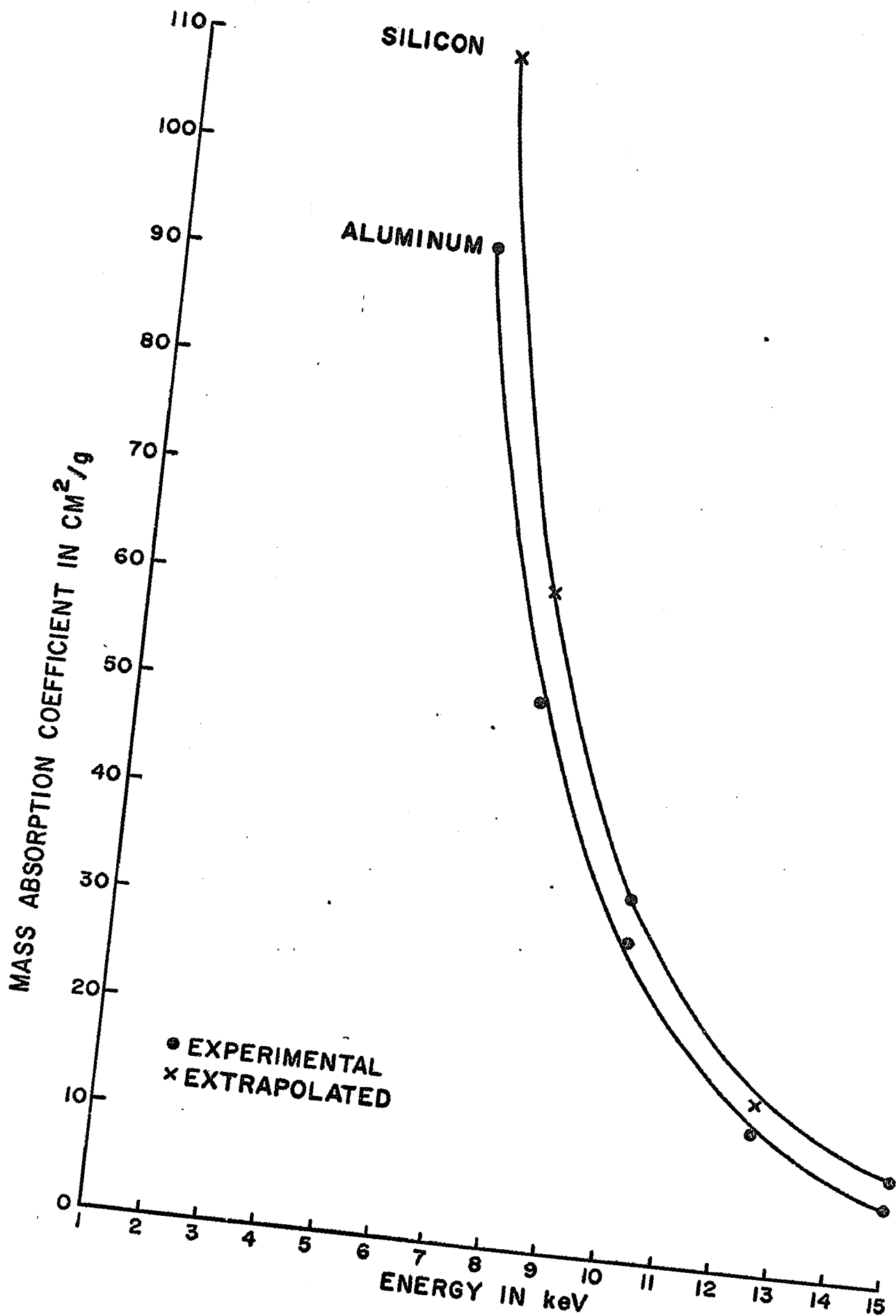


FIG. 18